ABSTRACT

This thesis describes some Raman scattering experiments on solids in the temperature range 1.8 - 300°K. The three main problems studied were : (a) the phase transitions in $PrAlO_3$; (b) the Jahn-teller phase transitions in the series of mixed crystals $Tb_cGd_{1-c}VO_4$; (c) the Two-Magnon excitations in the mixed crystals $Mn_{1-c}Zn_cF_2$.

Chapter 2. reviews the theory of phonons, magnons (both ferromagnetic and anti-ferromagnetic) and electronic excitations in solids. The mechanisms which cause light scattering from these excitations are discussed, together with the selection rules for Raman scattering.

Chapter 3. describes the experimental techniques that were used. The spectra were excited using an Argon-ion laser. A 90° scattering geometry was employed, and the spectra analysed by a double-grating spectrometer. Detection was by means of a photomultiplier tube used in the pulse-counting mode. The sample was mounted in a conventional helium cryostat. Optical birefringence was used to study $Tb_cGd_{1-c}VO_4$; the experimental arrangement is described in this chapter. A superconducting magnet dewar was built in this laboratory for magneto-optical work, and is briefly described in Chapter 3.

In Chapter 4. some experiments on $PrAlO_3$ are discussed. The Raman spectra were measured between 4.2 and 300°K and used

to study the low temperature phase transitions at 146 and 196°K. The Raman data were compared with the predictions of a theoretical model of $PrAlO_3$, based on molecular field theory; this model was found to give a reasonable qualitative description of the observed behaviour. It was concluded that below 99°K $PrAlO_3$ has only a very small deviation from tetragonal symmetry. Optical fluorescence and EPR experiments reinforce this conclusion. In the vicinity of the phase transition at 146°K the anomalous behaviour of two of the low frequency Raman lines was found to be due to coupling between an electronic level of Pr^{3+} and a phonon.

Chapter 5. deals with some Raman and optical birefringence studies on the series of mixed crystals $Tb_cGd_{1-c}VO_4$. The Jahn-Teller phase transition temperatures were measured using the optical birefringence method and found to be in good agreement with the predictions of Molecular Field theory. In addition, this theory predicted a unique type of phase transition for a certain range of c, and this was observed in the crystals with c = 0.365. On cooling, these crystals underwent a Jahn-Teller phase transition to a lower symmetry at 8.5 ± 0.5°K; further cooling resulted in a second phase transition at 2.3 ± 0.1°K temperature at which the crystals reverted to their original high-temperature symmetry. These crystals therefore had a high and low- temperature phase of the same symmetry, with an intermediate phase of lower symmetry. Raman scattering was used to measure the E_g phonon splittings below the transition temperature in the mixed crystals as a

function of temperature. Comparison of experiment with predictions of a Molecular Field theory showed that this theory gave an excellent description of the behaviour of the system. This indicated that the electron-phonon interaction in the mixed crystals was of long range.

Chapter 6. describes the results of some Two-Magnon Raman scattering experiments on $Mn_{1-c}Zn_cF_2$ alloys. The peak-frequencies and linewidths of the Two-Magnon lines at helium temperature were measured over the whole concentration range. These were compared with the predictions of two different theories. The first theory involved calculation of the first three moments of the Magnon lineshape, while the second was a cluster-model theory based on the Ising model. Both theories gave reasonable agreement with the experimental results. The phonon frequencies were also measured at low temperature as a function of c. The E_g phonon exhibited two-mode behaviour for $c < 0.25$, and one-mode behaviour for the rest of the concentration range. This anomaly was attributed to a local mode effect.

Appendix 1. gives a brief description of some attempts to subtract the background Rayleigh scattering from Magnon spectra in order to measure the true lineshape. The experiments failed, but had they been successful, would have enabled a direct comparison between experimentally and theoretically determined moments to be made.

Finally, Appendix 2. describes some phonon and electronic Raman scattering experiments on HoF_3 and TbF_3. The

frequencies of all but two of the Raman active phonons were measured in both materials. At low temperatures electronic transitions between the levels of the ground-state multiplets of the Ho^{3+} and Tb^{3+} were observed. A level scheme for some of the electronic levels within the $^5I_8$ multiplet of Ho^{3+} was derived from these results, but the results for Tb^{3+} have so far proved difficult to interpret.

SOME LIGHT SCATTERING EXPERIMENTS

IN SOLIDS.

by

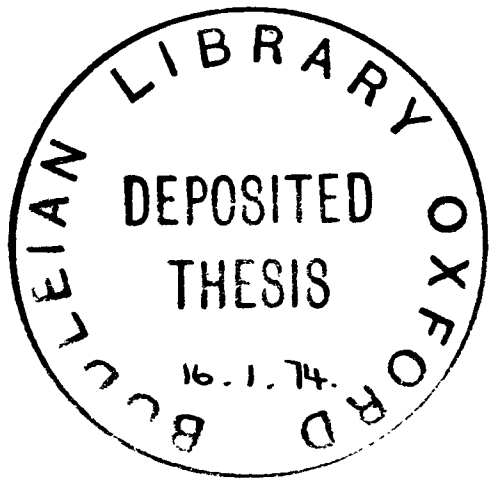
A. M. PERRY

St. John's College

Oxford.

A thesis submitted for the degree of Doctor of Philosophy in the University of Oxford.

November 1973.



ACKNOWLEDGMENTS

I should like to offer my particular thanks to the following people: Professor B. Bleaney, F.R.S., for making the facilities of the Clarendon Laboratory available to me; Dr. W. Hayes, my Supervisor, for cheerful guidance and encouragement; Dr. R.T.Harley and Dr. S.R.P.Smith for many helpful ideas and discussions; Dr. S.H.Smith, Mrs. B.M.Wanklyn and Mr. J. Storey for growing the crystals used in these experiments; Mr. F. Wondre and Mr. G. Read for help in analysing and preparing samples; Mr. H.S. Lock and Mr. E.J.Jenkinson and their workshop staff who have helped build and maintain the apparatus; my mother for patiently deciphering my handwriting and typing this thesis, and finally the Science Research Council and Oxford University for financial support.

CONTENTS

		Page
Chapter 1.	INTRODUCTION	1. 1
Chapter 2.	THEORY	
	2. 1 Phonons	2. 1
	2. 2 Dispersion Curves	2. 4
	2. 3 Anharmonicity	2. 5
	2. 4 Phonons in mixed crystals	2. 6
	2. 5 Semi-classical Theory of the Raman Effect	2.10
	2. 6 Quantum Mechanical Theory	2.13
	2. 7 Selection Rules in Raman Scattering	2.15
	2. 8 Piezo-electric Crystals	2.17
	2. 9 Second-order Raman Effect	2.18
	2.10 Selection Rules for Second-order Raman Effect	2.19
	2.11 Temperature Effects	2.21
	2.12 Magnons	2.22
	(a) Ferromagnetic	2.23
	(b) Anti-ferromagnetic	2.25
	2.13 First-order Magnon Raman Scattering	2.28
	2.14 Second-order Magnon Raman Scattering	2.30
	2.15 Magnons in Mixed Crystals	2.32
	2.16 Electronic Raman Effect	2.33

		Page
Chapter 3.	EXPERIMENTAL TECHNIQUES	
	3. 1 Introduction	3. 1
	3. 2 Laser	3. 1
	3. 3 Spectrometer	3. 2
	3. 4 Detection System	3. 4
	3. 5 Variable-temperature Cryostat	3. 7
	3. 6 Superconducting Magnet Dewar	3. 9
	3. 7 Optical Birefringence Experiments	3.11
Chapter 4.	EXPERIMENTS ON PRASEODYMIUM ALUMINATE	
	4. 1 Introduction	4. 1
	4. 2 Raman Spectra	4. 3
	4. 3 Optical Fluorescence	4.16
	4. 4 EPR Experiments	4.19
	4. 5 Theory	4.20
	4. 6 Conclusions	4.24
Chapter 5.	EXPERIMENTS WITH TERBIUM GADOLINIUM VANADATE	
	5. 1 Introduction	5. 1
	5. 2 Theory	5. 6
	5. 3 Experimental	5.12
	5. 4 Raman Spectra	5.13
	5. 5 Birefringence Experiments	5.16
	5. 6 Comparison of Theory and Experiment	5.18

			Page
Chapter 6.	EXPERIMENTS WITH MANGANESE ZINC FLUORIDE		
	6. 1	Introduction	6. 1
	6. 2	Experimental	6. 3
	6. 3	Raman Spectra	6. 4
	6. 4	Theory of Raman Scattering from $(Mn,Zn)F_2$	6. 7
	6. 5	Moment Calculations	6.11
	6. 6	Cluster Model	6.13
	6. 7	Comparison of Experiment and Theory	6.15
	6. 8	Phonons	6.17
Appendix 1.	MOMENTS		A1. 1
Appendix 2.	ELECTRONIC RAMAN SCATTERING IN HoF_3 and TbF_3		A2. 1
References.			

CHAPTER ONE

INTRODUCTION

The change in frequency of monochromatic light scattered by a material was first observed by C.V. Raman in 1928, and the effect now bears his name. Following this discovery a large number of experiments on Raman scattering were performed, first on gases and liquids, and later on solids. These yielded much information about molecular structure, but experiments were hampered by the low intensity of the scattered light, and work in this field diminished. It was not until the early 1960's, with the advent of the laser, that Raman scattering was again studied in earnest. Many new developments have taken place over the past ten years, and today Raman scattering has become an important method of investigating solids. Most types of elementary excitations in solids scatter light, and this technique is a convenient method of measuring their energies and symmetry properties. Raman scattering from phonons, magnons and electronic excitations is described in this thesis.

Chapter 4. describes some experiments on the low temperature phase transitions of $PrAlO_3$. This material is unique among the Rare-Earth Orthoaluminates in having several phase transitions at low temperatures. Previous work by Cohen et al (1969) and Riseberg et al (1969) showed two phase transitions at 151°K and 206°K. They found that at 80°K the crystal appeared to have only a small distortion from tetragonal symmetry. Our phonon and electronic Raman spectra obtained from 5 - 300°K give evidence that there is

a further gradual transition to a tetragonal phase as the temperature is lowered below 150°K. The experimental results are compared with a molecular field model developed by Smith (Harley et al 1973(a)), which predicts this transition to a tetragonal structure at low temperature. The results of EPR and fluorescence experiments on $PrAlO_3$ are also consistent with a tetragonal phase at low temperatures.

While for $PrAlO_3$ a theory was developed when the experimental results were well established, the opposite was true for $(Tb,Gd)VO_4$. In this case theory predicted a certain phenomenon which was sought for experimentally to confirm this theory. Work on pure $TbVO_4$ (Elliott et al 1972) showed that if the electron/lattice coupling for Tb lay in a certain range, this would lead to two Jahn-Teller phase transitions. At the lower transition the structure should revert to a higher symmetry. It was later suggested that dilution of $TbVO_4$ by Gd might bring the coupling within this critical region. A series of mixed crystals was grown, and this effect was indeed observed. The E_g phonon modes and the electronic levels were measured as a function of temperature, and compared to the Molecular Field Theory. Optical birefringence was used to obtain the transition temperatures, and these results are given in Chapter 5.

Chapter 6. describes the results of two-magnon Raman scattering on $(Mn,Zn)F_2$ alloys at low temperature. This work was prompted by the fact that there was little experimental evidence about spin excitations in materials diluted with a

nonmagnetic constituent. The spectra are compared with two different theories by Buyers, Elliott and Saville (Buchanan et al 1972).

Following from this work it would have been interesting to measure experimentally the moments of a lineshape. The first few moments can often be calculated theoretically in cases where the actual lineshape cannot, and so moments provide a way of comparing theory and experiment directly. To measure the moments of a lineshape it was necessary to subtract the background due to Rayleigh scattering and scattering due to imperfections, etc., especially for lines at low frequencies. Appendix 1. describes several experiments designed to achieve this. Appendix 2. gives the results of some electronic Raman scattering on HoF_3 and TbF_3.

Chapter 2. of this thesis is a review of the theory of phonons, magnons and electronic excitations, together with the theory of Raman scattering. Chapter 3. describes the experimental methods.

CHAPTER TWO

THEORY

2.1 Phonons

The theory of lattice dynamics is now well established, and has been reviewed by Cochran (1963). Some of the results of this theory of relevance to Raman scattering will be discussed in this section. The problem is to obtain a theoretical model of a solid, which is an interacting system of a large number of particles. It is the symmetry of a crystalline solid that makes the theory tractable.

The theory is developed on the basis of several assumptions. In the absence of a detailed knowledge of the interaction in a solid, the adiabatic approximation is used. This assumes that the electrons instantaneously take up a configuration determined by the nuclear displacement, and produce an effective internuclear potential, enabling the forces to be treated as though they acted between nuclei. The potential energy, ϕ, of a crystal may then be expanded as a Taylor series in terms of the small nuclear displacement, (Cochran 1963).

$$\phi = \phi_1 + \phi_2 + \phi_3 + \cdots \qquad (2.1)$$

where
$$\phi_1 = \sum_{sl_j} u^j_{sl} \left[\frac{\partial V}{\partial u^j_{sl}}\right]_0 \qquad (2.2)$$

and
$$\phi_2 = \sum_{sl_j} \sum_{s'l'j'} u^j_{sl}\, u^{j'}_{s'l'} \left[\frac{\partial^2 V}{\partial u^j_{sl}\, \partial u^{j'}_{s'l'}}\right]_0 \qquad (2.3)$$

Where U^j_{sl} is the displacement of the s^{th} atom in the unit

cell l in the direction of j. The first term $\emptyset_1$ is zero as the derivatives are evaluated about the equilibrium position. If terms higher than quadratic in the displacement are neglected, then the restoring force is proportional to the displacement (Harmonic approximation). This leads to a set of classical equations of motion, which in theory could be solved to give the nuclear displacement. However, if we consider N unit cells, each containing n atoms there will be 3Nn equations, (Ziman 1969).

In a regular solid with translational invariance, Bloch's theorem requires that the displacements be of the form (Ziman 1969).

$$u_{sl}(t) = \sum_q e^{i\underline{q}.\underline{l}} \cdot u_{s0}(t) \qquad (2.4)$$

This reduces the number of equations of motion from 3Nn to 3n, which can be solved in the usual way by assuming a time dependance of the displacements of the form $e^{i\omega t}$. Thus the periodicity of the lattice leads to 3n wave-like excitations, frequencies $\omega_1(\underline{q}) \ldots \omega_{3n}(\underline{q})$, which are characterized by $\underline{q}$ the wavevector. A set of 3n normal modes can be found from suitable combinations of these solutions, and these are the <u>phonons</u>. The wavevector $\underline{q}$ can take N values in the Brillouin zone, so that the number of distinct modes is still 3Nn, equal to the number of degrees of freedom of all the atoms.

This treatment effectively replaces the atoms by a set of 3Nn simple harmonic oscillators, which within the

Harmonic approximation are independent. The phonons form a set of orthogonal eigenfunctions, and are therefore non-interacting. The oscillators may be quantized with energy $\hbar\omega$, and the normal modes written in terms of annihilation and creation operators (Kittel 1966).

The phonons are Bosons, and hence obey Bose-Einstein statistics. Thus the number of phonons n_0 of frequency ω at temperature T is given by:

$$n_0 = \left[\exp(\hbar\omega/k_B T) - 1\right]^{-1} \qquad (2.5)$$

A static displacement in a phonon mode can lower the symmetry of the lattice. Obviously, if all the nuclear displacements are zero, the lattice still has the full symmetry of the space group. However, if some of the atoms are displaced from their equilibrium positions by the phonons, then not all the symmetry operations of the group will take the displaced lattice into itself. What is needed is a method of finding the transformation properties of the 3n phonon modes for a given wavevector.

This can be done by considering the transformation properties of displacements on each of the atoms in the unit cell under the symmetry operations of the group appropriate to the particular wavevector being considered. For Raman scattering it will be shown that $\underline{q} = 0$ phonons are excited. This is a particularly simple case, as the symmetry group is then the point group of the lattice. The representation obtained will be 3n dimensional, and in general will be

reducible to a sum of irreducible representations (of the point group for $\underline{q} = 0$) (Heine 1960). Three of these irreducible representations will be vector representations, for the three acoustic modes at $\underline{q} = 0$ are just uniform translations of the whole crystal along the three axes. The remaining $3(n-1)$ irreducible representations are the optic modes. The Raman selection rules discussed later make it possible to decide which of these modes will be Raman active.

2.2 Dispersion Curves

The main parameters of phonons, which are of interest, are the symmetry, polarization, dispersion curves and density of states. The first two are important for $\underline{q} = 0$ phonons in first order Raman scattering, and it was shown above how the symmetry of phonons could be calculated. The dispersion curves and density of states determine the second order spectrum, and some of their properties are discussed in this section.

For a given value of $\underline{q}$, there will be $3n$ normal modes having frequencies $\omega_j(\underline{q})$. These are the $3n$ branches of the ω- q curves called the dispersion curves. For a crystal with n non-equivalent ions per unit cell there will be three branches (one mainly longitudinal, two transverse) of it's dispersion curves whose frequencies approach zero as $\underline{q} \rightarrow 0$. These are called the acoustic modes (Kittel 1966). For

small $\underline{q}$, $\omega_q \propto \underline{q}$ for the acoustical modes. The remaining $3(n-1)$ branches each have a finite limiting frequency as $\underline{q} \to 0$, and are known as optic branches.

The dispersion curves are symmetric about the centre (Γ point) of the Brillouin zone i.e. $\omega(\underline{q}) = \omega(-\underline{q})$, as propagation of phonons does not distinguish between "positive" and "negative" directions. Also $\omega(\underline{q} + \underline{G}) = \omega(q)$ where $\underline{G}$ is a reciprocal lattice vector (Ziman 1969).

The density of state $g(\omega)\,d\omega$ is defined as the number of modes having a frequency between ω and $\omega + d\omega$ For a crystal of volume V containing N unit cells of n atoms each this is $g(\omega)\,d\omega$

$$= \frac{NV}{(2\pi)^3} \sum_{1}^{3n} \int_{\omega=\omega_j(\underline{q})} \frac{dS \cdot d\omega}{|\nabla_{\underline{q}}\, \omega_j(\underline{q})|} \qquad (2.6)$$

The form $g(\omega)$ depends on the actual dispersion curve, but will have singularities with $g(\omega)$ a local maxima whenever $\nabla_q\, \omega_j\ (q) = 0$. These points are called <u>critical points</u> and their existence can be deduced purely on symmetry grounds (Van Hove 1953). The density of states weights the scattering cross-section (in second-order Raman scattering) so that peaks are observed from phonons corresponding to these critical points.

2.3 <u>Anharmonicity</u>

The harmonic approximation used so far explains many

of the features of phonons, but fails to explain phenomena such as thermal expansion and the temperature dependance of the elastic constants and phonon frequencies (Ziman 1969). Anharmonicity results from terms higher than quadratic in the expansion of the potential energy as a power series in the nuclear displacements (equ. 2.1).

Anharmonic theory has been treated by Cowley (1963). The consequences of anharmonicity are that phonons no longer form a set of orthogonal eigenfunctions and so coupling between phonons results. The main effect of this on Raman scattering is a variation in width and frequency of phonon modes as the temperature is changed (Loudon 1964).

2.4. Phonons in Mixed Crystals

So far it has been assumed that the crystal lattice is perfectly regular, free from intrinsic lattice defects and impurities, (e.g. vacancies and interstitials). However, as many of the experiments in this thesis were performed on mixed crystals, some of the effects of impurities will be discussed in this section. Impurities have the effect of destroying the translational invariance of the lattice. This may be sufficient to allow lattice modes to interact with light in cases where they would not otherwise do so. Several cases of impurity induced Raman spectra have been observed (e.g. Harley et al 1971).

Defect atoms can also introduce into the lattice

spectrum modes which are not characteristic of the host lattice itself, but rather of the environment of the impurity. These modes are called Resonance modes, Gap Modes and Local Modes. Resonance modes occur when the impurity has a frequency within the lattice spectrum of the host. A Gap Mode is one whose frequency lies in the gap between the acoustic and optic modes. Localized modes have a high frequency well above the maximum frequency of the host lattice. As the name implies, these modes are localised, having an amplitude of vibration which is large at the defect and decreases rapidly with increasing distance from the impurity.

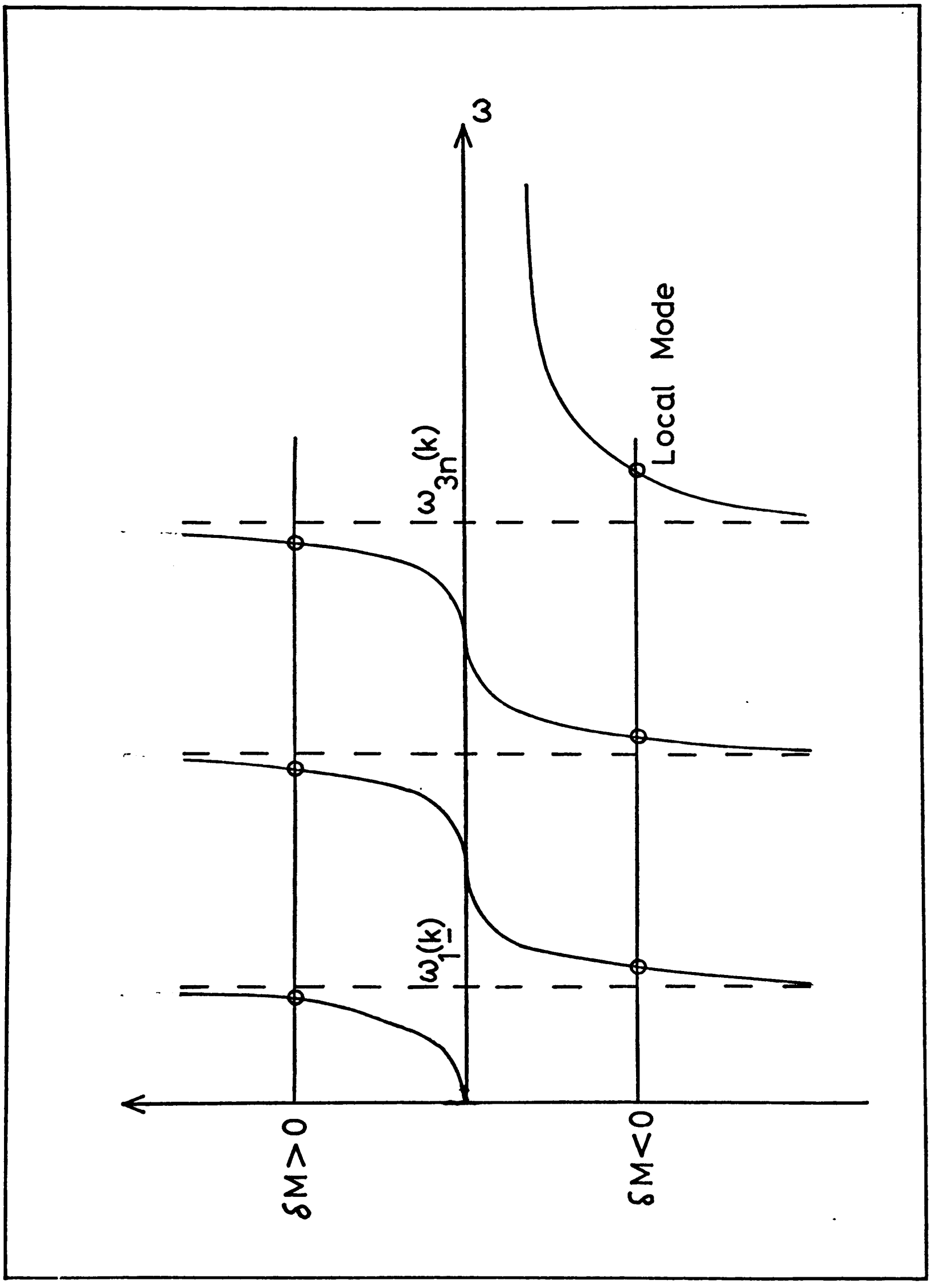
The simplest case of a local mode arises from an isolated mass defect, where it is assumed that the force constants are unchanged. This case is discussed by Dawber and Elliott (1963). The treatment given here (Harrison 1970) assumes that the symmetry of the host crystal is undisturbed by the impurity except in its immediate vicinity. A Green's function method incorporating the defect is then used to determine the normal modes of the crystal. This gives the normal modes , ω , as solutions of

$$\frac{1}{3N} \sum_{\underline{k}} \frac{\omega^2}{\omega(\underline{k})^2 - \omega^2} = \frac{M}{\delta M} \qquad (2.7)$$

where there are N atoms of mass M. A mass defect, $(M + \delta M)$ lies at one lattice site and $\omega(\underline{k})$ are the normal modes of the host lattice. This equation is solved graphically by plotting each side of the equation as a function of ω , the points of the intersection giving the roots. (see Fig. 2.1).

Fig. 2.1.

Graphical solution of Equation 2.7showing production of Local Mode for light mass defect.



It is seen that for $\delta M > 0$ (heavy mass defect) no new modes are formed, and the frequencies depart only slightly from $\omega(\underline{k})$. For $\delta M < 0$ an extra solution occurs at $\omega > \omega(\underline{k})_{Max}$, the local modes. Local modes also occur if the impurity has a similar mass to the atom it replaces but has a larger force constant. These local modes provide information on the interatomic forces near the defect, and have been observed experimentally in several materials, e.g. the local mode due to H^- in CaF_2 (Elliott et al 1966).

If the impurity content is increased sufficiently, interactions between impurity atoms become important. These crystals are usually termed "mixed" rather than "impure". Mixed crystals are those which are formed by two components with a range of concentration ratios. The two systems studied in this thesis $(Mn,Zn)F_2$ and $(Tb,Gd)VO_4$ could be grown with concentrations varying over the whole concentration range. The behaviour of the long wavelength optical phonons in mixed crystals have been reviewed by Chang and Mitra (1971).

The collected results show that there are generally two classes of mixed crystal. One class exhibits the so-called "one-mode behaviour" in which the $\underline{q} \simeq 0$ phonon frequencies of each of the modes vary continuously with concentration from the frequencies of one end member to that of the other, and appear with approximately constant strength. The other class shows "two-mode behaviour" in which for intermediate concentrations two sets of phonon frequencies occur at frequencies close to those of the end members, the strength of

each mode being approximately proportional to the mole fraction of each component. A few compounds have been found which fit neither class, exhibiting one-mode behaviour over part of the concentration region and two-mode behaviour over the rest.

Several theoretical models of mixed crystals are discussed by Chang and Mitra, there being at present no rigorous theory to account for the lattice vibrations of mixed crystals over the whole concentration range. These models and empirical facts are used as a basis to obtain criteria for predicting the behaviour of mixed crystals. For a mixed crystal system $AB_{1-x}C_x$ the criteria are:-

(1) If the substitution is made on the heavier elements ($M_B, M_C > M_A$) the system is one-mode type. The converse is not always true.

(2) If the reststrahlen bands of the pure compounds overlap the mixed system is one-mode type. Again the converse is not necessarily true.

(3) If the mixed crystal system exhibits two-mode behaviour throughout the concentration range ($0 < x < 1$) the lighter crystal must have a frequency gap between its acoustic and optic bands to allow the gap mode to appear.

(4) If the mixed crystal system is two-mode the masses must be such as to allow the existence of a local mode.

These "rules" are obeyed by most crystal systems with a few exceptions, and give a good indication of the likely

type of behaviour

2.5 Semi-Classical theory of the Raman Effect

Raman scattering in a crystal is the inelastic scattering of light with the creation or destruction of an elementary excitation in the solid. This section will deal exclusively with scattering by phonons. However, other kinds of excitation can scatter light inelastically, and Raman scattering by Magnons and the Electronic Raman effect are discussed in later sections.

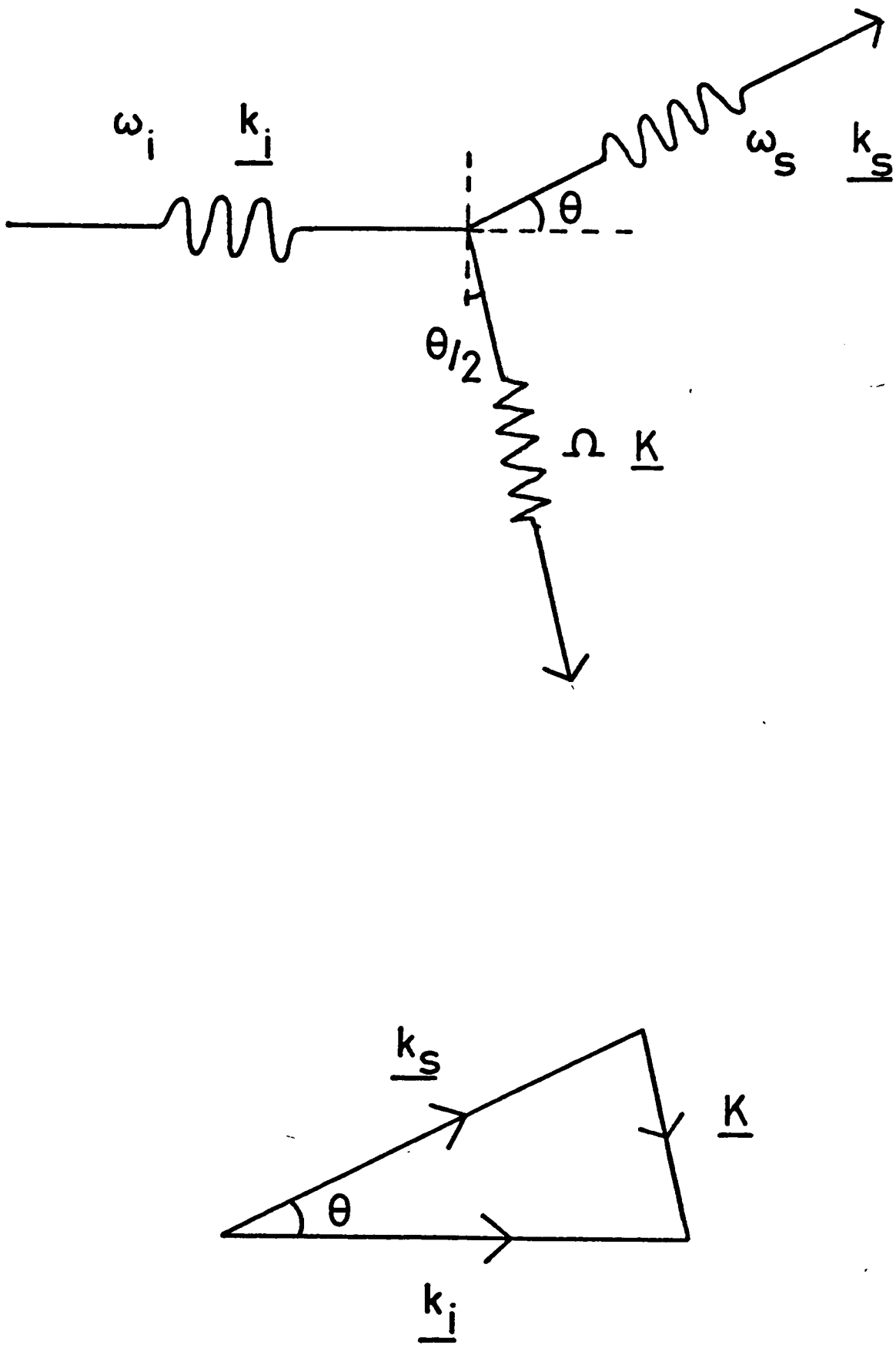
Phonons can be divided into two classes, optic and acoustic. Inelastic scattering from acoustic phonons occurs in the frequency range $0 \rightarrow 1_{cm}^{-1}$ approximately, and is known as Brillouin scattering. Light scattered from optic modes generally has a frequency shift of about $10 \rightarrow 1000cm^{-1}$; this is called Raman scattering. The theory of the Raman effect has been discussed in a review article by Loudon (1964).

Consider a photon, frequency ω_i, wavevector $\underline{k}_i$ being scattered through an angle θ by the production of one phonon of frequency Ω, wavevector $\underline{k}$ giving a scattered photon (ω_s, $\underline{k}_s$) as shown in Fig. 2.2. Conservation of energy and wavevector give:-

$$\left.\begin{aligned} \omega_i &= \omega_s + \Omega \\ \underline{k}_i &= \underline{k}_s + \underline{k} \end{aligned}\right\} \qquad (2.8)$$

Fig.2.2.

One-phonon Raman scattering. The lower picture shows the conservation of wavevector.



If the incident light is in the visible region, then the wavelength $\lambda_i \backsimeq 10^{-5}$cm., and wavevector $\underline{k}_i = \frac{2\pi}{\lambda_i} \backsimeq 10^5 cm^{-1}$. For 90^o scattering, the usual experimental arrangement, the phonon and photon wavevectors are of the same order of magnitude, thus $\underline{k} \backsimeq 10^5 cm^{-1}$ also. At the Brillouin Zone boundary, $\underline{k}_{zb} \backsimeq 10^8 cm^{-1}$, so that $\underline{k} \ll \underline{k}_{zb}$. Thus Raman scattering effectively excites zone centre ($\underline{k} \backsimeq 0$) phonons only.

Classically the electric field, $\underline{E}$, of the incident photon,

$$\underline{E} = \underline{E}_o \cos \omega_i t \qquad (2.9)$$

may be thought of as producing a polarization, $\underline{P}$, in the material. These are related by :-

$$\underline{P} = \underline{\underline{\alpha}} \cdot \underline{E} \qquad (2.10)$$

where $\underline{\underline{\alpha}}$ is the polarizability tensor. Higher order terms in the electric field are of importance only for very high light intensities, and may be neglected here. The polarizability is modulated by the phonon frequency, Ω, and the oscillating polarization re-radiates light. Taking components of equation 2.10

$$P_i = \alpha_{ij} E_j \qquad (2.11)$$

For a single phonon, frequency Ω, its normal co-ordinate $Q_1(t)$ can be written as

$$Q_1(t) = Q_1 \cos \Omega t \qquad (2.12)$$

Because of the electron/lattice interaction, the electronic

eigenvalues depend on the relative displacement of the atoms and α_{ij} can be expanded as a power series in the phonon co-ordinates, (Loudon 1964).

$$\alpha_{ij} = (\alpha_{ij})_0 + \left(\frac{\partial \alpha_{ij}}{\partial Q_1}\right)_0 Q_1 \cos \Omega t + \ldots \text{ Higher terms} \qquad (2.13)$$

where the derivative is evaluated at $Q_1 = 0$, writing this in a more concise notation

$$\alpha_{ij} = \alpha_{ij}^{0} + \alpha_{ij}^{1} \cos \Omega t \qquad (2.14)$$

Combining equations 2.9, 2.11 and 2.14

$$\begin{aligned} P_i &= \alpha_{ij}^{0} E_j^{0} \cos \omega_i t + \alpha_{ij}^{1} E_j^{0} \cos \Omega t \cdot \cos \omega_i t \\ &= \alpha_{ij}^{0} E_j^{0} \cos \omega_i t + \tfrac{1}{2} \alpha_{ij}^{1} E_j^{0} \left[\cos (\omega_i - \Omega) t + \cos (\omega_i + \Omega) t\right] \end{aligned} \qquad (2.15)$$

Thus the scattered light contains three components at frequencies ω_i, $(\omega_i + \Omega)$ and $(\omega_i - \Omega)$. The elastically scattered light, ω_i, is called Rayleigh scattering. The component at lower frequency $(\omega_i - \Omega)$ is the Stokes component, due to creation of one phonon, while that at higher frequency $(\omega_i + \Omega)$ (Anti-Stokes) is due to destruction of phonon.

Generalizing to n, normal modes, frequencies $\Omega_1 \ldots \Omega_n$., equation (2.14) becomes

$$\alpha_{ij} = \alpha_{ij}^{0} + \sum_{k=1}^{n} \alpha_{ijk}^{1} \cos \Omega_k t \qquad (2.16)$$

giving a Rayleigh line, ω_i , plus n Stokes lines at frequencies $(\omega_i - \Omega_1)$.... $(\omega_i - \Omega_\eta)$ and n Anti-Stokes lines (Born and Huang 1954).

2.6 Quantum Mechanical Theory

Although the above semi-classical theory gives a qualitative description of the Raman effect, a quantum mechanical description of the states and interactions is needed to predict the selection rules governing the transitions.

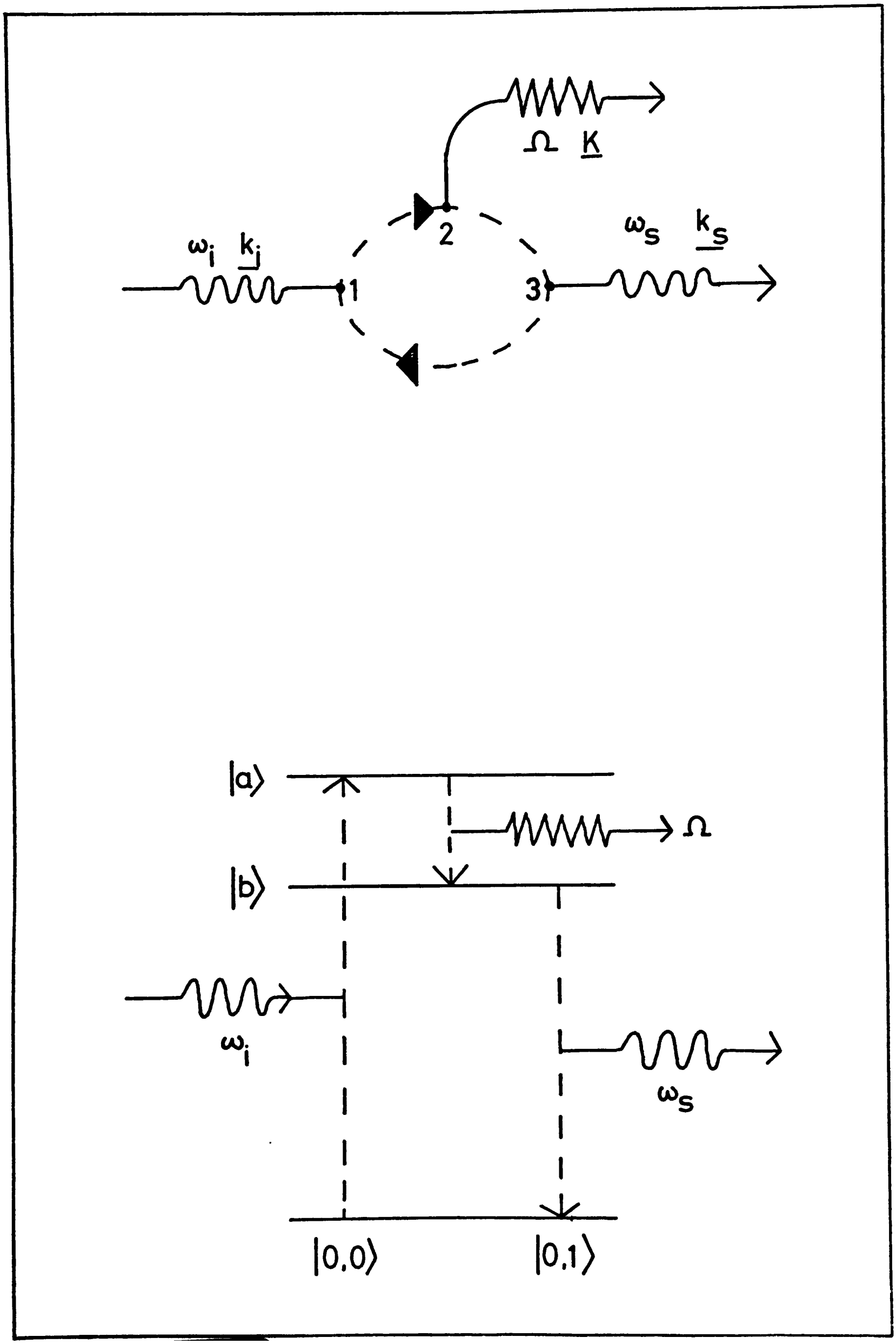
Raman scattering consists of three transitions, (1) absorption of a photon, frequency, ω_i ., (2) emission of a phonon, Ω (confining attention to the Stokes component) and (3) emission of a photon ω_s . This sequence of events is shown in Fig. 2.3 (Loudon 1964).

The incident photon induces a virtual transition from the electronic and vibrational ground state $|0,0\rangle$ (in second quantisation notation,) to a state $|a\rangle$ through the electron/radiation interaction H_{ER}. This decays with phonon emission to another state $|b\rangle$, through the electron/lattice interaction H_{EL}. Finally, the system reverts to its ground electronic state and excited vibrational state $|0,1\rangle$ with the emission of a photon. The final state of the system is in an excited vibrational state, due to the creation of a phonon.

These events can be treated by third-order perturbation

Fig. 2.3.

One-phonon Raman scattering.



theory, giving a transition probability governed by a term like

$$\sum_{a,b} \left[\frac{\langle 0,0|\underline{er}_i|a\rangle\langle a|H_{EL}|b\rangle\langle b|\underline{er}_j|0,1\rangle}{(\omega_a-\omega_s)(\omega_b-\omega_i)} \right] \qquad (2.17)$$

Where $\underline{er}_i$ and $\underline{er}_j$ are the dipole operators inducing the transitions, i and j relating to the polarization directions of the electric vector of the incident and scattered radiation respectively.

The wavefunctions $|0,0\rangle$ and $|0,1\rangle$ transform like the normal modes of vibration that they represent. As $|0,0\rangle$ is the vibrational ground state, from group theory this transforms as Γ_1. the identical representation. H_{EL} is a Hamiltonian of the system, and must therefore have the full symmetry of the crystal, so it too must transform like Γ_1. Then the term $|a\rangle\langle a|H_{EL}|b\rangle\langle b|$ also transforms as Γ_1, so from the integral theorem of group theory (Tinkham 1964) the term (2.17) will only be non-zero if $|0,1\rangle$ transforms like $(\underline{r}_i\underline{r}_j)$.

The terms $(\underline{r}_i\underline{r}_j)$ transform like the irreducible representations having basis functions like (xx,yy,zz,xy,xz,yz). Thus only modes with these basis functions will be Raman active. In direct-product groups these will be even ("g") modes. This is in contrast to infra-red absorption, where all the infra-red active modes are odd ("u") so that infra-red absorption and Raman scattering are complementary procedures in these crystals.

The scattering efficiency, S, is the ratio of the number of scattered photons of frequency ω_s produced per unit time per unit cross-sectional area of the crystal in a solid angle $d\Omega$ about the direction of observation to the number of incident photons ω_i crossing unit area in unit time. This is calculated by summing over the matrix elements 2.17 (Loudon 1964). For the usual experimental arrangement of right-angle scattering ($\underline{k}_i \perp \underline{k}_s$), which minimizes the Rayleigh scattered component of the spectrum, this gives,

$$S = A\left[\sum_{\substack{\rho,\sigma \\ =x,y,z}} e_i^{\sigma} R_{\sigma\rho} e_s^{\rho}\right]^2 \qquad (2.18)$$

where σ and ρ denote the axes along which the electric vectors of the incident and scattered light are polarized. $R_{\sigma\rho}$ is the Raman tensor, and has the same symmetry properties as α_{ij} in the semi-classical theory. The form of this tensor is such that

$$R_{\sigma,\rho}(-\omega_i, \omega_s, \Omega) = R_{\rho,\sigma}(-\omega_i + \Omega, \omega_s + \Omega, -\Omega) \qquad (2.19)$$

Therefore, provided $\Omega \ll \omega_i, \omega_s$ the Raman tensor is symmetric.

2.7 Symmetry and Selection Rules in Raman Scattering

It has been shown in section 2.1 that the phonon branches are characterized by the irreducible representations of the crystal space group, and correspond to different symmetries of vibration of the atoms in the unit cell. Raman scattering involves phonons which have effectively $\underline{k} = 0$ and

this leads to the simplification that the crystal point group can be used. This applies only to crystals which have a centre of inversion. Crystals lacking a central inversion (piezo-electric) are discussed briefly below. All the materials discussed in this thesis retained a centre of inversion in each phase.

For a given structure the irreducible representations of all the phonons can be found. The problem is to decide which of these will be Raman active. As the transition probability depends upon the Raman tensor, (or the polarizability tensor which has the same symmetry) it follows from the integral theorem of group theory that a phonon mode will be first order Raman active if, and only if, its irreducible representation is the same as one of the irreducible representations which occur in the reduction of the polarizability tensor. The irreducible representations of the polarizability tensor have been calculated for the 32 crystal point groups by several authors, and all their results collected together in the review by Loudon. This also lists the non-vanishing components of the Raman tensor, so that the polarization properties of these phonons may be determined, using equation (2.18).

Thus from a knowledge of the structure of a crystal, group theory enables the number of phonons and their irreducible representations to be calculated. The selection rules then determine which of these modes will be Raman active, and give their polarization properties. Reversing this

process, it is possible to infer something of the crystal structure from observation of its Raman spectrum, and it is this technique which has been most often used in this work.

A consequence of the selection rules is the so-called "Centre of Inversion" rule - if all the atoms in the unit cell lie at centres of inversion, there will be no first order Raman spectrum. This follows from the impossibility of there being any even-symmetry phonon modes, as any displacement of an atom from its equilibrium position will have odd-symmetry under inversion about that point.

2.8 Piezo-Electric Crystals

Piezo-electric crystals have no centre of inversion, and so phonon modes may be both infra-red and Raman active. For these phonons there will be interaction of the light with the mechanical vibration and the excitation around the interaction region will be partially phonon and partially light. This mixed excitation in the interaction region is called a polariton.

Polaritons exist only for very small values of $\underline{k}$ so that in order to scatter light from them the Raman spectra must be observed in the forward direction. Since the scattering process conserves momentum, a polariton with minimum $\underline{k}$ will be produced in the forward direction. By increasing the scattering angle from the forward direction polaritons of increasingly higher $\underline{k}$ can be observed until

the excitation becomes pure phonon for angles greater than about 10^{o}. Raman scattering from polaritons has been observed in several piezo-electric materials e.g. ZnO (Porto, Tell and Damen 1966). Quartz (Scott, Cheesman and Porto 1967) and CdS (Gross et al 1971).

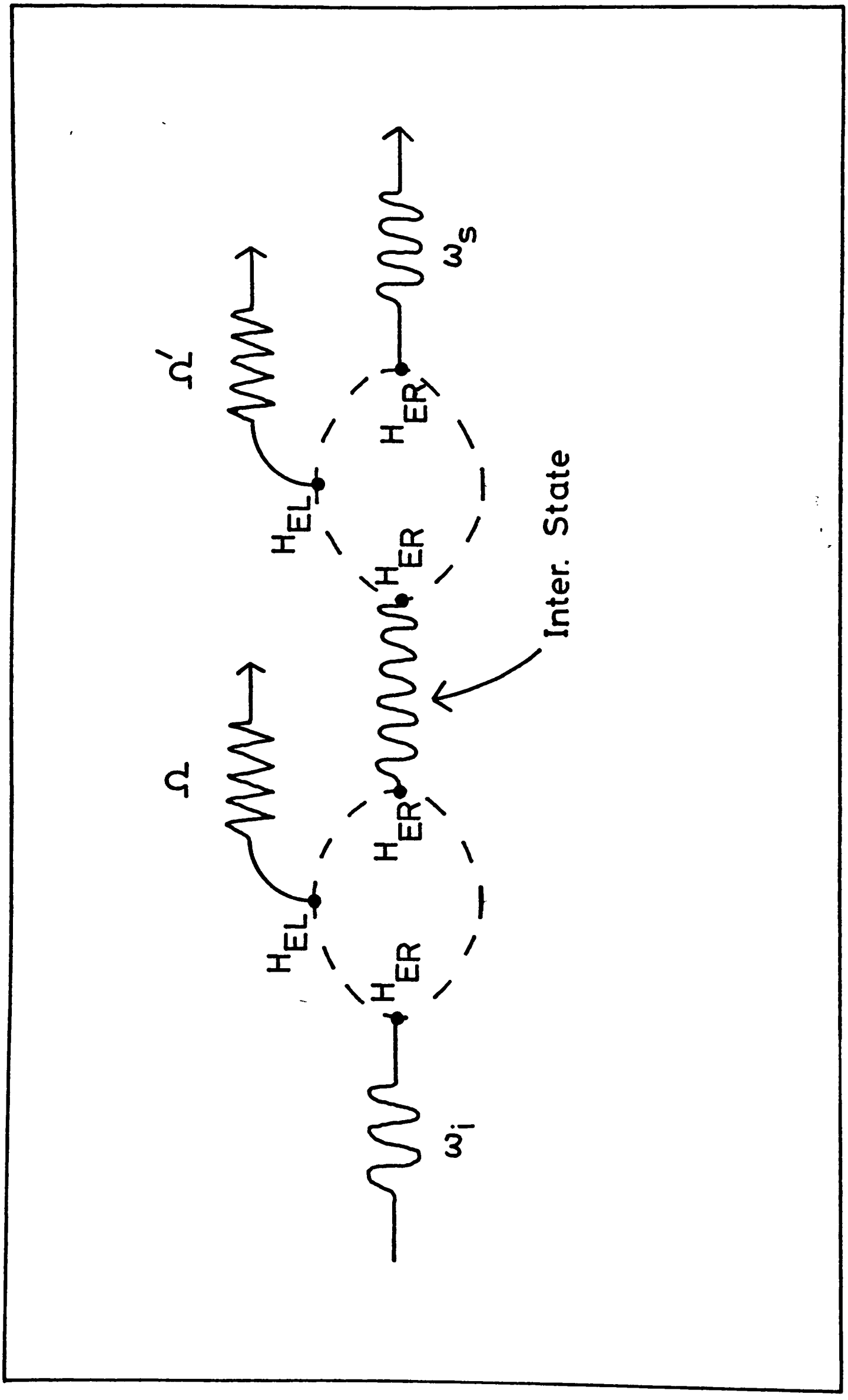
2.9 Second Order Raman Effect

Second order Raman scattering is a process in which two phonons participate in the scattering process. These may either both be destroyed, giving a Stokes component, both created (Anti-Stokes) or one created and one destroyed, (Stokes or Anti-Stokes, depending on their relative frequency). In addition, there are two types of second order Raman scattering, giving either a line or continuum spectrum. These processes arise from higher order terms in equation (2.13).

Line spectra occur when light suffers two successive first-order scattering events, as shown in Fig. 2.4 (Loudon 1964). The two phonons must individually satisfy the first-order Raman selection rules, and no information about the phonon frequencies in addition to that given by the first-order spectra is obtained. The scattering efficiency for this process depends on the crystal volume, as both scattering events must take place within the crystal. The scattering efficiency is small compared with first order processes, for if a fraction (1/n) of the incident photons are scattered in first order, only about $(1/n)^{2}$ will be scattered by this type of second

Fig. 2.4.

Two-phonon Raman scattering, showing mechanism which produces line spectra.



order event.

The continuum is due to a different type of scattering, where the light interacts with a pair of phonons simultaneously, Fig. 2.5 (Loudon 1964). Now there is no restriction on the phonon wavevectors, except that their sum should equal the change in wavevector of the scattered photon. Since the photon wavevector is small compared with the Brillouin zone boundary, this requires the wavevector of two phonons to be approximately equal and opposite. The shape of the continuum is determined by the density of states of the phonon dispersion curve for the pair of phonons. As the continuum derives from a single scattering event, its scattering efficiency is independant of crystal size, and this gives an experimental method of distinguishing the two types of scattering. Thus information about the density of states can be inferred from the continuum spectrum.

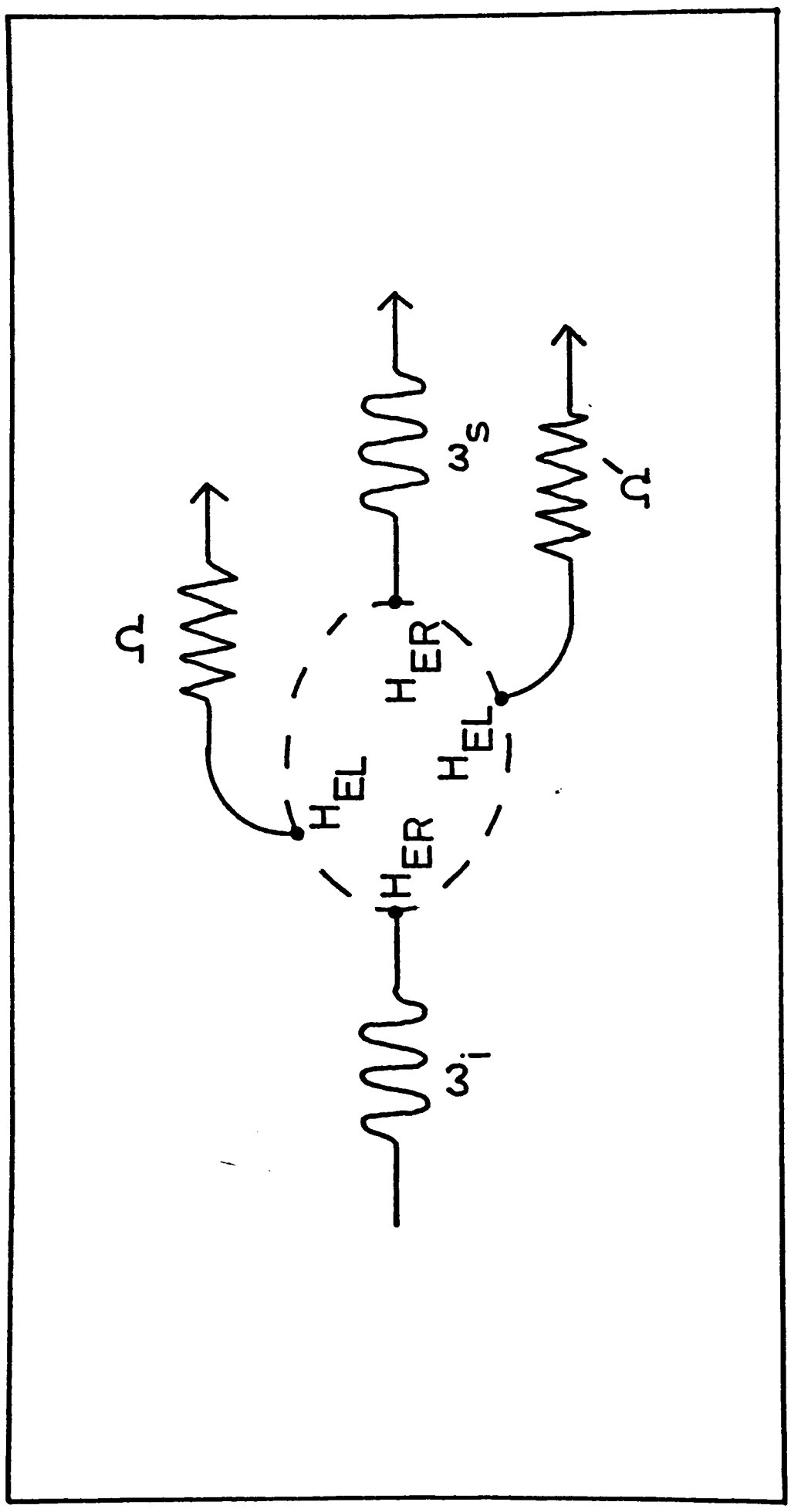
In general the second order spectra are weaker than the first order in a given material. However, there are exceptions to this, e.g. in TiO_2 (Porto et al 1967) and care must be taken in assigning lines as first order solely on a basis of their intensity.

2.10 Selection Rules for Second Order Raman Effect

A theory of the second order Raman effect has been developed using the polarizability derivative approach (Born and Bradburn 1947). However, for comparison with

Fig. 2.5.

Two-phonon Raman scattering. Mechanism responsible for continuum spectra.



experiment the critical point analysis is usually used (Loudon and Johnson 1964).

This critical point analysis associates sharp features of the spectrum with pairs of phonons from the critical points of the dispersion curve. In practice, the shape of the spectrum depends on the phonon density of states and the dependance of the interaction with wavevector and frequency. However, the interaction will not normally have a frequency dependance with sharp discontinuities so that all the peaks in a second order spectrum usually correspond to the critical points.

As Raman scattering from pairs of phonons at a particular critical point may be forbidden, it is important to have selection rules for pairs of phonons at a given wavevector. These have been deduced from group theory (Bhagavantam and Venkatarayudu 1939).

These selection rules are simplest when both phonons are at the Brillouin zone centre. If the two phonons belong to the same branch then the two phonon state is described as an "overtone", whereas if they belong to different branches it is called a "combination". For combination states the Raman transition is allowed if the Kronecker product of the irreducible representations of the two phonons contain irreducible representations in common with the polarizability tensor. For overtone states the symmeterized Kronecker square of the phonon irreducible representations must be used. These selection rules apply to $\underline{k} = 0$ phonons (Loudon 1964). Selection rules for $\underline{k} \neq 0$ are more complex, and have been

dealt with by Birman (1962).

2.11 Temperature Effects

The general features of a Raman spectrum as the temperature is increased are that the linewidths increase while the peak frequencies decrease. The decrease in frequency is usually greater for lower frequency lines. These effects can be qualitatively understood by allowing for anharmonic forces in the crystal.

When anharmonic forces are included, the delta function scattering efficiency S is replaced by

$$S(\omega_s) = \frac{S}{\pi} \cdot \frac{\Gamma}{(\omega_i - \Omega - \omega_s - \Delta)^2 + \Gamma^2} \qquad (2.20)$$

a Lorentzian line shape about a frequency $(\omega_i - \Omega - \Delta)$ with half-width Γ (Loudon 1964). The total scattering efficiency is still S , as

$$\int S(\omega_s)\, d\omega_s = S \qquad (2.21)$$

Expressions for Γ and Δ have been derived quantum mechanically by Maradudin et al (1962). The theory is complicated, but its predictions agree with experiment in that $\Delta = \Delta_0 + \alpha T$ and $\Gamma = \Gamma_0 + \beta T$ for $K_B T/\hbar \gg$ phonon frequencies.

The Stoke and Anti-Stokes intensities at a given

temperature are proportional to $(n_0 + 1)$ and n_0 respectively where n_0 is given by equation (2.5).

Thus the ratio of intensities of Stokes and Anti-Stokes components are given by

$$\frac{I(\text{Anti-Stokes})}{I(\text{Stokes})} = \frac{n_0}{n_0+1} = \frac{(e^{\hbar\omega/k_BT}-1)^{-1}}{e^{\hbar\omega/k_BT}(e^{\hbar\omega/k_BT}-1)^{-1}} = e^{-\hbar\omega/k_BT} \qquad (2.22)$$

While the one-phonon Stokes intensity decreases with temperature like $(n_0 + 1)$ the two phonon spectra, at the same frequency, decreases as $(n_0 + 1)^2$. Thus the second order spectrum decreases more rapidly as the temperature is reduced. This gives another method of distinguishing the two types of spectra.

2.12 Magnons

Magnons are the quantised excitations of a spin system from its ground state. The ground state cannot always be determined exactly, but to a good approximation can be taken as the Neel state, where all the spins are fully aligned, either parallel in a ferromagnet or anti-parallel in an anti-ferromagnet. These excitations are similar in some ways to phonons. They can be derived from a simple Hamiltonian whose terms are well understood, but the theory is more complicated as we cannot usually make the harmonic approximation with magnons, except in a ferromagnet at low temperatures. This section will review the theory of

ferromagnetic and anti-ferromagnetic magnons, and then go on to discuss the mechanisms for one and two magnon light scattering.

(a) Ferromagnetic Magnons

Assuming a nearest neighbour exchange coupling J_{ij} and an external magnetic field H applied in the z direction, the ferromagnetic spin Hamiltonian can be written (Fleury and Loudon 1968).

$$\mathcal{H} = -\sum_{ij} J_{ij}\, \underline{S}_i \cdot \underline{S}_j - g\beta H_0 \sum_i S_i^z \qquad (2.23)$$

in the Heisenberg representation. The Ising approximation ignores off-diagonal elements of the spin operators and just considers spin along the field (z axis).

The Ising Hamiltonian is

$$\mathcal{H}_{Ising} = -\sum_{ij} J_{ij} S_i^z S_j^z - g\beta H_0 \sum_i S_i^z \qquad (2.24)$$

The ground state of the Hamiltonian (2.23) is taken to be the state with all spins parallel and have the maximum value S of the spin along the z axis.

The components of $\underline{S}$, i.e. S^x, S^y, and S^z are not independent, as $\underline{S}_i \cdot \underline{S}_i = S(S+1)$. It is therefore convenient to make a linear transformation to operators which are independent (Kittel 1966). viz.,

$$\left.\begin{aligned} S^+ &= S_x + iS_y \\ S^- &= S_x - iS_y \end{aligned}\right\} \qquad (2.25)$$

These obey the commutation rules (Ziman 1969)

$$\left.\begin{aligned} \left[S_i^+, S_j^-\right] &= 2S_i^z \delta_{ij} \\ S_i^z,\ S_j^{\pm} &= \pm S_i^{\pm} \delta_{ij} \end{aligned}\right\} \qquad (2.26)$$

The $S^{\pm}$ are raising and lowering operators, as they increase or decrease S^z by 1.

$$\begin{aligned} S^+ |S^z = m\rangle &= \sqrt{(S-m)(S+m+1)}\ |S^z = m+1\rangle \\ S^- |S^z = m\rangle &= \sqrt{(S+m)(S-m+1)}\ |S^z = m-1\rangle \end{aligned} \qquad (2.27)$$

The $S^+.S^-$ can be written in terms of the Boson annihilation and creation operators a, a^+ by the transformations (Kittel 1966).

$$\left.\begin{aligned} S^+ &= (2S - a^+a)^{\frac{1}{2}}\, a \\ S^- &= a^+ (2S - a^+a)^{\frac{1}{2}} \end{aligned}\right\} \text{ where } \left[a, a^+\right] = 1 \qquad (2.28)$$

From which $\qquad S^z = S - a^+a$

To apply these transformations it is necessary to approximate the square roots, so that $S^+ \simeq \sqrt{2S}\, a$ and $S^- \simeq \sqrt{2S}\, a^+$. This is equivalent to the harmonic approximation in the phonon theory. Writing the Hamiltonian in terms of Boson operators.

$$\begin{aligned} \mathcal{H} = &- \sum_{ij} J_{ij} S^2 - g\beta H_0 \sum_i S \\ &+ \sum_{ij} J_{ij} S \left(a_i a_j^+ + a_i^+ a_j\right) + g\beta H_0 \sum_i a_i^+ a_i - \sum_{ij} a_i^+ a_i a_j^+ a_j \end{aligned} \qquad (2.29)$$

The last term is neglected in the low temperature approximation where few magnon states are populated, as it contains two annihilation operators and is therefore zero unless two magnons are present.

Finally, the Hamiltonian is diagonalized by writing it

in terms of magnon operators b_k and b_k^+, related to a_i, a_i^+ by the Fourier transforms

$$a_i = \frac{1}{\sqrt{N}} \sum_{\underline{k}} e^{i\underline{k}.\underline{r}_i} b_k \; ; \quad a_i^+ = \frac{1}{\sqrt{N}} \sum_{\underline{k}} e^{-i\underline{k}.\underline{r}_i} b_k^+ \; ; \; J(\underline{k}) = \sum_{ij} J_{ij} e^{i\underline{k}.(\underline{r}_i - \underline{r}_j)} \quad (2.30)$$

The Hamiltonian becomes

$$H = E_0 + \sum_{\underline{k}} E_k b_k^+ b_k \quad (2.31)$$

with eigenvalues

$$E_k = \hbar\omega_k = \{[J(0) - J(\underline{k})]S + g\beta H_0\} \quad (2.32)$$

In zero field, and assuming a nearest neighbour isotropic exchange J, J(k) can be expanded as $\underline{k} \to 0$ giving (Kittel 1966)

$$\lim_{\underline{k} \to 0} \hbar\omega_k \propto S J(\underline{k})^2 \quad (2.33)$$

Thus the magnon dispersion curve for a ferromagnet has $\omega \propto k^2$ near the zone centre (cf. phonons).

If the term $(2S - a^+a)^{\frac{1}{2}}$ in equation (2.28) had been expanded further, the next highest terms would have been fourth order, like $a^+a^+a\,a$. These terms give interactions between magnons. However, as the terms contain two annihilation operators, they are only non-zero if two magnons are present. Therefore at low temperatures the approximation that magnons behave like non-interacting Bosons is valid.

(b) Anti-Ferromagnetic Magnons

If J_{ij} changes sign, then the spins align anti-parallel to minimize the energy. This gives two sublattices i and j for simple structures like MnF_2 and the Hamiltonian can be

written as

$$\mathcal{H} = +\sum_{ij} J_{ij}\, \underline{S}_i \cdot \underline{S}_j - g\beta H_A \left[\sum_i S_i^{z} - \sum_j S_j^{z}\right] - g\beta H_0 \left[\sum_i S_i^{z} + \sum_j S_j^{z}\right] \qquad (2.34)$$

H_A is the Anisotropy field, a local field which provides a unique axis of alignment for the spins. H_A is generally small. If $H_A = 0$ the spin sytem is in a state of neutral equilibrium and all the spins could rotate together with no change in energy (Ziman 1969). The total spin $S^z = 0$.

There are now two types of magnon for each value of $\underline{k}$. Creation of a magnon on the "up" spin lattice changes S^z by - 1, whereas creation of a magnon on the "down" lattice changes S^z by + 1. If the sublattices are equivalent (as in MnF_2) then the magnon branches are degenerate.

Four spin-operators are now defined, two for each sublattice. These are transformed to magnon operators in a similar manner to the ferromagnetic case giving (Fleury and Loudon 1968)

$$\left.\begin{aligned} S_i^{+} &= (2S/N)^{\frac{1}{2}} \sum_k (u_k b_{\downarrow k} + \sigma_k b_{\uparrow -k}^{+})\, e^{i\underline{k}\cdot\underline{r}_i} \\ S_i^{-} &= \;\;\text{"}\;\; \sum_k (u_k b_{\downarrow k}^{+} + \sigma_k b_{\uparrow -k})\, e^{-i\underline{k}\cdot\underline{r}_i} \\ S_j^{+} &= \;\;\text{"}\;\; \sum_k (\sigma_k b_{\downarrow -k} + u_k b_{\uparrow k}^{+})\, e^{-i\underline{k}\cdot\underline{r}_j} \\ S_j^{-} &= \;\;\text{"}\;\; \sum_k (\sigma_k b_{\downarrow -k}^{+} + u_k b_{\uparrow k})\, e^{i\underline{k}\cdot\underline{r}_j} \end{aligned}\right\} \qquad (2.35)$$

where $$u_k^{2} - v_k^{2} = 1 \qquad (2.36)$$

Equation (2.36) is the condition for the operators to diagonalize H and ensure that the excitation of one magnon

changes S^z by ± 1. Physically, this gives a linear combination of spin excitations on the two lattices. Each magnon changes the z component of spin on one sublattice by $\pm u_k^2$, and of the other by $\mp v_k^2$. In MnF_2 u_k and v_k are both large near the zone centre, so that one magnon of either type perturbs both the sublattices. As $\underline{k}$ approaches the zone boundary, $u_k - 1$ and hence $v_k - 0$, so that zone boundary magnons perturb only one sublattice. This is not generally true for other lattice structures (Fleury and Loudon 1968).

Substituting in H for the spin operators, equations (2.35) give

$$\left.\begin{aligned} \mathcal{H} &= E_0 + \sum_{\underline{k}} \left[E_{\uparrow k} b_{\uparrow k}^{+} b_{\uparrow k} + E_{\downarrow k} b_{\downarrow k}^{+} b_{\downarrow k} \right] \\ \text{where} \quad E_{\downarrow k} &= E_k + g\beta H_0 \\ \text{and} \quad E_{\uparrow k} &= E_k - g\beta H_0 \end{aligned}\right\} \qquad (2.37)$$

Therefore the two-magnon branches are degenerate in zero external magnetic field

$$E_k = \hbar\omega_k = \left[(J(0)S + H_A)^2 - (J(\underline{k})S)^2 \right]^{\frac{1}{2}} \qquad (2.38)$$

Neglecting H_A and the external field (Kittel 1966)

$$\lim_{\underline{k} \to 0} \hbar\omega_k \propto k \qquad (2.39)$$

Thus anti-ferromagnets have a dispersion curve where $\omega \propto k$ near the zone centre, in contrast with ferromagnets.

The zone-centre magnon frequencies in a magnetic field are given by

$$\pm \hbar\omega_{k=0} = \left[(2J(0)S + H_A)H_A\right]^{\frac{1}{2}} \pm g\beta H_0 \qquad (2.40)$$

As the magnetic field increases, the degenerate modes split until one mode reaches zero frequency in a critical field H_c given by

$$H_c = \frac{1}{g\beta}\left[(2J(0)S + H_A)H_A\right]^{\frac{1}{2}} \qquad (2.41)$$

For $H_0 > H_c$ the spins on one sublattice try and realign parallel to the other sublattice. This is the "spin-flop" transition.

2.13 First Order Magnon Light Scattering

For visible light the wavelength is very much greater than the lattice spacing, so that as for phonons, only $\underline{k} \backsimeq 0$ magnons are excited optically. In a ferromagnet, the zone centre magnon has zero frequency unless an external magnetic field is applied, when its energy becomes $\hbar\omega_{k=0} = g\beta H_0$, from equation (2.32). Even in large ($\backsimeq$100kG) magnetic fields this is generally $\lesssim 10\,cm^{-1}$, which is too small to be

easily observed by Raman scattering. However, in antiferromagnets the zone centre magnon can have a large energy (given by equation (2.40)) even when no field is applied, e.g. $\sim 52\text{cm}^{-1}$ in FeF_2 (Chlmann and Tinkham 1961).

In the limit when the wavelength of light is large compared to the lattice parameter it is assumed that the coupling between the radiation and the lattice is through a dipole interaction. This could be an electric dipole interaction,

$$V_{ED} = -e\underline{E}\cdot\sum_i \underline{r}_i \qquad (2.42)$$

or magnetic dipole

$$V_{MD} = -g\beta\underline{H}\cdot\sum_i \underline{S}_i \qquad (2.43)$$

where $\underline{E}$ and $\underline{H}$ are the electric and magnetic vectors respectively of the light. The magnetic dipole interaction obviously gives the more direct coupling to the spins, and it was this mechanism that was first purposed for magnon light scattering by Bass and Kaganov (1959). They used this interaction as a perturbation in second order perturbation theory to calculate the scattering cross section and selection rules for light scattering. However, comparison of their theory with experimental results on FeF_2 (Fleury and Loudon 1968) showed that the predicted cross-section was much too small and the polarization section rules incorrect.

A later theory of Elliott and Loudon (1963) used the electric dipole interaction. This gave a larger cross section, and used an indirect coupling of the electric vector to the spins due to a mixing of the spin and orbital motions. This theory considered magnetic ions with $\langle L \rangle = 0$ in the ground state. This could either be an ion with an S ground state (e.g. Mn^{2+} $S = 5/2$) or an ion in which the orbital motion is quenched by the crystal field (e.g. Fe^{2+} in FeF_2). In either case there can be no splitting of the ground state by the spin-orbit coupling, and the levels with different S^z are split by the exchange interaction. Transitions between these levels are equivalent to the excitation of a magnon. Higher terms (which have $L \neq 0$) will be split by the spin-orbit coupling, and these act as intermediate states for the Raman scattering, where V_{ED} causes dipole transitions between the levels.

This mechanism gives a cross-section and polarization selection rules which are in better agreement with the experimental observations in FeF_2 (Fleury and Loudon 1968).

2.14 Second Order Magnon Light Scattering

The second-order Raman effect involves the creation (or destruction) of pairs of magnons. In common with second order phonon scattering these magnons have approximately equal and opposite wave vectors $\pm \underline{k}$. As the magnon dispersion curves are symmetric in $\underline{k}$ space $\omega(\underline{k}) = \omega(-\underline{k})$.

The actual line shape observed is determined by the density of states and scattering from critical points, as for phonons.

Fleury and Loudon (1968) also observed second order magnon scattering in FeF_2 . This was more intense than the first order scattering, implying that a different mechanism caused the two magnon scattering. If the spin-orbit coupling mechanism had been extended to a higher order to give two magnon scattering, then it would have predicted an intensity less than the first order spectrum.

One possible mechanism is to use the phonon modulation of the exchange. In this theory the incident radiation can be thought of as producing a virtual phonon, (by the usual Raman process) which then decays into two magnons (Fleury and Loudon 1968).

Another method, the so-called exchange scattering mechanism, has been proposed by Fleury and Loudon (1968), and is similar to a technique used by Tanabe et al (1965) for the magnon optical absorption. This uses the exchange operator directly instead of spin-orbit coupling in third-order perturbation theory. Exchange scattering produces magnons in pairs because of a term like $S_i^- S_j^+$, and therefore there is no possibility of this mechanism giving one magnon scattering. It has not proved possible to distinguish these two mechanisms experimentally. (Woods - Halley 1969).

If the lineshapes of the two magnon Raman spectra predicted by these theories are compared with experiment,

poor agreement is obtained. This is due to the omission in the theory of any interaction between the magnons. It has been pointed out that the magnons in second order Raman scattering are produced close together, and so the interactions would be expected to be important (Elliott and Thorpe 1969). A theory accounting for magnon interactions was developed by Elliott and Thorpe (1969) and more recently Natoli and Ranninger (1973). When the interactions are included much better agreement with experiment is obtained.

2.15 Magnons in Mixed Crystals

The recent experimental and theoretical work on mixed magnetic crystals has been reviewed by Cowley and Buyers (1972). Most of the experimental work has concentrated on magnetic impurities. These modify the magnon spectrum in two possible ways. First, they can give rise to a localized excitation at a frequency above the maximum frequency of the host lattice. This is a localized defect mode, equivalent to a local phonon mode. The theory for local modes in an anti-ferromagnet has been worked out by Lovesay (1968). Secondly, impurities can give a resonant band within the frequency band of the host crystal. The review discusses the various theories of magnons in mixed crystals and compares them with the available experimental results.

2.16 Electronic Raman Effect

The electronic eigenfunctions of a free atom can be characterized by the angular momentum of the electrons using the full rotation group, (Tinkham 1964). When such an atom is placed in a crystalline environment the crystal field may raise the degeneracy of some of the energy levels which can then be reclassified in terms of the irreducible representations of the crystal symmetry group. For ions with an odd number of electrons (half-integral angular momentum) the electronic energy levels must be at least doubly degenerate regardless of how low the symmetry is, provided there are no magnetic fields present to remove time reversal symmetry. This is Kramer's Theorem (Kramers 1930).

Raman scattering from the electronic levels of paramagnetic ions was first proposed by Elliott and Loudon (1963). At about the same time Hougen and Singh (1963) reported the measurement of the electronic energy levels of Pr^{3+} in $PrCl_3$ by electronic Raman scattering.

The theory of the electronic Raman effect has been reviewed by Kiel (1969). Second-order perturbation theory is used to derive a transition rate, which is governed by a term like $P(f,g;\nu,\alpha,\beta) \equiv$

$$\frac{e^2}{2}\sum_i \Big[\Big(\frac{1}{E_i-h\nu}+\frac{1}{E_i+h\nu}\Big)\big(\langle f|r_\beta|i\rangle\langle i|r_\alpha|g\rangle+\langle f|r_\alpha|i\rangle\langle i|r_\beta|g\rangle\big) + \Big(\frac{1}{E_i-h\nu}-\frac{1}{E_i+h\nu}\Big)\big(\langle f|r_\beta|i\rangle\langle i|r_\alpha|g\rangle-\langle f|r_\alpha|i\rangle\langle i|r_\beta|g\rangle\big)\Big] \tag{2.44}$$

Where E_i is the energy (above the ground state) of the intermediate state $|i\rangle$; $|g\rangle$ the electronic ground state and $|f\rangle$ the final state. The frequency of the incident

radiation is ν and α and β are the polarization directions of the incident and scattered light respectively.

The form of $P(f,g;\nu,\alpha,\beta)$ is such that it can be written as the sum of a symmetric and anti-symmetric part.

$$P = P_S + P_A \tag{2.45}$$

interchanging α and β

$$P(f,g;\nu,\alpha,\beta) = P(f,g;-\nu,\beta,\alpha) \tag{2.46}$$

Therefore if $h\nu << E_i$ the second (anti-symmetric) term will be zero, and the whole term symmetric, as for phonon scattering. In practice the anti-symmetric term is usually quite large. Even if $h\nu = \frac{1}{2}E_i$, then $P_A = \frac{1}{2} P_S$ and cannot be neglected.

P_A transforms like a magnetic dipole moment. There is a general rule for pairs of states that anti-symmetric terms occur in the scattering tensor whenever magnetic dipole transitions are allowed between the states (Kiel 1969).

The scattering intensity is proportional to $|P|^2$, and therefore if the scattering tensor is purely anti-symmetric there will be no asymmetry in the intensity. In general though, the intensity in ($\alpha\beta$) polarization will be proportional to $|P_S + P_A|^2$, and in ($\beta\alpha$) proportional to $|P_S - P_A|^2$. Maximum asymmetry occurs when either $P(f,g;\nu,\alpha,\beta)$ or $P(f,g;\nu,\beta,\alpha)$ equals zero.

Comparing the Stokes and Anti-Stokes intensities, it

can be shown that

$$P(g,f;\nu,\alpha,\beta) = P(f,g;\nu,\beta,\alpha) \qquad (2.47)$$

(Kiel 1969). This is a necessary condition for the system to be thermodynamically stable.

The selection rules are slightly more complicated for the electronic Raman effect than in the phonon case. This is because the ground state $|g\rangle$ need no longer transform like the identical representation, and the representations of levels for odd-electron ions will be double valued (from Kramer's Theorem). The selection rules are based on group theory; the requirement for the transition rate to be non-zero is that the matrix elements satisfy the integral theorem of group theory (Tinkham 1964). Suppose that for a given symmetry, the polarization tensor is reduced to the sum of irreducible representations Γ_p, of that group. This will be the same set of tensors as listed for phonons by Loudon (1964). If the ground state belongs to the irreducible representation Γ_g and the final state to Γ_f, then the direct product can be written as

$$\Gamma_g \times \Gamma_f = \sum \Gamma_h \qquad (2.48)$$

Then if the particular Γ_p occurs among the $\sum \Gamma_h$ the polarization components of Γ_p should appear in the Raman scattering. Complete tables for the electronic Raman effect selection rules are given by Kiel and Porto (1969).

Electronic Raman scattering has proved to be a useful

technique for studying low lying electronic energy levels. Most of the experimental work on insulators seems to have been concentrated on the Rare Earth ions (Boal, Grunberg and Kohingstein 1973 , and references therein). The Raman effect enables transitions between states of the same parity to be observed, which could only be seen in direct absorption by electric quadrupole or magnetic dipole interactions, which are both much weaker. It has certain advantages over fluorescence, in that there is no need to determine separately the initial or terminal states, so that the spectra are easier to interpret. Also it gives more information because of its polarization, particularly in cubic crystals where fluorescence is unpolarized but the Raman spectra is still polarized (Boal, Grunberg and Koningstein 1973). Finally, electronic Raman scattering experiments can be performed on much smaller crystals than are necessary for absorption work.

CHAPTER THREE

EXPERIMENTAL TECHNIQUES

3.1 Introduction

The practical requirements for performing Raman scattering experiments are (1) a light source, (2) an analysing system (Spectrometer) and (3) a detector and recorder. In order to study the spectra at low temperatures, the sample must be contained in a suitable cryostat, and lenses are needed to couple together optically the light source, sample and spectrometer. The general scheme of the system is shown in Fig. 3.1., and the components are dealt with separately below.

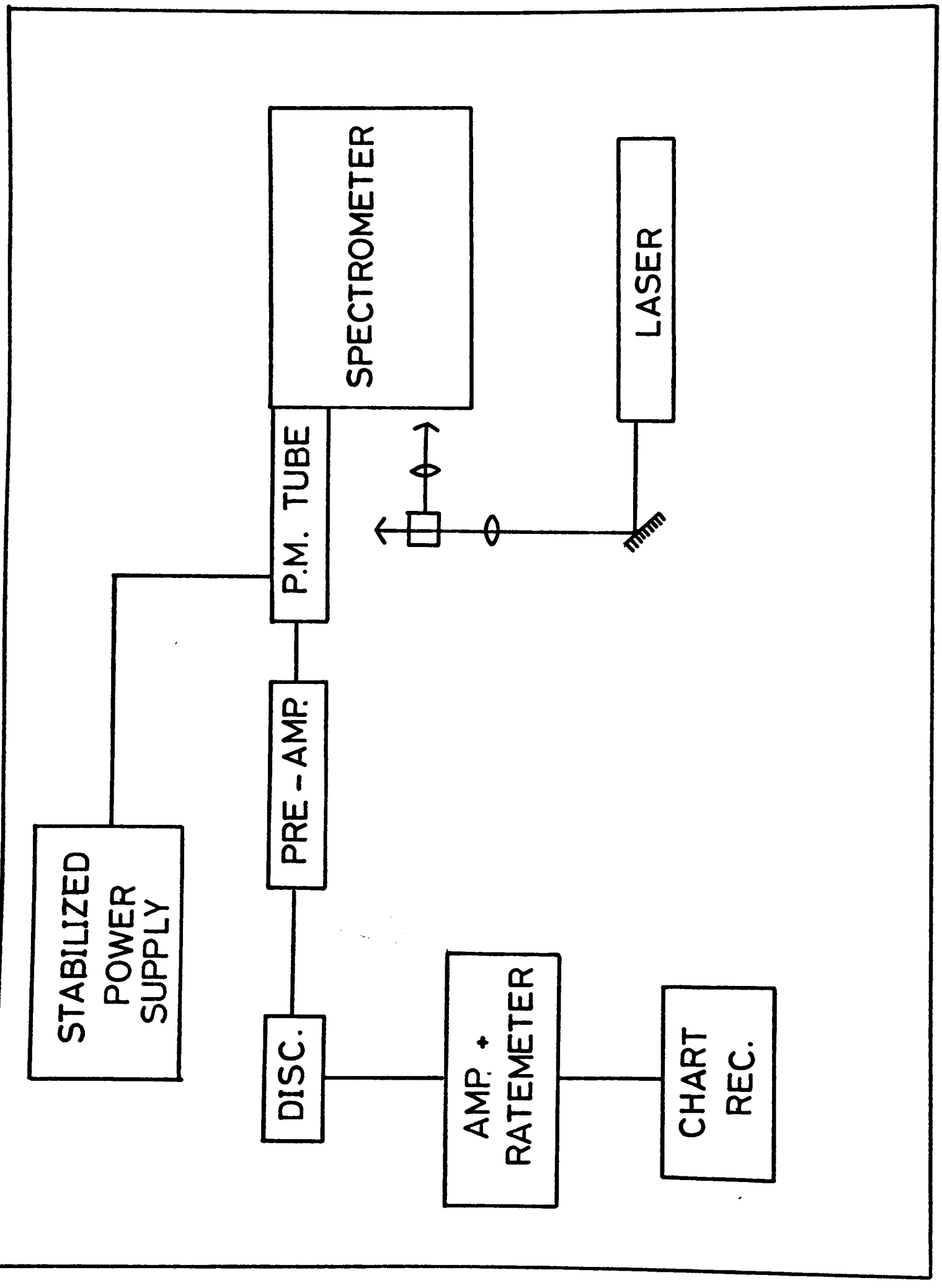
3.2 The Laser

The Raman scattering cross section of most materials is small, so that an intense light source is needed to observe the effect. The source must be highly monochromatic and for polarization studies should be well collimated and polarized. All these requirements are satisfied by a laser, and today lasers are used almost exclusively as the light sources for Raman scattering.

The laser used in all the experiments in this thesis was a "Coherent Radiation Laboratories" Argon-Ion laser, which produced about 1 W. maximum power at each of the two main wavelengths, (514.5 and 488.0nm.) The laser was used without an intercavity etalon, and hence oscillated in several modes simultaneously. However, the line width was still $< 0.1 cm^{-1}$

Fig. 3.1.

Schematic layout of Raman scattering apparatus.



which was quite adequate. After an initial warm-up period of about half-an-hour power output was stable over a period of several hours.

The laser light was polarized with the electric vector vertical, and was reflected on to the sample by a system of plane mirrors. The mirror system enabled the laser light striking the sample to be polarized either parallel or perpendicular to the spectrometer axis. The light was finally focused onto the sample by means of a 5cm focal length lens.

3.3 The Spectrometer

All the crystals were transparent, so a 90° scattering geometry was used. This arrangement minimized the intensity of the Rayleigh scattered light entering the spectrometer. The light scattered at right-angles by the sample was focused by means of an f/2.4 lens onto the entrance slit of a "Spex 1401" double monochrometer. This was a $\frac{1}{4}$m. double grating spectrometer of the Czerny-Turner type with gratings of 1200g/mm blazed at 500nm. As the frequency- shifted components of the scattered light were very weak compared to the unshifted Rayleigh line, it was necessary to use a monochrometer with a high dispersion and resolution. A double monochrometer has effectively twice the resolution and dispersion of each monochrometer used singly. This reduced the background of light

due to random scattering from the intense Rayleigh line within the instrument sufficiently so that the Raman lines were not obscured. A high resolution was also desirable in that features of the Raman spectra could be discerned closer to the excitation frequency.

To fully utilise the resolution of the gratings, the angle of the light cone passing through the extrance slits had to be such as to just fill the first diffrection grating. According to the manufacturers, this required the light to diverge at an angle of 8^{o} after entering the spectrometer. This angle, together with the aperture (f/2.4) and focal length of the collecting lens were sufficient to determine the sample-slits distance and the lens position.

A polarizer could be fitted in front of the entrance slits for polarization measurements. To overcome the problem of differing reflection coefficients from the gratings for vertical and horizontal polarized light, a quartz wedge (a "scrambler") was permanently fixed in front of the slits. This had the property of converting the light to a circular polarization, so that intensities in different polarizations could be directly compared.

It was obviously desirable to optimize both the amount of light passing through the spectrometer and the resolution. Although the amount of light could have been increased by increasing the slit widths, this would have had an adverse effect on the resolution. The resolution was mainly determined

by the exit slit and this was kept as narrow as possible while a compromise was reached between resolution and intensity to determine the other slit widths. It was advantageous to have a reasonably wide intermediate slit, as this improved the stability of the instruments - i.e. prevented intensity changes for a given wavelength with drift in temperature

As the line width of the laser was very much less than the spectrometer resolution, the resolution could be measured directly by scanning through the laser frequency (with the beam suitably attenuated.) The observed resolution for the two most commonly used slit settings are given below.

Entrance Slit Ht. (m.m.)	Inter Slit Width (μ)	Exit Slit (μ)	Resolution (cm^{-1})
5	100	200	100	3·0
2	50	100	50	0·8

The entrance slit height had some effect on the resolution, as aberrations in the spectrometer optics caused the final image on the straight exit slits to be slightly curved. To compensate for slight temperature drift in the spectrometer calibration the laser frequency was measured at the beginning and end of every experiment. The scanning rate of the spectrometer could be varied over a wide range.

3.4 The Detection System

The detection system is shown schematically in Fig. 3.1. The photomultiplier tube was an ITT FW 130 type,

and the electronics standard Harwell 2000 series with a "Servoscribe" chart recorder. Of the three main methods of detection, pulse counting, D.C. measurement and synchronous detection, it has been shown that at the low light levels involved in Raman scattering, pulse counting gives the best signal to noise ratio, S/N (Morton 1968; Nakamura and Scharz 1968). Hence this was the method chosen.

Consider the workings of a photomultiplier tube. When a photon strikes the photocathode, an electron is emitted which is collected by the first dynode. This emits secondary electrons which are collected by the next dynode - the process continuing along the chain until a pulse of current is emitted from the anode. Ideally, every photon would produce an identical pulse, and one would only have to count these pulses to measure the light intensity.

In practice, not all photons produce electrons at the cathode. The percentage that does (called Quantum Efficiency) is a function of the wavelength of the light. It was therefore important to choose a photomultiplier tube with a cathode giving a high quantum efficiency in the visible region. Also, as the electron multiplication process through the tube is a statistical one, there is a variation of pulse heights. Even when the tube was not illuminated pulses were still observed. These were of two types, very small pulses due to thermionic emission in the tube (Morton 1968) and pulses much larger than typical photons produced, probably due to background radio-activity. Obviously if some of these spurious pulses could be

removed without affecting the signal pulses, S/N would be increased. This was achieved by feeding the output from the tube (via a pre-amplifier) to the discriminator which passed only pulses above a certain height, which could be varied. This discriminator setting was determined as follows:- With the tube illuminated at a constant intensity the count rate was measured as a function of the discriminator setting. For low settings, when almost all pulses were counted, the count rate was very high and fell rapidly with increasing discrimination level. At a certain level the count rate began to fall less rapidly as all the small noise pulses were blocked. It was at this "knee" in the curve that the discriminator was set. These small noise pulses originated both in the tube itself and in the pre-amplifier. Very few spurious pulses larger than the mean signal height were found, so that an upper cut-off level on the discriminator was not used.

The two other factors influencing S/N were the temperature and the operating voltage. A decrease in the temperature led to a reduction in the dark count, by reducing thermionic emission. However, this gave only a small increase in S/N due to the decreased sensitivity and the statistical behaviour of the tube's output becoming more erratic. Increasing the tube voltage increased the dark count faster than the gain. Also it caused the randomness of the dark count to increase rapidly, both factors tending to reduce S/N. Hence the tube was used at the lowest practical voltage, 2000v.

The photomultiplier tube used had a high quantum efficiency and a low dark count and thermal emission. It was found to be worthwhile cooling the tube to about $-40^{\circ}C$, (Thermoelectrically), when the dark count could be reduced to about 1 count sec^{-1}. A stabilized power supply was used to minimize noise from this source, and it was necessary to screen the pre-amplifier efficiently to prevent pick-up of electrical noise.

The signal was fed into an amplifier and ratemeter, and the output recorded on a strip chart recorder. A marking device in the spectrometer indicated $10cm^{-1}$ intervals on the chart. The ratemeter consisted essentially of an RC integrating circuit, whose sensitivity and time constant could be varied over a wide range. To prevent the signal to the chart recorder being overdamped, the scanning rate of the spectrometer for a given slit width and time constant was determined by the following "rule of thumb"

$$\text{Scanning speed} \leq \frac{\text{Resolution}}{5 \times (\text{Time constant})}$$

3.5 Variable Temperature Cryostat

The low temperature spectra were obtained with the sample mounted in a conventional variable temperature cryostat Fig. 3.2. Details of the sample mounting are shown in Fig. 3.3. The sample was cooled by being brought into

Fig. 3.2.

The Variable-temperature cryostat.

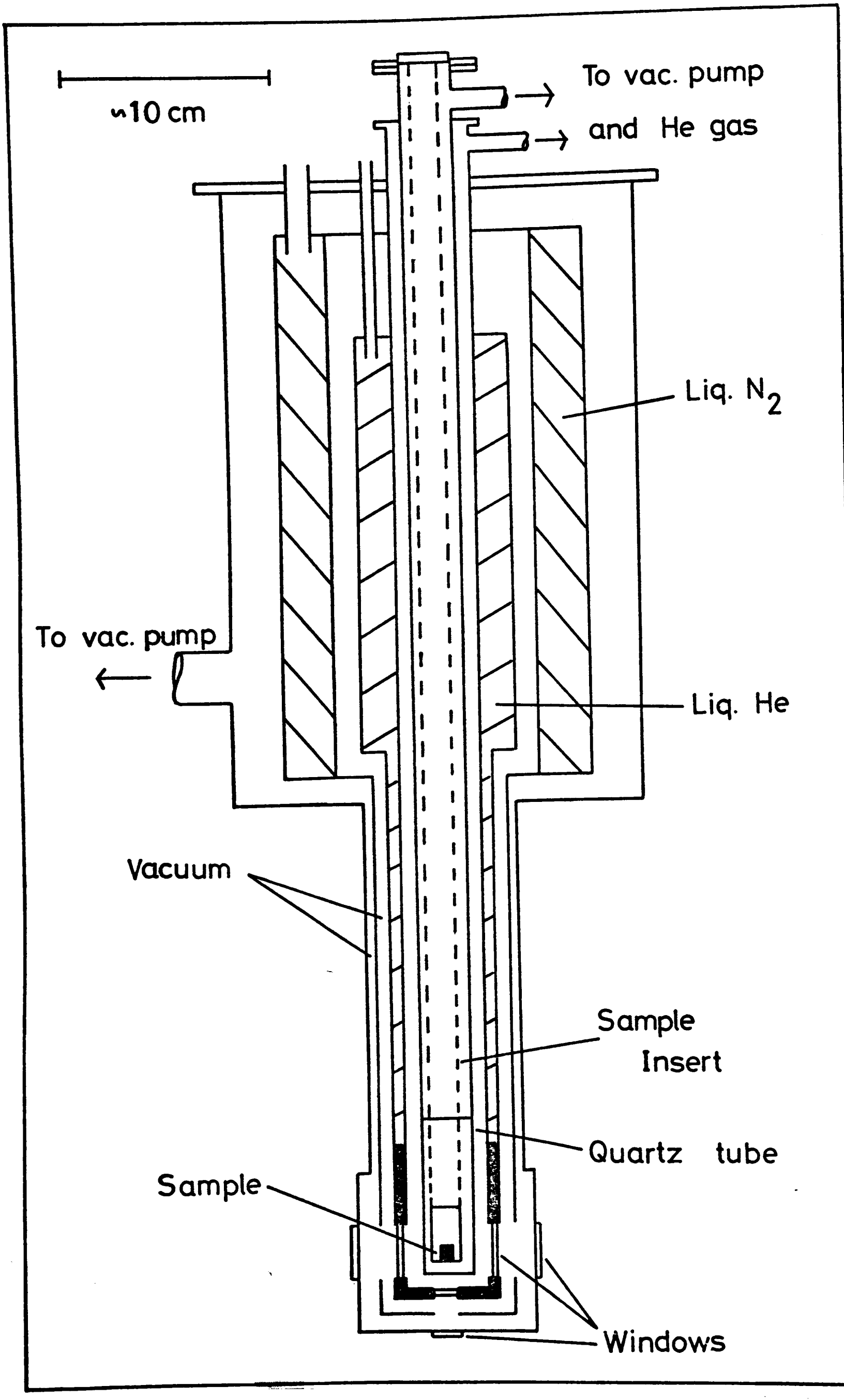
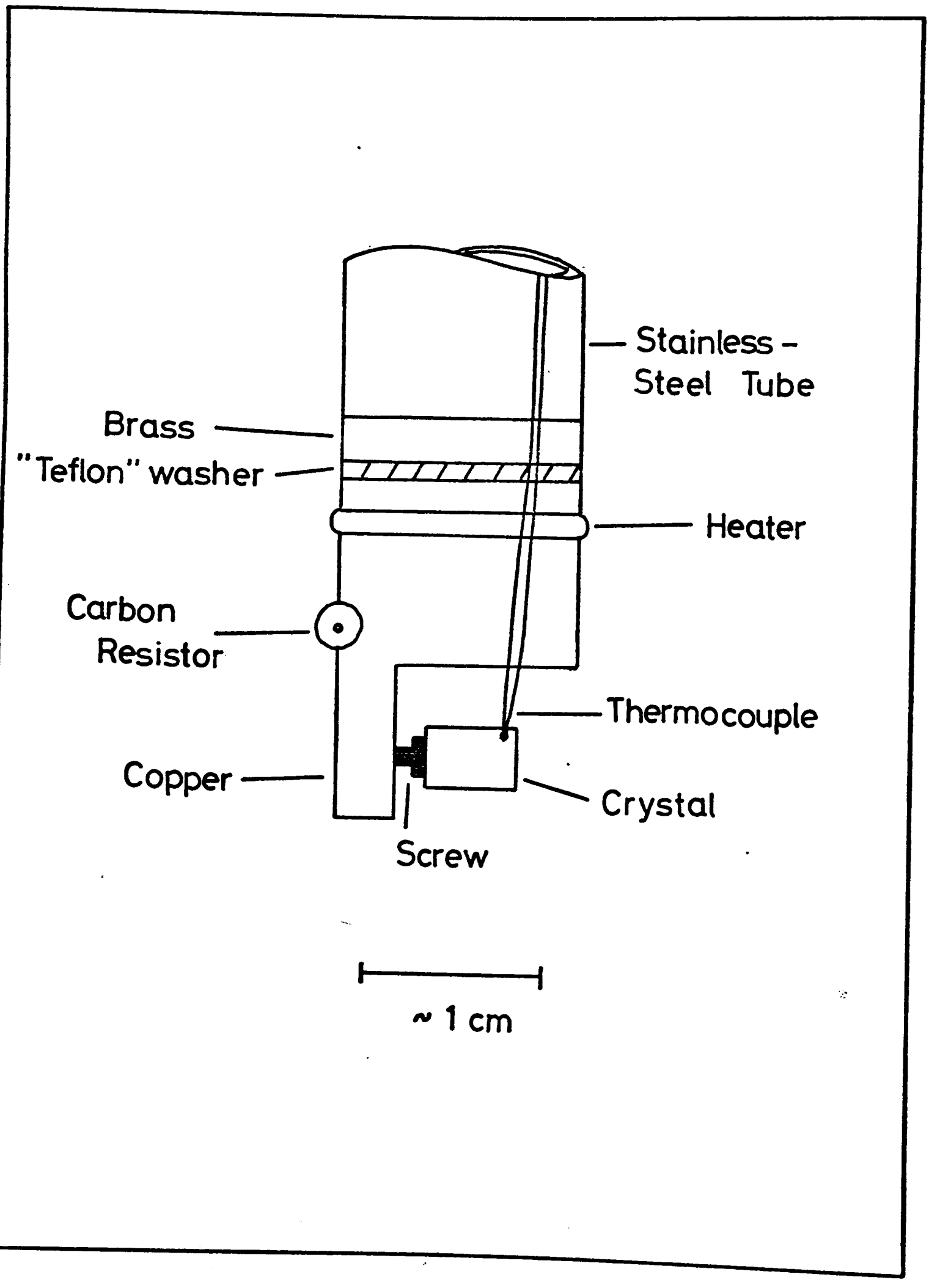


Fig. 3.3.

Detail of sample mounting in variable temperature cryostat.



thermal contact with the refrigerant through helium gas inside and outside the quartz tube. To measure the sample temperature a Gold/Copper thermocouple junction was attached directly to the crystal. For temperature measurements below about $4^{o}K$ an "Allan-Bradley" 350Ω carbon resistor was used, as the thermocouple became insensitive in this region. This was also used at higher temperatures to stabilize the temperature with the temperature controller. In order to vary the sample temperature, a small wire-wound heater was incorporated in the sample mounting. So that all these components were in good thermal contact, the end of the sample insert was made from copper, and to prevent excessive heat leaks along the stainless steel tube it was thermally insulated by a thin "Teflon" washer. The space outside the quartz tube could be evacuated so that the sample temperature could be raised while still keeping the sample, heater and thermocouple in good thermal contact through the surrounding helium gas.

For experiments at a fixed temperature the insert and quartz tube were removed and a similar, but slightly larger diameter, insert used. This prevented losses of scattered light from the quartz, and brought the sample into better thermal contact with the refrigerant. In all cases the sample was glued lightly to the insert.

Temperatures below $4.2^{o}K$ were obtained by pumping on the liquid helium. Both the carbon resistance thermometer and the helium vapour pressure indicated a minimum temperature of $1.7^{o}K$. The helium exchange gas around the sample condensed

and this prevented experiments in the range 2.1° to 4.2°K. as the bubbles in the liquid scattered the laser beam until at the λ- point (2.1°K) the helium was superfluid and free from bubbles.

The emf. of the calibrated thermocouple was measured with a potentiometer, giving an accuracy of $\pm$ 0.5°K. The carbon resistance was measured with an A.C. Wheatstone bridge, and was very sensitive to small changes in temperature. The off-balance current from the bridge was used to control the heater current, thus stabilizing the temperature. Both the A.C. bridge and the heater unit were designed and built by the Electronics Workshop in this laboratory. The stability obtained was within the accuracy of the thermocouple.

In most experiments the laser caused some local heating in the crystal. Ultimately, the accuracy of the temperature measurement depended on the determination of the local heating rather than the accuracy of the thermocouple.

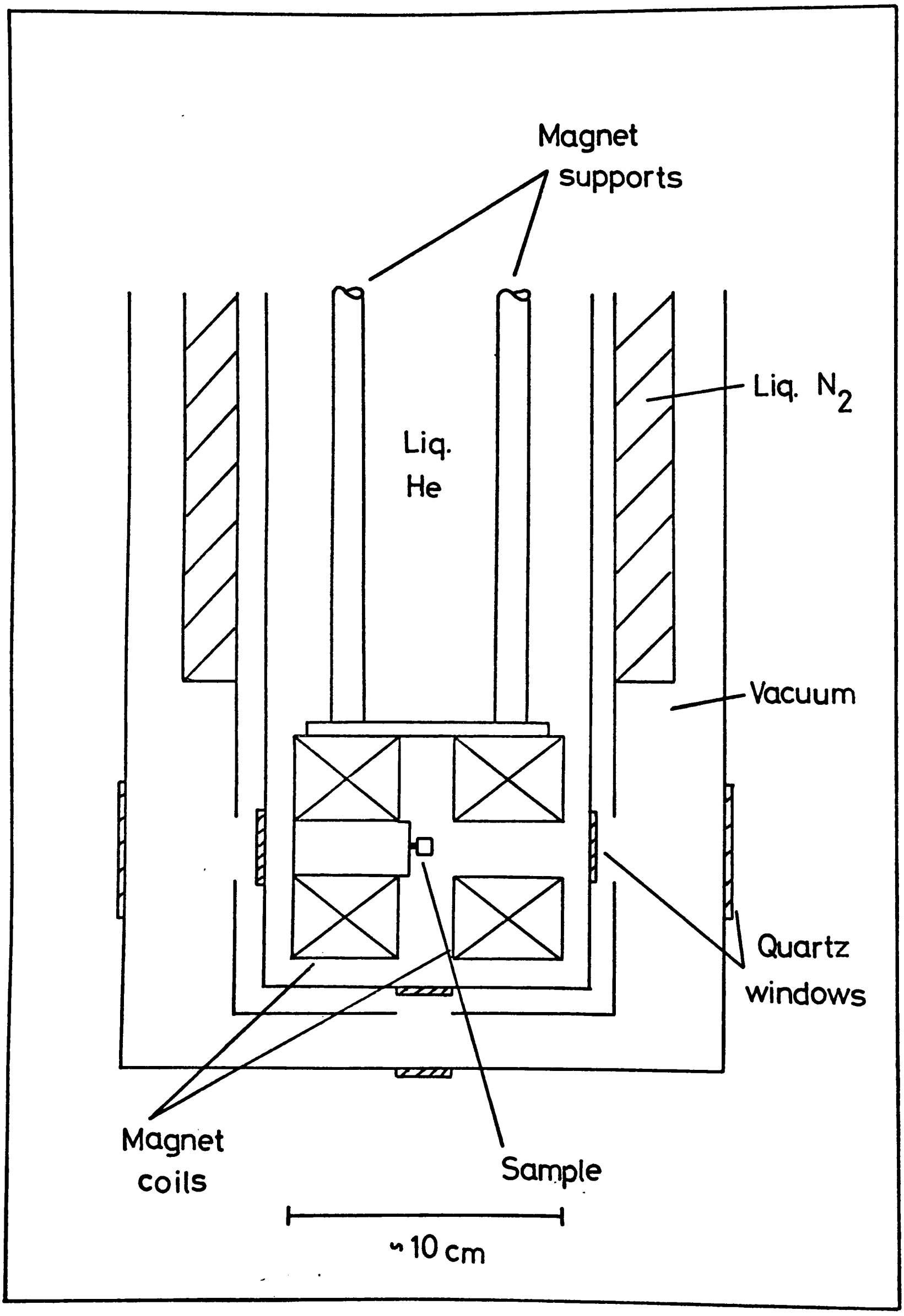
3.6 Superconducting Magnet Dewar

A superconducting magnet built in this laboratory was used to obtain Raman spectra in magnetic fields up to $\sim$65kG. It consisted of a split coil of Niobium/Titanium wire immersed in superfluid helium at about 2°K, and is shown schematically in Fig. 3.4.

The sample was mounted at the centre of the coils, and

Fig. 3.4.

Detail of lower part of superconducting magnet dewar.



was in direct contact with the liquid helium. To obtain spectra at higher temperatures the crystal was glued to an insert within a quartz tube similar to that used in the variable temperature cryostat. Temperatures up to about 10°K could be reached in this way. With the liquid helium in direct contact with the outside of the quartz tube it was impossible to reach higher temperatures without producing large temperature gradients in the sample region, which made the temperature measurement uncertain. In practice, it was found to be more satisfactory to obtain the spectra at 2°K whenever possible.

The incident laser beam reached the sample vertically through a hole in the magnet mounting. Scattered light parallel to the direction of the magnetic field passed along the bore of the magnet and emerged through a window in the dewar The collection angle of this arrangement corresponded to approximately f/2.5.

Current for the magnet was derived from a 70amp. power supply, via a control unit and sweep unit. The sweep unit enabled the current to be increased at a constant rate to a predetermined value and then held constant. The magnetic field was measured using a small Hall probe mounted directly behind the sample. The Hall probe was calibrated against a proton magnetometer using a search coil as follows. The search coil was placed in a conventional electromagnet and calibrated against a proton magnetometer. The total induced current in the coil was measured with an integrating digital

voltmeter. Then the search coil was mounted in the superconducting magnet and the Hall probe calibrated.

The superconducting magnet was used only in the experiments on TbF_3, described in the Appendix, and hence just a brief description of the apparatus has been given.

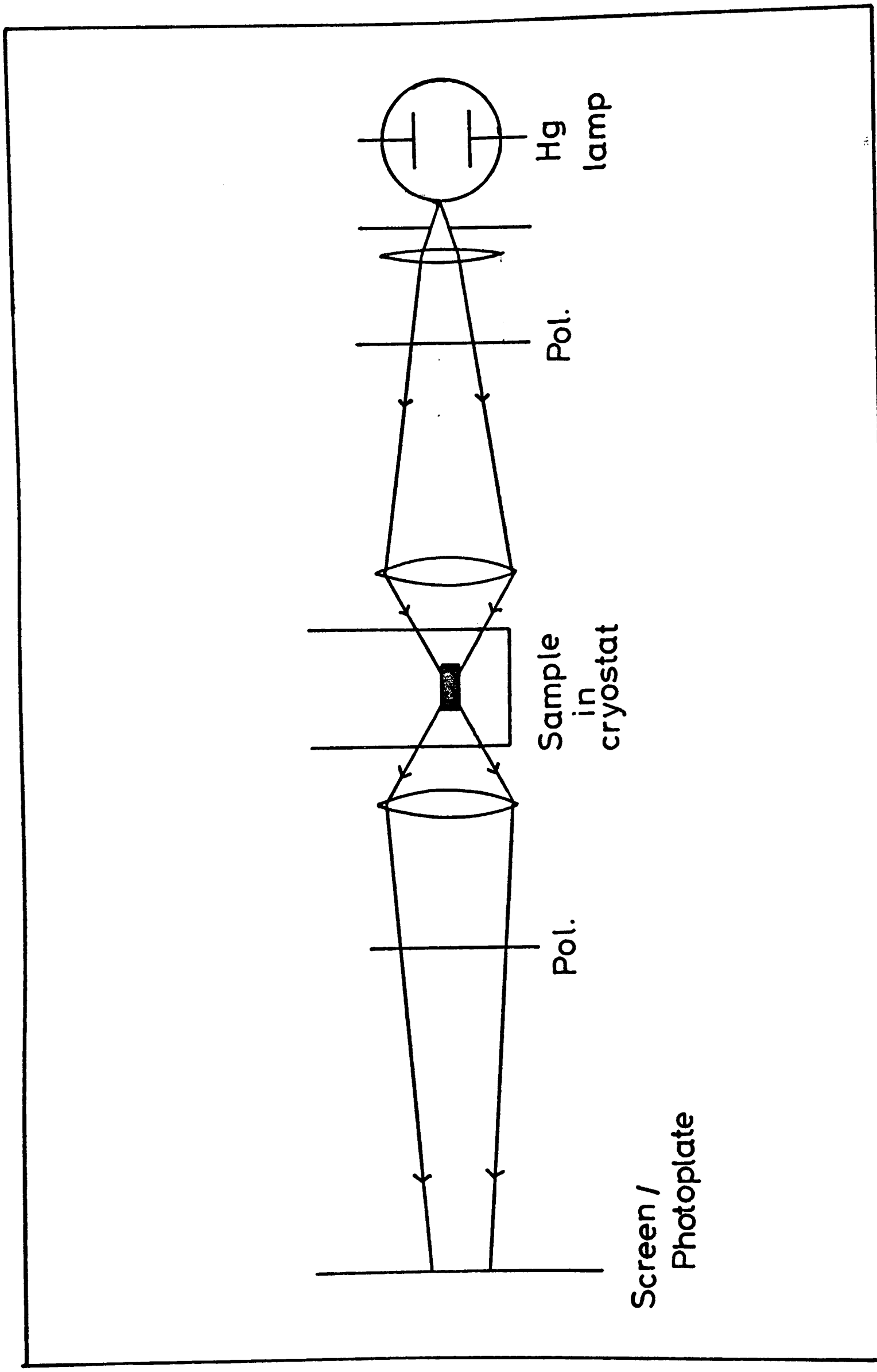
3.7 Optical Birefringence Experiments

This method, based on the interference of convergent polarized light, was used to determine the transition temperature of the $(TbGd)VO_4$ crystals (Chapter 5). The type of interference pattern produced depends on whether the crystal is uniaxial or biaxial. As the lowering of the symmetry from D_{4h} to D_{2h} at the phase transition causes the crystal to change from uniaxial to biaxial, the change in the interference pattern enables the transition to be detected. The theory of birefringence is discussed by Jenkins and White (1957), and this technique has been used recently to study the phase transition in $TmVO_4$ (Becker et al 1972).

The apparatus used in these experiments is shown in Fig. 3.5. The sample was mounted in the cryostat described in section 3.5. To avoid straining the crystal, it was not held rigidly in any way, but just rested in the groove of a small screw head. The point light source was a mercury lamp, made approximately monochromatic by the use of filters. After passing through a polarizer the light was

Fig. 3.5.

Schematic diagram showing layout used for optical birefringence experiments.



focused onto the sample by a combination of lenses whose combined focal length was approximately 5cm. The light passed along the tetragonal (optic) axis of the crystal and was collected by a second lens. After passing through a second polarizer an interference pattern was produced on the screen (which was replaced by a photographic plate for recording the patterns).

It was found to be important that the mean direction of the light was accurately aligned with the optic axis of the crystal, as small deviations produced changes in the pattern. The lenses were arranged so that small adjustments to their positions could be made to facilitate this alignment. Monochromatic light was used, as with white light chromatic aberration in the system caused blurring of the interference pattern. Temperatures above $4^{o}K$ were measured with the thermocouple, which was stuck onto the brass screwhead as close to the sample as possible, and below $4^{o}K$ from the helium vapour pressure. The heating due to the light was negligible.

The results of these experiments are discussed in Chapter 5.

CHAPTER FOUR

EXPERIMENTS ON

PRASEODYMIUM ALUMINATE

4.1 Introduction

$PrAlO_3$ has been found to undergo several structural phase transitions below room temperature which do not have counterparts in any other perovskite crystal. At room temperature the structure is the trigonal distortion (D_{3d}^6) of the cubic perovskite structure (O_h^1) which is caused by the collapse of the Γ_{25} R-point phonon at a temperature (1320°K) just below the melting point (Scott 1969). This trigonal structure is shared by La, Ce and Nd aluminates, but these compounds retain it down to 0°K. Cohen et al (1969), found that when $PrAlO_3$ is cooled below room temperature it undergoes a first-order phase change at 205°K (T_1) to an orthorhombic structure (C_{2h}^3) and a second-order transition at 151°K, (T_2) to a triclinic phase of C_i^1 symmetry. These phase transitions have previously been studied using Raman scattering (Finkman et al 1971), optical absorption and electric and magnetic susceptibility methods (Cohen et al 1969). X-ray determinations of the structures have been carried out at 172°K in the orthorhombic phase and at 135°K in the triclinic phase (Burbank 1970). So far, no X-ray determination of the structure at helium temperatures has been reported, but it has been found in the Raman and optical absorption experiments that below 77°K there is no apparent deviation from tetragonal symmetry. The crystal appears to have a number of domains at low temperature. Cohen found that a single crystal of $PrAlO_3$ at room temperature became twinned below 205°K, and that the domain boundaries moved with temperature. At 151°K

a new set of domains appeared, until at about 80°K the crystal again became a single domain. The domain at 80°K could be re-oriented by the application of a magnetic field. (Riseberg et al 1969; Finkman et al 1971).

This chapter describes the results and interpretation of some Raman scattering experiments on $PrAlO_3$ between 4.2°K and 300°K. These spectra confirm the results of other Raman scattering experiments, and were obtained independently in 1971. The two phase transitions were found to occur at 196 ± 5°K and 146 ± 5°K, slightly lower than the values obtained by Cohen et al (1969). Below 99°K no deviation from tetragonal symmetry could be detected from the Raman spectra. Later Raman scattering experiments were done on small crystals which had larger domains then the original crystal. This allowed a detailed study of the anomalous behaviour of some of the low frequency Raman lines in the vicinity of the 146°K phase transition to be made. Some of these lines were identified as coupled electron-phonon lines from a study of their polarizations. The Raman spectra are discussed in detail in the next section; most of these results have been published recently (Harley et al 1973(a).)

Sections 4.3 and 4.4 describe the results of some optical fluorescence and EPR experiments on $PrAlO_3$ (Harley et al 1973(a).) A molecular field model of $PrAlO_3$ was developed by Smith (Harley et al 1973(a)) which accounts qualitatively for the observed behaviour. The theory of this model is reviewed in section 4.5. Finally, a critical

discussion of the experimental results and theory is given in section 4.6.

While all the results of these Raman, fluorescence and EPR experiments indicate that $PrAlO_3$ has tetragonal symmetry below 99°K, Birgeneau et al using EPR and neutron scattering, have found small deviations from tetragonal symmetry even at very low temperatures (private communication to W. Hayes).

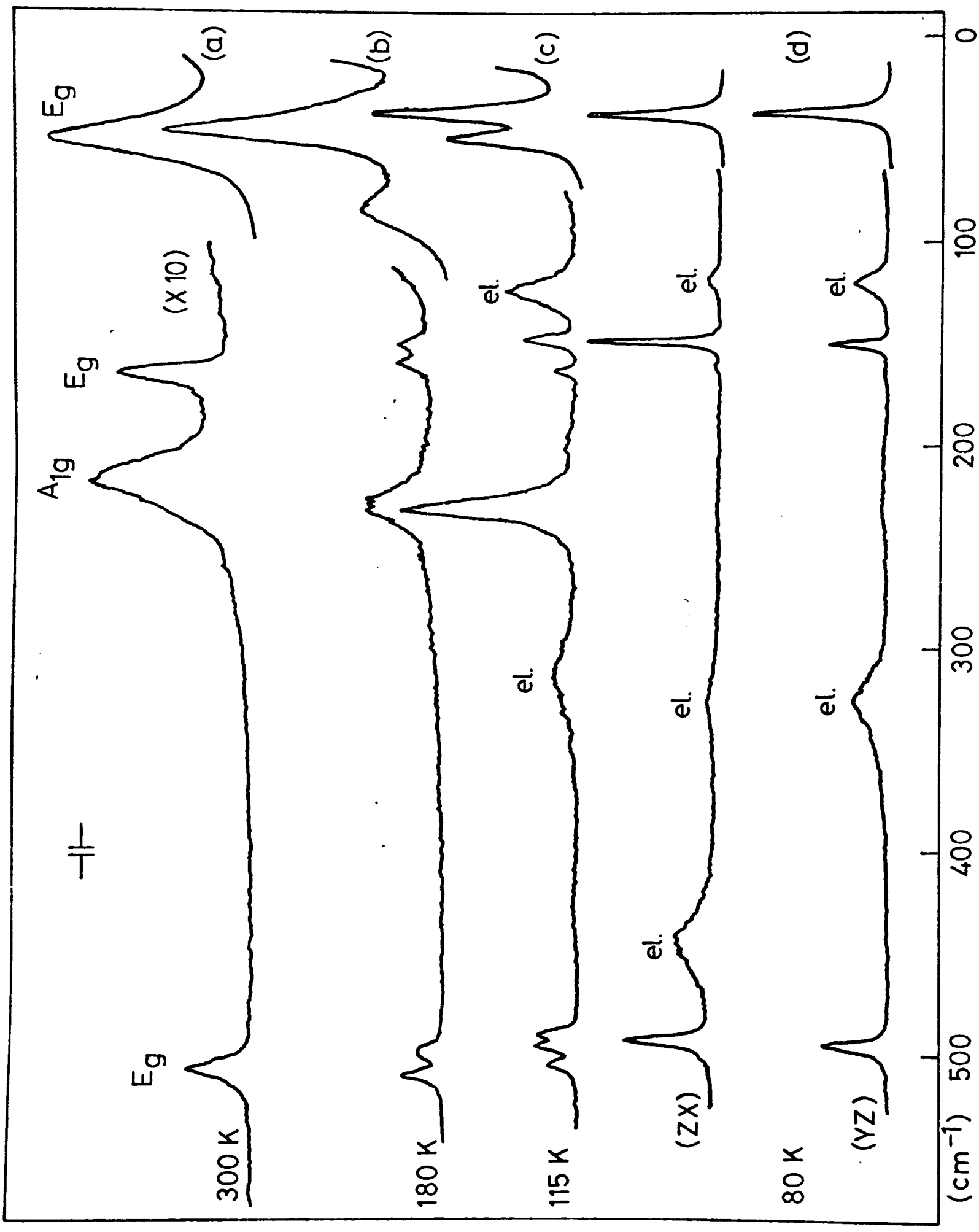
All the samples of $PrAlO_3$ were flux grown in this laboratory by Mrs. B.M.Wanklyn and were of good optical quality with rectangular faces perpendicular to the tetragonal axes of the cubic perovskite structure.

4.2 Raman Spectra

The Raman spectra were obtained with the crystal mounted in the variable temperature cryostat described in Chapter 3, using about 500mW of 514.5 nm radiation from the Argon-ion laser. Although temperatures were measured by a thermocouple in direct contact with the crystal, the accuracy of temperature measurement was only $\pm 5^{\circ}K$ due to local heating of the sample by the focused laser beam.

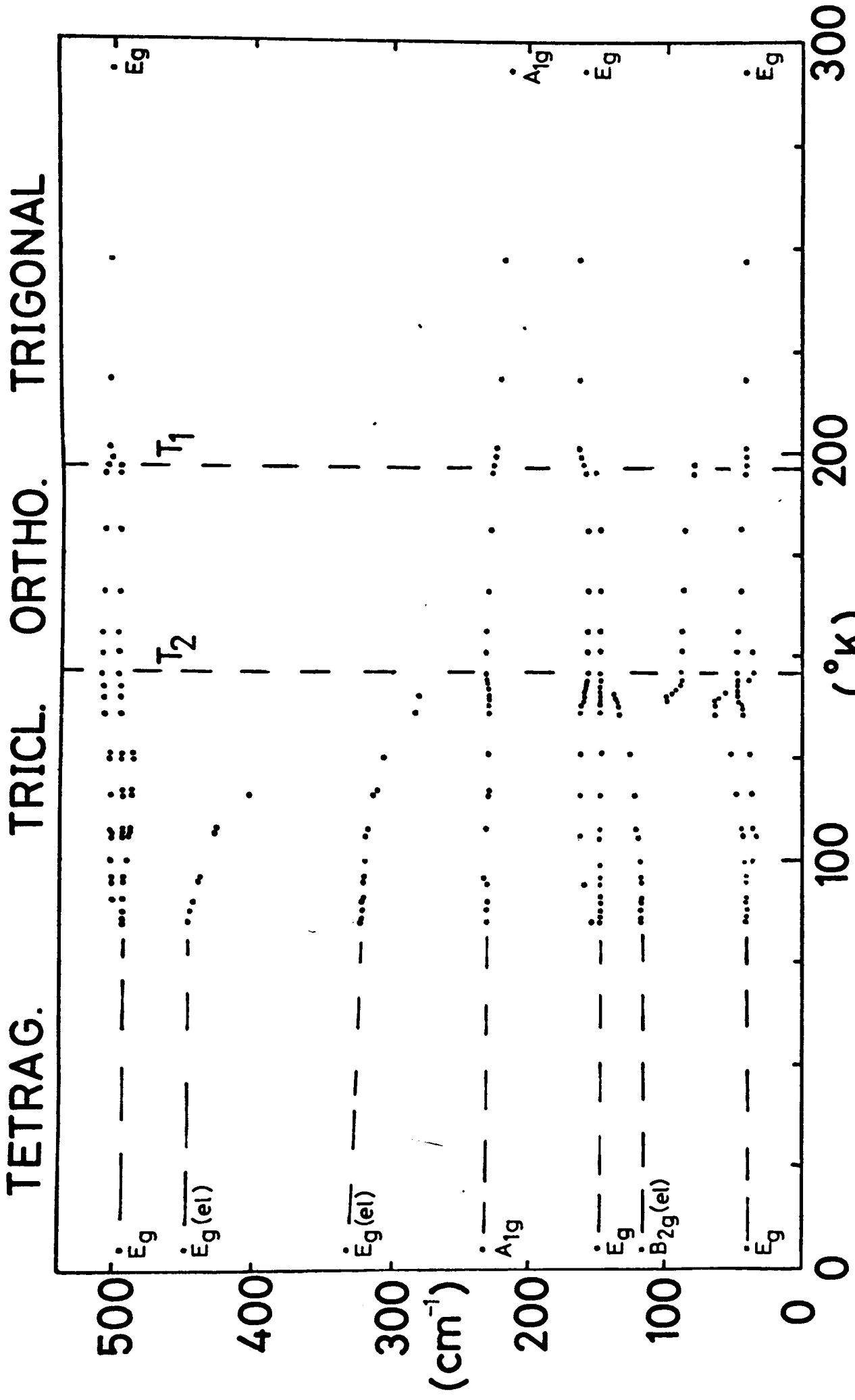
Raman spectra of $PrAlO_3$ at 300°K, 180°K, 115°K and 80°K are shown in Fig. 4.1. and the positions of the observed lines are plotted against temperature in Fig. 4.2. These results agree quite closely with those of Finkman et al (1971).

Fig. 4.1.



Raman spectra of $PrAlO_3$ at various temperatures. Symmetries of the modes at 300°K are indicated and electronic lines are denoted by el. The lowest frequency electronic line appearing in the 80°K spectra is caused by leakage of the intense B_{2g} electronic mode.

Fig. 4.2.



Positions of Raman lines in $PrAlO_3$ as a function of temperature. Electronic lines are denoted by el; and the dashed lines represent interpolations between the measurements at 4°K and 80°K.

In the trigonal phase ($T > T_1$) the sample consisted of a few relatively large domains whose trigonal axes lay along one of the body diagonals of the cubic perovskite lattice. Thus it was possible to determine the symmetries of the four observed lines, which were all due to phonons, from their polarizations; the symmetries are given in Fig. 4.1a and on the right hand side of Fig. 4.2 and refer to the group D_{3d}^6 of the trigonal phase. There are three Eg and one A_{1g} phonons, and they correspond closely in frequency and intensity with lines observed in $NdAlO_3$ (Scott (1969), Finkman et al (1971),)

Between the first-order phase transition (T_1) and 99°K the spectra (Figs. 4.1b and c; Fig. 4.2) were unpolarized so that assignment of symmetries was not possible. In this region the crystal assumed multidomain structures (Cohen et al 1969). However, later experiments were performed on a much smaller crystal which appeared to be almost single domain in this temperature range, and some polarization data obtained. These results are described later in this section.

Below 99°K the spectra (Figs. 4.1d and e; Fig. 4.2) were polarized and, within the experimental uncertainty, two of the original perovskite axes were equivalent and the third unique (see also Finkman et al 1971). In other words, taking axes x, y and z normal to the crystal faces, it was found that if spectra were recorded for xz, yz and xy polarizations, then within experimental uncertainties, two of the spectra were identical and the third different; a similar result held for

the xx, yy and zz spectra. The crystal thus appeared to be tetragonal and consisted of a few relatively large domains with tetragonal axes oriented along (100) type axes of the cubic perovskite lattice. The observed lines can be assigned to modes of the symmetries indicated on the left hand side of Fig. 4.2, where the representation labels refer to the group D_{4h} ; z was taken as the tetragonal axis and x and y were therefore equivalent. Under this nomenclature, the B_{1g} and B_{2g} modes had symmetries (xx-yy) and (xy) respectively.

At helium temperature and 80°K four intense lines corresponded quite closely in energies with the four phonon lines observed at room temperature and had the same degeneracies (three E_g and one A_{1g}, see Figs. 4.1 and 4.2). These lines were therefore interpreted as due to phonons. The remaining three lines at helium temperature were assigned to electronic modes (two E_g(el) and one B_{2g}(el), see Fig. 4.2) because they corresponded closely to the energies of electronic transitions within the $^3H_4$ ground manifold of Pr^{3+} determined by fluorescence (section 4.3) and because the two E_g(el) modes had asymmetric Raman tensors (xz intensities not equal to zx) The E_g(el) modes are $\backsim 40cm^{-1}$ wide (see Figs. 4.1d and e).

Evidence that at low temperatures $PrAlO_3$ is tetragonal (within the accuracy of Raman measurements), comes from the behaviour of the E_g phonon lines as the temperature is raised. Below 90°K they appeared as single, symmetric unsplit lines with widths $\lesssim 3cm^{-1}$. At 99 ± 5°K the modes at $39cm^{-1}$ and $494cm^{-1}$ were observed to split, indicating that below 99°K

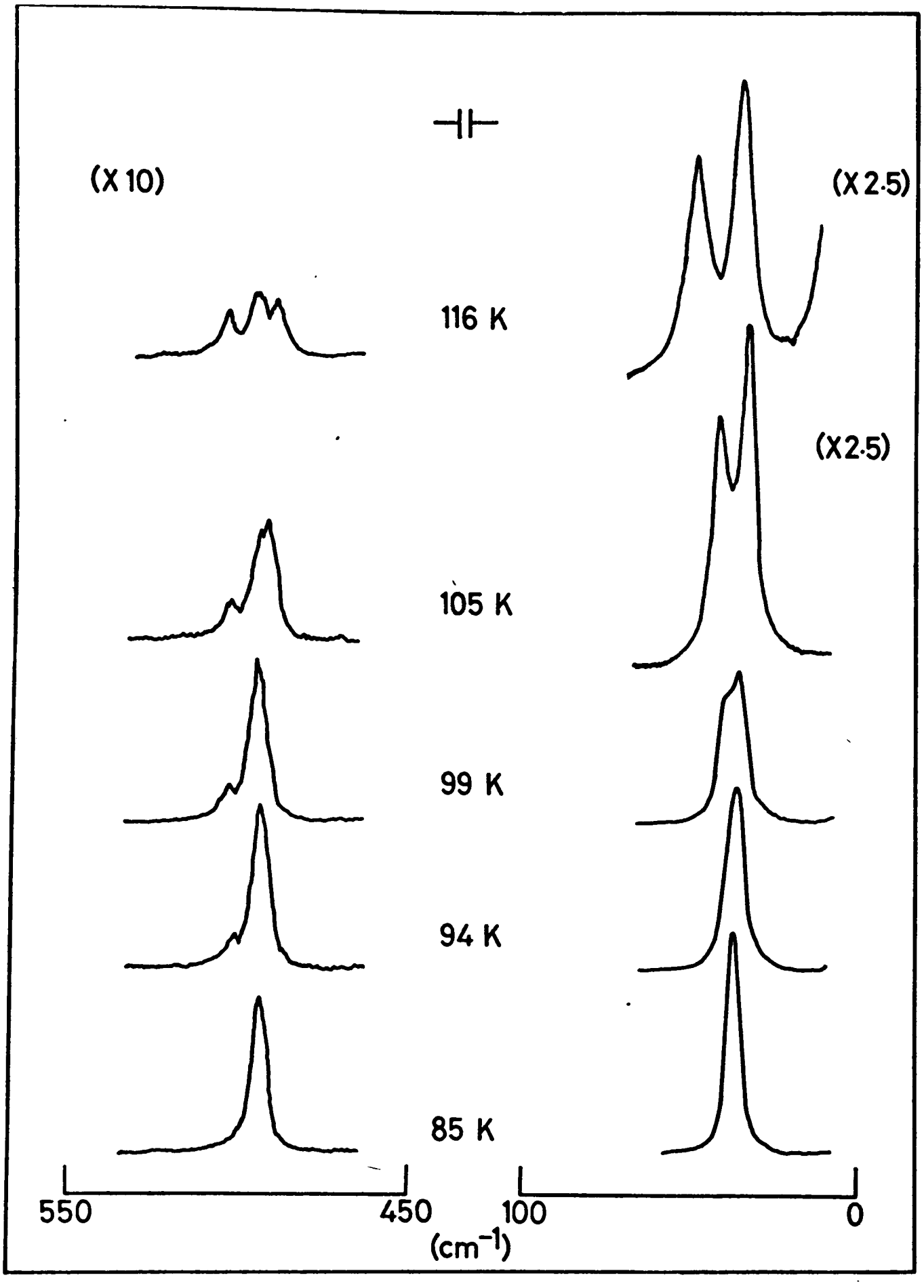
they were degenerate and hence that the lattice contained a fourfold symmetry axis (see also section 4.4) The splitting of these modes is illustrated in Fig. 4.3; it developed in a gradual manner, suggesting that the structure was also changing gradually as the temperature was increased. There appears to be no explanation of this effect in terms of domain formation or re-orientation without a change in crystal structure. We assume that at low temperatures $PrAlO_3$ has D_{4h} symmetry, as these experiments could detect no deviation from a tetragonal structure.

In the triclinic phase, where the temperature, T , is in the range ($\sim 99 < T < T_2$) substantial shifts occurred in the electronic lines (Fig. 4.2) which corresponded to changes in the electronic energy levels observed in fluorescence (section 4.3); near T_2 the E_g(el) modes broadened and became undetectable. In this region two lines whose intensities increased with temperature appeared just above the E_g phonon modes at $149cm^{-1}$ and $494cm^{-1}$ (See Fig. 4.2 and 4.3).

In the orthorhombic phase ($T_2 < T < T_1$) there was little temperature variation of the spectra and no electronic lines could be detected. The A_{1g} phonon lay about $8cm^{-1}$ higher than in the trigonal phase (Fig. 4.2) and all the E_g phonons of the trigonal phase were split into two components. The two higher frequencies E_g modes had splittings of about $10cm^{-1}$ and the two components of the lower E_g mode occurred at about $45cm^{-1}$ and $81cm^{-1}$ just below T_1.

In the vicinity of T_2 the components of the lowest

Fig. 4.3.



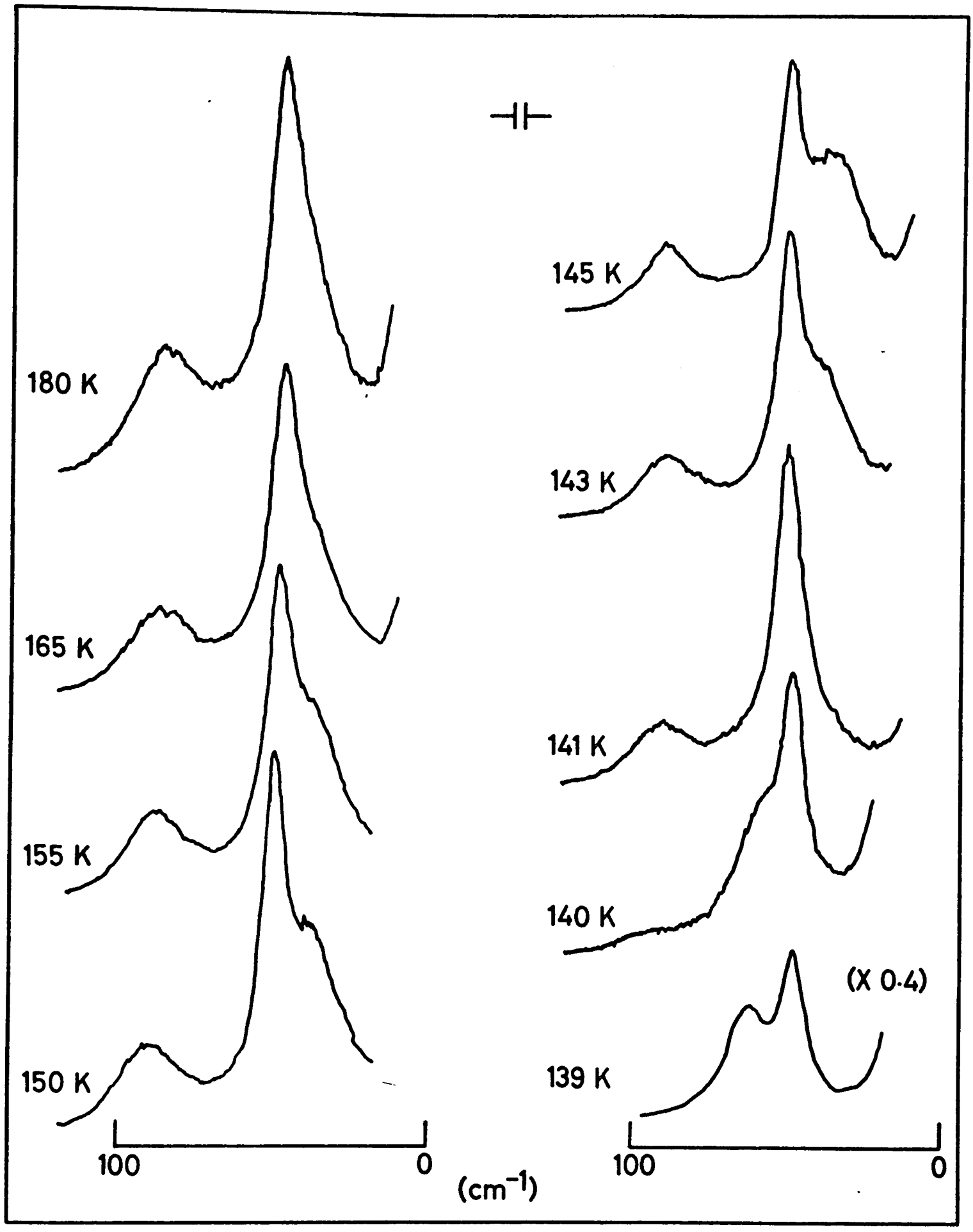
Raman spectra of $PrAlO_3$ E_g symmetry phonon lines at $39cm^{-1}$ and $494cm^{-1}$ between 85^oK and 116^oK showing the splittings which develop. Resolution is indicated at the top of the figure.

E_g phonon mode showed anomalous behaviour (see Figs. 4.2 and 4.4). These effects were studied in detail in an almost single domain crystal, and are discussed at the end of this section.

The cubic perovskite lattice has no Raman-active zone-centre phonons, as all the atoms are at centres of inversion, but the distorted phases possess Raman active phonons which originate from the R-point phonons of the cubic phase because the size of the Brillouin zone is halved in the distorted phases. Symmetries for the even parity phonons in the trigonal and tetragonal modifications of $PrAlO_3$ are given in Table 4.1, assuming that the lowering of symmetry is due to rotations of the oxygen octahedra in the Γ_{25} R-point mode, (see section 4.5). Similar assignments have been given by Worlock et al (1969) for $SrTiO_3$.

In the C_{2h}^3 and C_i^1 symmetry modifications of $PrAlO_3$ all the even parity, zone centre phonon modes are Raman active and singly degenerate. The soft Γ_{25} R-point phonon which drives the O_h^1 to D_{3d}^6 phase transition at 1320°K corresponds to a rotation of T_{1g} symmetry of the oxygen cage about an Al^{3+} ion, (Cochran and Zia 1968), with an opposite sense of rotation in adjacent unit cells of the cubic structure, and it gives rise to one A_{1g} and one E_g Raman active mode in the D_{3d}^6 phase: these were observed at 222cm^{-1} and 45cm^{-1} respectively at 212°K (see Fig. 4.2 and Scott 1969). The other two modes observed in the D_{3d}^6 phase at 164cm^{-1} and 506cm^{-1} at 212°K both had E_g symmetry and also had E_g symmetry

Fig. 4.4.



Low frequency Raman spectra of $PrAlO_3$ between 139°K and 180°K in the vicinity of T_2.

Table 4. 1.

Even parity zone-centre phonon modes in $PrAlO_3$ in the D_{3d}^6 and D_{4h} phases.

Approximate Eigenvector	R-Point progenitor	D_{3d}^6	D_{4h}
Rotation of Oxygen Cage	Γ_{25}(soft)	A_{1g}+ E_g	A_{1g} + E_g
Vibration of Oxygen Cage	Γ'_2	$[A_{2g}]$	$[A_{2g}]$
	Γ'_{12}	E_g	$[A_{2g}]$+ B_{2g}
	Γ_{15}	$[A_{2g}]$+E_g	B_{1g} + E_g
Motion of Pr ion.	Γ_{15}	$[A_{2g}]$+ E_g	B_{1g} + E_g

[ ] denotes a Raman inactive mode

when the crystal was cooled to the apparently tetragonal phase (see Fig. 4.2). Thus it seemed probable that both these modes originated from Γ_{15} R-point phonons of the cubic phase (see Table 4.1), the 164cm^{-1} mode being mainly a motion of the Pr^{3+} ion and the 506cm^{-1} mode mainly an oxygen cage vibration. The third component of each Γ_{15} R-point phonon of the cubic phase had A_{2g} symmetry in the trigonal phase and is Raman inactive, but in D_{4h} it has B_{1g} symmetry and should therefore be Raman active. No phonon modes of B_{1g} symmetry were observed at helium temperatures but just below the temperature at which the E_g modes began to split, weak modes which increased in intensity with temperature were observed about 10cm^{-1} above each of the 506cm^{-1} and 164cm^{-1} phonons (see Figs. 4.2 and 4.3). These modes could be followed through the C_i^1 and C_{2h}^3 phases, but were absent in the D_{3d}^6 phase above T_1 (Fig 4.2). It seemed reasonable to assign these as the third components of the Γ_{15} R-point modes, which were unobservably weak at helium temperature. On this basis the modes originating from the Γ'_{12} R-point phonon (see Table 4.1) were not observed in any of the phases.

Several crystals were examined between crossed polaroids at 77^{o}K. Eventually, a crystal was found which appeared uniformly dark over its whole cross-section as the two crossed polarizers were rotated together through 360^o relative to the crystal. Assuming the crystal was tetragonal, and hence uniaxial with the optic axis parallel to the z (tetragonal) axis, this implied that the polarized light was propagating along

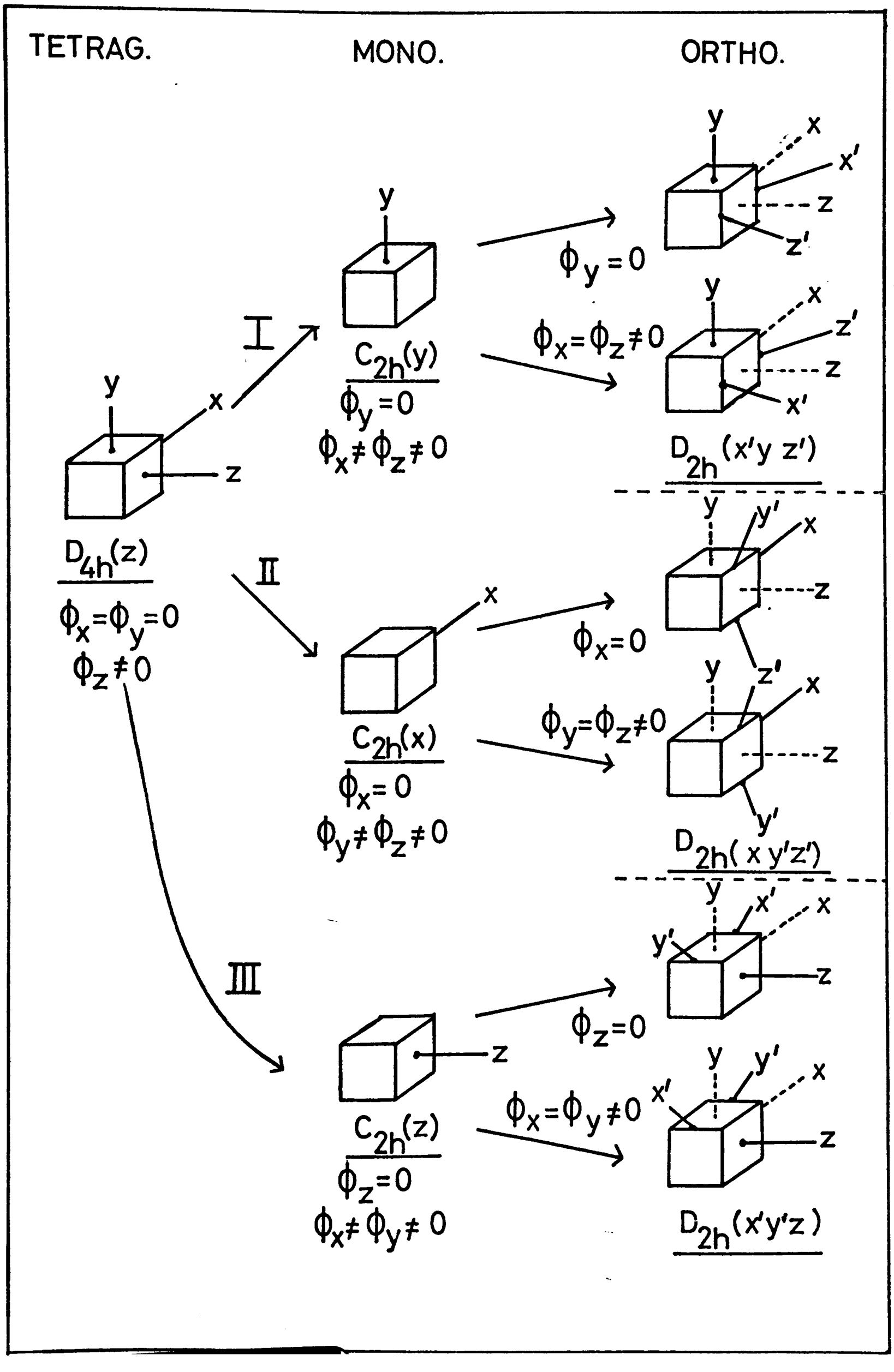
the z axis. The uniformity over the whole crystal showed that the crystal was a single domain. The remainder of the experiments on $PrAlO_3$ were performed on a small, single domain crystal.

In order to check that the direction of the z axis had been correctly determined, the Raman spectra were observed while the crystal was maintained at 77°K. Examination of the polarizations in which the two E_g electronic modes (see Figs. 4.1 and 4.2) appeared proved that the z axis had been correctly assigned.

Having obtained a single domain sample, and found its axes at low temperatures, the first experiments were concerned with studying the way these axes changed in the various phases. The predictions of the model (section 4.5) are shown schematically in Fig. 4.5. On this model the various phases are characterized by rotations, ϕ, of the oxygen octahedral cage about the fourfold axes of the high temperature (O_h) phase. At low temperature, when the model predicts a tetragonal structure, only the rotation about the z, tetragonal, axis is non-zero. As the temperature is raised, the rotation about one of the other axes increases from zero, giving a monoclinic (C_{2h}) phase. This rotation can be about the x axis (Case I) or the y axis (Case II). (see Fig. 4.5) (Case III is discussed below). The two-fold axis is the one about which the rotation is zero (i.e. y in Case I, x in Case II). When this rotation about x and y equals that about z, the crystal has reached the orthorhombic (D_{2h}) phase. For each case I and II there are

Fig. 4.5.

Development of principal axes in $PrAlO_3$ relative to crystal faces, as predicted by model (section 4.5).



two possible sets of axes in the orthorhombic phase, depending on the relative phases of the rotations about the two axes (Fig. 4.5). However, the end result is that in the D_{2h} phase, one two-fold axis is parallel to the (100) type perovskite axis, while the others point in (110) type directions, i.e. at 45^{o} to the original tetragonal set of axes.

In Case III, which is theoretically possible, the rotation about the tetragonal axis goes to zero, while rotations about the other two axes develop. This leads to the sets of axes shown in Fig. 4.5 (Case III).

The polarizations of several lines were studied experimentally in the orthorhombic phase. By arranging for the polarization of the incident and scattered light to be at 45^{o} to the original tetragonal set of axes, a set of axes could be found which were in agreement with the predictions of the model. The lines had polarizations which were consistent with orthorhombic symmetry, one of the two-fold axes being parallel to a (100) type direction of the cubic perovskite lattice and the other two at 45^{o} to the original tetragonal (z) axis, (as shown for Cases I and II in Fig. 4.5).

The Orthorhombic axes often appeared in different directions (in the same sample) after cooling to $77^{o}K$ and warming again to above T_2. However, if the axes were determined above T_2, and the sample only cooled to $99^{o} < T < T_2$, on reheating to above T_2 the <u>same</u> axes were observed. On no occasion was the situation shown as Case III in Fig. 4.5

observed. This involved a spontaneous re-orientation of axes, and would have resulted in a two-fold-axis of the orthorhombic structure being parallel to the fourfold-axis of the tetragonal structure.

The next experiments determined the polarizations of the lines in the Raman spectrum at 118°K, above the temperature at which the degenerate E_g modes were observed to split and below T_2. The fact that the lines showed any kind of polarization indicated that the symmetry was higher than triclinic. (X-ray work by Burbank, 1970 suggested that $PrAlO_3$ had triclinic, C_i^1, symmetry at 135°K.) There is only one kind of Raman tensor for triclinic symmetry, the general symmetric tensor with all elements non-zero. The Raman lines had polarizations at 118°K that were consistent with the monoclinic (C_{2h}) symmetry predicted by the model (Section 4.5).

The method used was as follows:- The sample was heated to above T_2 and the (100) type two-fold orthorhombic axis found. On cooling to 118°K this axis became the two-fold axis of the C_{2h} phase. For this experiment, this was the y axis of the tetragonal structure (see Case I, Fig. 4.5). The Raman tensors for C_{2h} (where y is the two-fold axis) are given in Table 4.2(a), (from Loudon 1964). The symmetries of the Raman lines 118°K are given in Table 4.2(b).

Of particular interest was the line at $\sim 145 cm^{-1}$, derived from an E_g phonon at low temperature. While the other two E_g phonons at $39 cm^{-1}$ and $494 cm^{-1}$ were seen to split

Table 4. 2.

(a) Raman tensor for C_{2h}. The two-fold axis is y.

A_g

$$\begin{pmatrix} a & . & d \\ . & b & . \\ d & . & c \end{pmatrix}$$

B_g

$$\begin{pmatrix} . & e & . \\ e & . & f \\ . & f & . \end{pmatrix}$$

(b) Symmetries of Raman lines at 118°K

Frequency (cm^{-1})	Symmetry	Frequency(cm^{-1})	Symmetry
37	B_g	231	A_g
52	A_g	∿320) ∿400)	?
127	B_g	486	A_g
143.5)	B_g	494	B_g
146.5)	A_g		
162	A_g	504	A_g

(c) Decomposition of irreducible representations of D_{4h} (fourfold axis z) into C_{2h}.

D_{4h}	C_{2h}		
4x axis	2x axis		
z	x	y	z
A_{1g}	A_g	A_g	A_g
A_{2g}	B_g	B_g	A_g
B_{1g}	A_g	A_g	A_g
B_{2g}	B_g	B_g	A_g
E_g	A_g+B_g	A_g+B_g	$2B_g$

at 99°K, no such splitting was observed for the 150cm^{-1} E_g phonon in the multi-domain sample (Fig. 4.2). In the single domain sample, this line appeared with almost equal intensity in zx and zy polarizations (corresponding to an A_g and B_g mode respectively, Table 4.2(a).,) but with peak frequencies differing by 3cm^{-1}. This showed that the E_g phonon had split, and accounted for the absence of splitting in the multi-domain sample. In the multi-domain sample, the zx and zy polarizations were superimposed. As the difference in frequency was comparable to the resolution (~3cm^{-1}), the splitting of the E_g phonon could not be resolved in this case.

The two electronic modes (E_g at low temperature), were very weak at 118°K and their polarizations could not be determined unambiguously. They should have split into an A_g and B_g component in C_{2h} symmetry, but their low intensity and large line-width made it impossible to check this experimentally.

Table 4.2(c) gives the decomposition of the irreducible representations of D_{4h} (where z is the fourfold axis) into the irreducible representations for C_{2h} with the two-fold axis along either x, y or z. It can be seen that the mode symmetries determined at low temperatures assuming a structure of D_{4h} symmetry (given in Fig. 4.2) are consistent with those obtained at 118°K for C_{2h} symmetry (Table 4.2(b).)

Next, the anomaly in the low-lying Raman lines in the region of 150°K was studied. This has already been mentioned

for the multi-domain sample, and is shown in Figs. 4.2 and 4.4. For the single domain crystal the orthorhombic axes were determined at 160°K, and are shown in Table 4.3(a). At low temperatures the set of axes (x,y and z) were perpendicular to the crystal faces, with z being the tetragonal axis. In the orthorhombic phase, the two-fold axes lay along y, and x' and z', where x' and z' are axes rotated by 45°. about y from their original positions x and z (this is just Case I of Fig. 4.5).

Between about 145°K and 190°K the lowest three lines of the Raman spectra consisted of a sharp line (width 8cm^{-1}) and two broad lines (widths ~20cm^{-1}). As the temperature was varied the sharp line remained almost constant in frequency while the two broad lines moved rapidly, particularly in the region of T_2, Fig 4.6. It was found that these lines had different polarizations. The experimentally determined Raman tensors for the sharp line and two broadlines in the orthorhombic phase are given in Table 4.3(b), referred to the set of axes (x,y and z). Traces of the spectra at 159°K in zx and zy polarizations are given in Fig. 4.7.

The Phonon Raman tensors for the irreducible representations of D_{2h} are given in Table 4.3(a), column 2., referred to the two-fold axes (x',y,z') (from Loudon 1964). For electronic excitations, these tensors can be asymmetric, and are given in column 3. Experimentally, it was more convenient to work with the set of axes (x,y,z) and these tensors have been transformed to this set of axes (by rotation

Fig. 4.6.

Low frequency Raman lines in single domain $PrAlO_3$. Circles denote zx polarization; crosses denote zy polarization. Dashed line gives frequency of singlet-singlet electronic transition, from fluorescence.

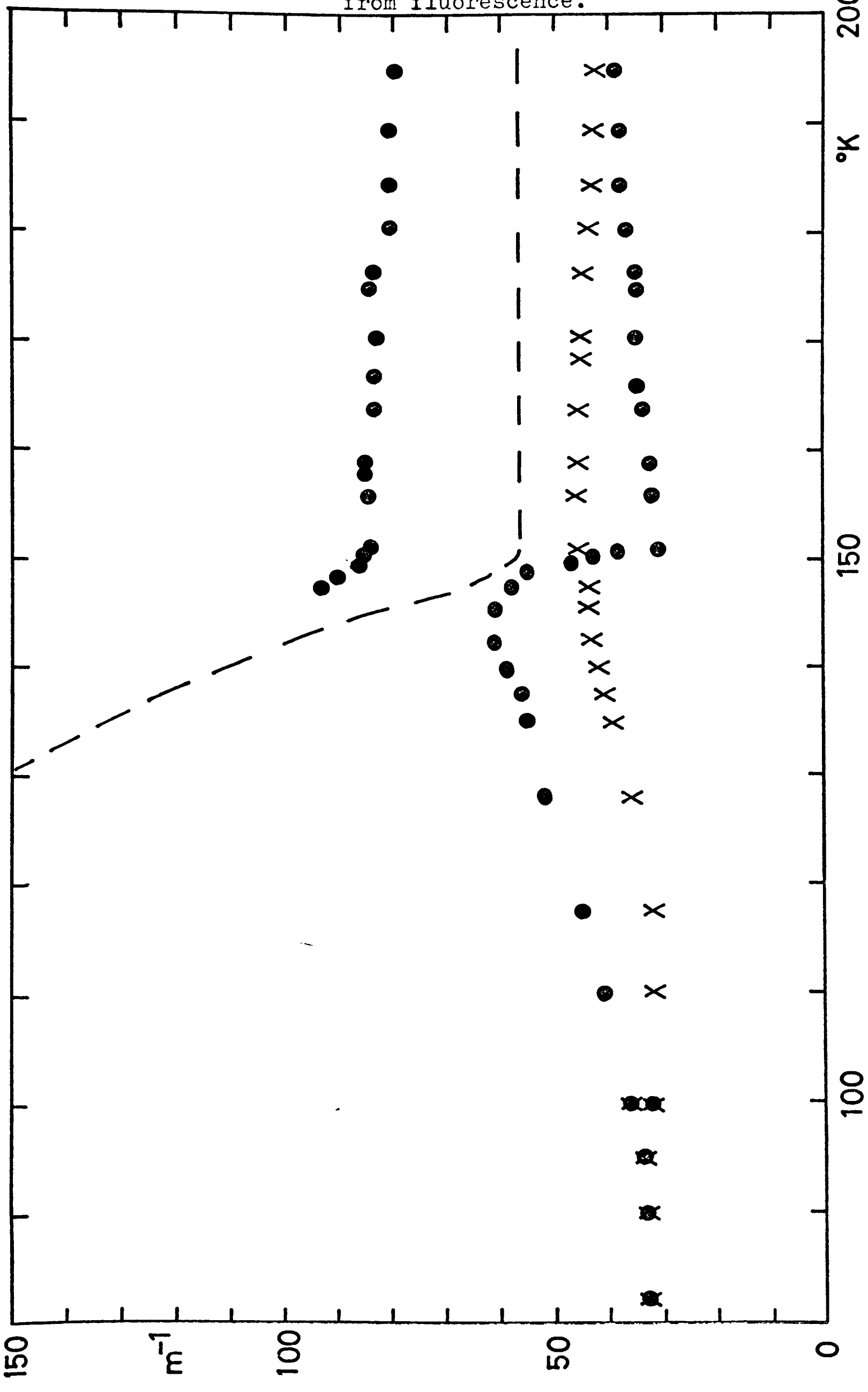
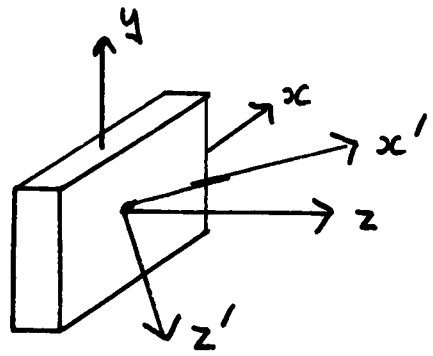


Table 4. 3.



(a) Raman Tensors for D_{2h}.

Irred. Rep.	Axes			
	x′, y, z′.		x, y, z.	
	Phonon	Electronic	Phonon	Electronic
A_{1g}	$\begin{pmatrix} a & . & . \\ . & b & . \\ . & . & c \end{pmatrix}$	$\begin{pmatrix} a & . & . \\ . & b & . \\ . & . & c \end{pmatrix}$	$\begin{pmatrix} a+c & . & c-a \\ . & 2b & . \\ c-a & . & a+c \end{pmatrix}$	$\begin{pmatrix} a+c & . & c-a \\ . & 2b & . \\ c-a & . & a+c \end{pmatrix}$
B_{1g}	$\begin{pmatrix} . & d & . \\ d & . & . \\ . & . & . \end{pmatrix}$	$\begin{pmatrix} . & d-d' & . \\ d+d' & . & . \\ . & . & . \end{pmatrix}$	$\begin{pmatrix} . & d & . \\ d & . & -d \\ . & -d & . \end{pmatrix}$	$\begin{pmatrix} . & d-d' & . \\ d+d' & . & -(d+d') \\ . & -(d-d') & . \end{pmatrix}$
B_{2g}	$\begin{pmatrix} . & . & e \\ . & . & . \\ e & . & . \end{pmatrix}$	$\begin{pmatrix} . & . & e-e' \\ . & . & . \\ e+e' & . & . \end{pmatrix}$	$\begin{pmatrix} e & . & . \\ . & . & . \\ . & . & -e \end{pmatrix}$	$\begin{pmatrix} e & . & -e' \\ . & . & . \\ e' & . & -e \end{pmatrix}$
B_{3g}	$\begin{pmatrix} . & . & . \\ . & . & f \\ . & f & . \end{pmatrix}$	$\begin{pmatrix} . & . & . \\ . & . & f-f' \\ . & f+f' & . \end{pmatrix}$	$\begin{pmatrix} . & f & . \\ f & . & f \\ . & f & . \end{pmatrix}$	$\begin{pmatrix} . & f+f' & . \\ f-f' & . & f-f' \\ . & f+f' & . \end{pmatrix}$

(Factors of $2^{-\frac{1}{2}}$ in the transformations have been neglected)

(b) Experimentally determined Raman tensors for $T_2 < T < T_1$.

X and Y denote non-zero elements.

Broad lines

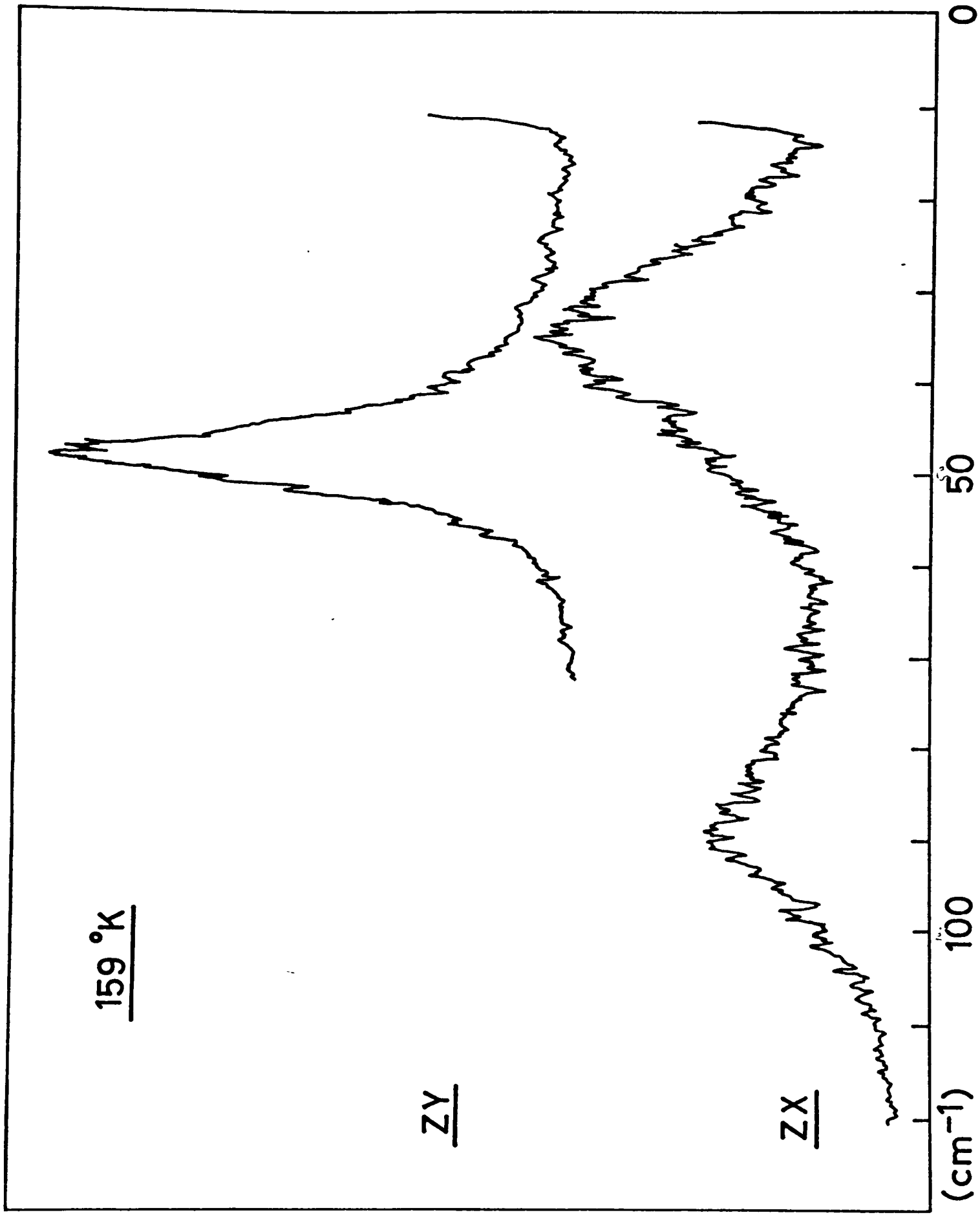
$$\begin{pmatrix} X & 0 & X \\ 0 & 0 & 0 \\ X & 0 & X \end{pmatrix}$$

Sharp line

$$\begin{pmatrix} 0 & Y & 0 \\ Y & 0 & Y \\ 0 & Y & 0 \end{pmatrix}$$

Fig. 4.7.

Low frequency Raman lines in single domain $PrAlO_3$ at 159°K; zx and zy polarizations.



of 45° about y) in columns 4 and 5 Table 4.3(a).

Comparison of the experimental Raman tensor (Table 4.3(b). where X denotes a non-zero component), for the two broad lines with the Raman tensors for the (x,y,z) axes shows that the lines are most likely to have B_{2g} (electronic) symmetry. The only other possibility is A_{1g} symmetry (either phonon or electronic), but this would require the component "b" to be very small.

These two broad lines have been interpreted as a pair of coupled electron-phonon modes of B_{2g} symmetry. Superimposed on Fig. 4.6 is the frequency of the singlet electric-dipole transition obtained from fluorescence (section 4.3). The similarity of the temperature variation of this electronic transition and the two broad modes suggests that the latter may have some electronic character. The very rapid decrease in frequency of the broad modes near T_2 implied that they may act as the "soft" mode for the phase transition at T_2, although they never reach zero frequency. This failure of the modes to fall completely to zero frequency at T_2 may be caused by coupling of the electronic levels to the acoustic phonons (Harley et al, 1973(a).)

If these modes are assumed to act as the soft mode for the phase transition, then they cannot have A_{1g} symmetry (because a soft A_{1g} mode does not change the symmetry of the lattice). This reinforces the interpretation of the broad modes as B_{2g} symmetry electron-phonon coupled modes.

The argument so far has assumed the orthohombic phase

to have D_{2h} symmetry, as suggested by the Raman data and the theoretical model (section 4.5). However, if the symmetry is taken as C_{2h} (from X-ray work by Burbank, 1970), then the broad modes still show electronic character and have B_g symmetry.

Turning now to the sharp mode, whose experimentally determined Raman tensor is also given in Table 4.3(b), (where Y denotes a non-zero component), it can be seen that this corresponds to either a B_{1g} or B_{3g} phonon for D_{2h} symmetry, (see Table 4.3(a),) Group theory shows that it must be B_{3g}, as it is derived from an E_g phonon of the trigonal (D_{3d}) phase. On reducing the symmetry from D_{3d} to D_{2h}, an E_g phonon splits into B_{2g} and B_{3g} components. One component is the upper broad line, already identified as B_{2g}, so that the sharp line must be of B_{3g} symmetry (see Figs. 4.2 and 4.6).

Fig. 4.6. shows that the transition temperature T_2 for the single-domain sample was $151\pm2^{o}K$, in comparison with $146\pm5^{o}K$ for the multi-domain sample. This sample dependance probably accounts for the difference in transition temperatures of this work and that of Cohen (1969). The uncertainty of the temperature was less in the single domain sample as there was less local heating due to absorption by imperfections in the crystal.

In the vicinity of $99^{o}K$, the temperature at which the E_g phonons were observed to split, the zero-frequency-shift scattering was investigated to see if it had a maximum intensity in this region. Observation of "critical opalescence" would have given evidence of a structural phase transition at this

temperature. No change in the intensity could be seen. Critical opalescence has been observed in $SrTiO_3$ at the 110°K phase transition (Steigmeier et al 1973), but in this case the increase was only about 600 counts/sec. and the Rayleigh scattering very weak (200 counts/sec. away from the transition). The Rayleigh scattering in $PrAlO_3$ was very much stronger, and would have masked any such effect. No soft mode could be observed near 99°K. As Birgeneau has recently detected deviations from tetragonal symmetry at temperatures below 99°K, (private communication) we concluded that there was no phase transition at 99°K (see section 4.6).

The Raman experiments show that $PrAlO_3$ has a higher approximate symmetry than is given by X-ray measurements. The Raman measurements indicate D_{4h} symmetry at low temperatures, changing to C_{2h}, D_{2h} and D_{3d} as the temperature is raised. No X-ray measurements have been reported at low temperatures, but at 135°K they give C_i symmetry (cf. C_{2h} from Raman measurements), and C_{2h} and D_{3d} in the higher temperature phases (Burbank 1970).

4.3 Optical Fluorescence

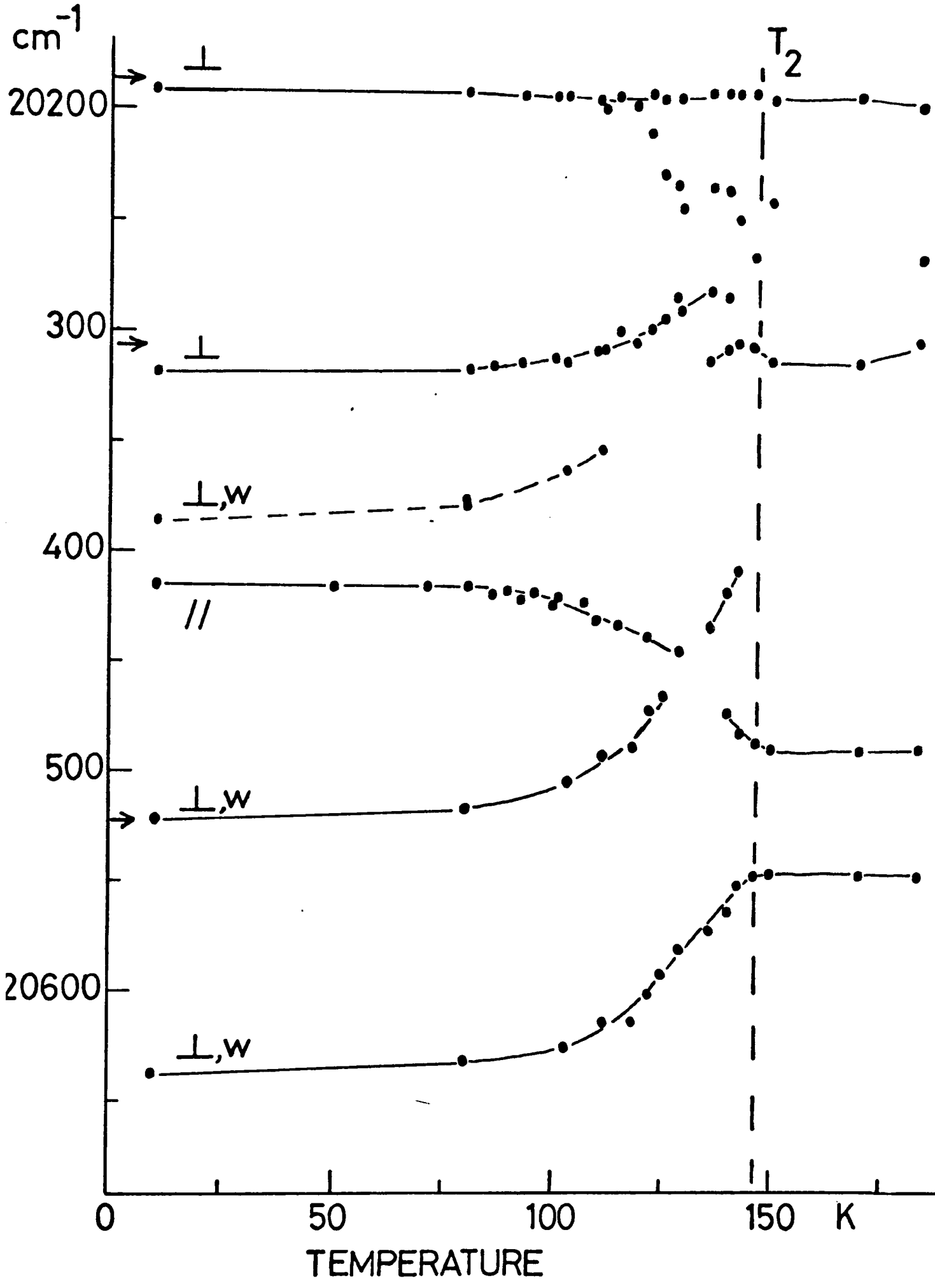
The fluorescence spectrum of $PrAlO_3$ in the region of the $^3P_0 \rightarrow {}^3H_4$ transition of Pr^{3+} was measured as a function of temperature between 4.2°K and 200°K (Harley et al 1973(a).) These spectra were excited by about 10mW of 476.5nm radiation

from an Argon-ion laser, and local heating was found to be negligible. The temperature variation of the line positions is shown in Fig. 4.8 : the full curves indicate the variation in position as far as they could be unambiguously determined. As $^3P_0$ is a singlet, it is assumed that the positions of the lines give a direct measure of the behaviour of the $^3H_4$ ground multiplet levels of Pr^{3+}. These results agree only qualitatively with those of Cohen et al (1969) which were obtained from the more complicated $^3H_4 \rightarrow {}^1D_2$ absorption spectrum.

At 4.2°K the spectra were consistent with the crystal having tetragonal symmetry, being well polarized relative to the tetragonal axis. Six lines were observed; three were weak, (marked w in Fig. 4.8), while the remaining lines were about an order of magnitude more intense. The intense lines were interpreted as being due to allowed electric-dipole transitions whereas the weak lines were electric-dipole-forbidden. Since the upper fluorescence level ($^3P_0$) is a singlet, it follows that the lower levels for the two perpendicular polarized electric-dipole transitions are doublets and for the parallel polarized transition the lower level is a singlet (Fig. 4.8). Assuming tetragonal symmetry, the $^3H_4$ manifold of Pr^{3+} will be split into two doublets and five singlets, and therefore all the weak, electric-dipole-forbidden transitions must be to singlet levels of $^3H_4$.

The arrows on the left of Fig. 4.8 mark the energies of the electronic Raman lines at 4.2°K measured from the

Fig. 4.8.



Positions of fluorescence lines for ^3P_o $^3H_4$ transitions of $PrAlO_3$ as a function of temperature. Below 99^oK lines are polarized parallel (//) or perpendicular ($\perp$) to the tetragonal axis. Arrows show separation of frequencies of electronic Raman lines from ground state. w denotes weak line.

position of the highest frequency fluorescence line, which is presumably due to a transition to the ground level of the $^3H_4$ manifold. Three electronic Raman lines were observed, the two higher frequency ones having E_g symmetry and the lower one B_{2g}, in agreement with the degeneracies of the levels deduced from the fluorescence data. The Raman and fluorescence frequencies agree within the experimental uncertainties caused by the linewidths. (Exact agreement would not be expected anyway in a system with such a strong effective interaction as there is between Pr^{3+} ions). At helium temperatures the fluorescence lines were very broad ($\sim 10cm^{-1}$) compared with other Rare Earth ions.

The fluorescence spectrum changed very little with temperature up to about 100°K. Between 100 and 150°K the line positions changed rapidly, the lines broadened and became unpolarized. This line broadening and self-absorption made the intense lines difficult to follow above 100°K, but it appeared that at this temperature the two intense perpendicularly polarized lines split, consistent with their being transitions to doublet levels. Above T_2 the lines became roughly constant in frequency. The highest frequency transition (at $20550cm^{-1}$) was very close to the value $20556cm^{-1}$ given by Martin-Brunetière (1969) for the transition from $^3P_0$ to the ground level of Pr^{3+} in $LaAlO_3$, which has the trigonal D_{3d}^6 structure of the room temperature phase of $PrAlO_3$.

4.4 EPR Experiments

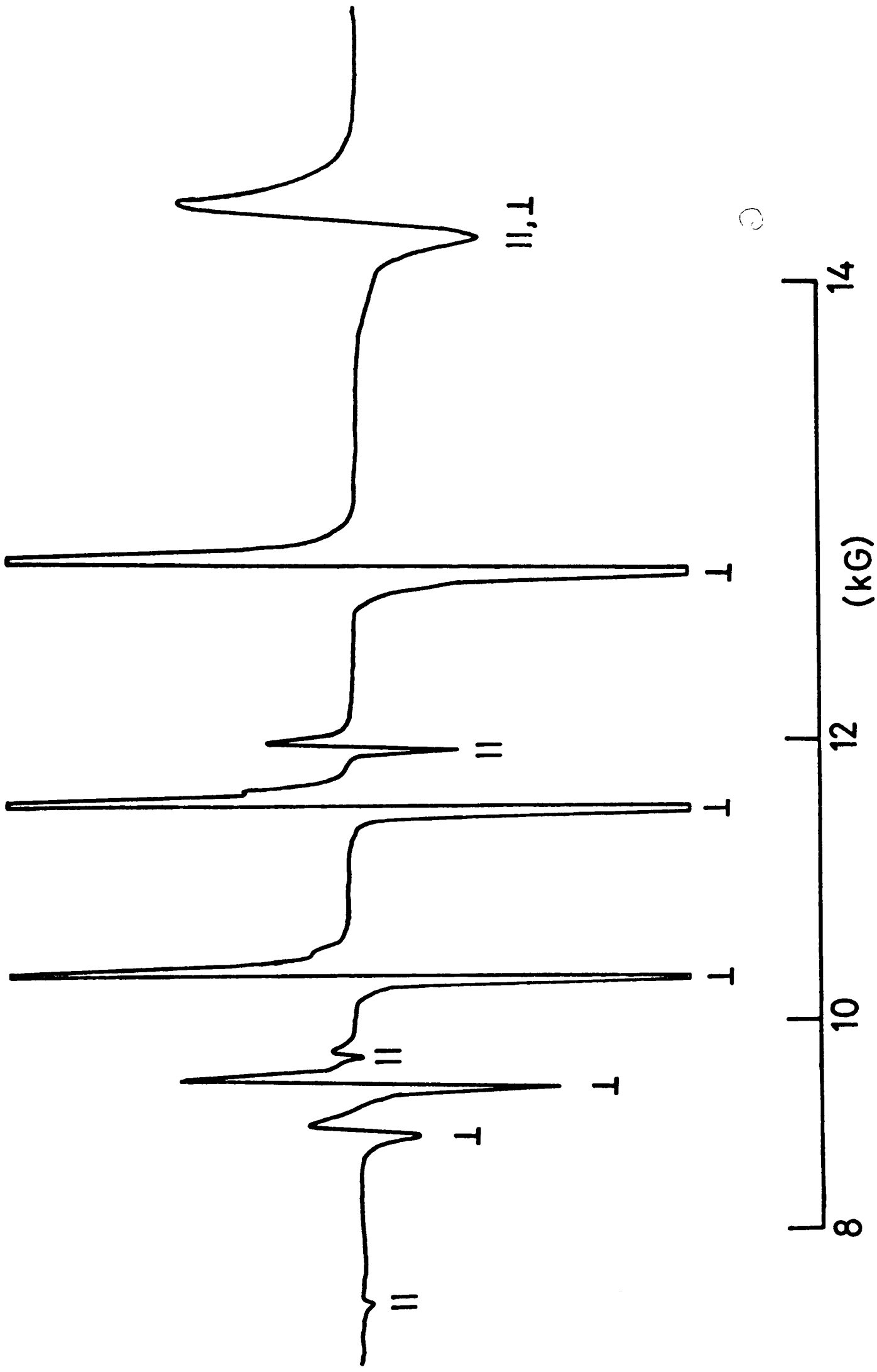
In this section a brief description will be given of the results of some EPR experiments on $PrAlO_3$ by Smith (Harley et al 1973(a).) The experiments were performed on the same large multi-domain crystal used in the Raman experiments; this was found to contain sufficient Gd^{3+} impurity to produce an intense EPR spectrum. Spectra were recorded at Q band (35GHz) and K band (25GHz) using transmission and reflection cavity systems respectively.

The object of this work was to determine the symmetry of the Pr^{3+} site at low temperatures. The Gd^{3+} ion, which substituted for Pr^{3+}, was an excellent probe as its EPR spectrum was very sensitive to the site symmetry. In agreement with the optical experiments, no deviation from tetragonal symmetry could be detected at $77^{o}K$.

At $77^{o}K$, only two types of EPR spectra were found when the magnetic field was aligned along a fourfold axis of the cubic perovskite structure. A "parallel" spectrum was obtained from those domains with $\underline{H}$ parallel to the tetragonal axis (z) and a "perpendicular" spectrum with $\underline{H}$ perpendicular to z. The magnetic field was insufficient to force the sample into a single domain, so the relative intensity of the two types of spectra depended upon the domain distribution.

A typical recording at Q band is reproduced in Fig.4.9, showing both kinds of spectrum when $\underline{H}$ was along a $\langle 100 \rangle$ type axis. The fact that only one type of perpendicular spectrum was seen implied that the two axes perpendicular to z were

Fig. 4.9.



Q-band EPR spectrum of Gd^{3+} ions in $PrAlO_3$ at $77^{o}K$. $\underline{H}$ is along a (100) direction of cubic structure. Lines marked ‖ arise from domains where $\underline{H}$ is parallel to the tetragonal z-axis; those marked ⊥ where $\underline{H}$ is perpendicular to the z-axis.

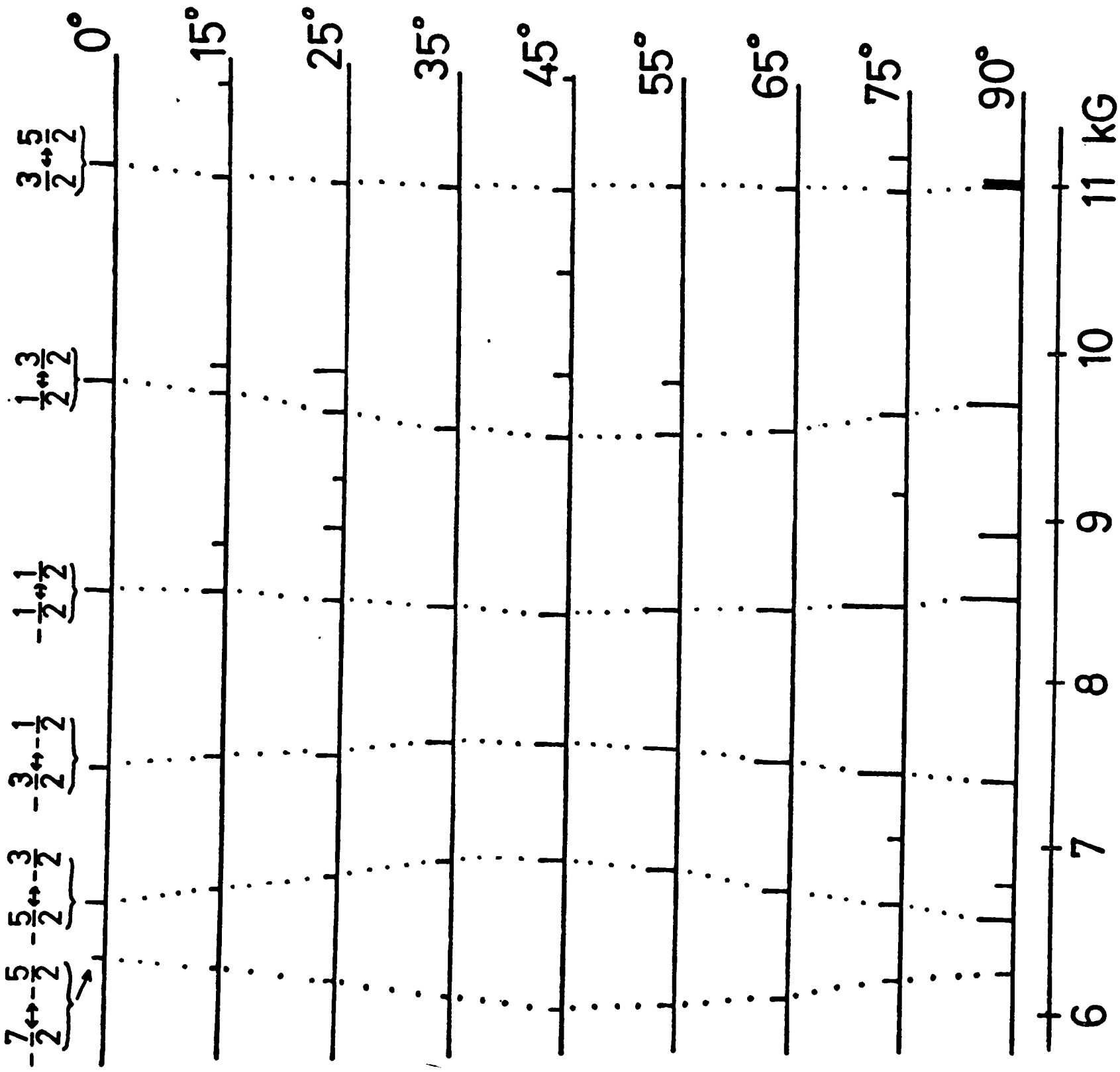
equivalent. This was checked by studying the angular variation of the spectra on a sample that was nearly a single domain whose z axis was vertical and normal to the plane of rotation of the magnetic field. The spectrum has a 90° periodicity, and no lines were observed to split into two components, (see Fig. 4.10). The points joined by dotted lines in this figure are the perpendicular spectrum; the remaining lines are weaker and caused by domains whose z axis was not vertical.

These results showed that at 77°K any deviation of the symmetry of a domain from tetragonal would have to be small enough to produce splittings in the EPR spectrum of less than the linewidth, (i.e. less than 100G). This rather large linewidth seems to be characteristic of the flux-grown crystals; Kiro et al (1963) found that flux-grown samples of $LaAlO_3$ had a considerably larger Gd^{3+} linewidth than those grown by other methods.

4.5 Theory

This section gives a brief description of a theoretical model of $PrAlO_3$ developed by Smith (Harley et al 1973(a).) The model is a molecular field model which includes coupling of the Pr^{3+} ion to the soft Γ_{25} R-point phonon of the high-temperature cubic phase, and is able to account qualitatively for the observed phase transitions.

Fig. 4.10.



Angular variation of K-band EPR spectra of Gd^{3+} in $PrAlO_3$ at 77°K. Dotted curves indicate angular variation of spectrum from domains with H perpendicular to the tetragonal axis, 0° corresponds to a ~100 direction of the cubic perovskite structure. Remaining lines are from other types of domain. Relative intensities are shown by heights of marks.

The various phases are characterized by the rotations of the oxygen-octahedra about the fourfold axes of the cubic phase; the rotations being ϕ_x, ϕ_y and ϕ_z. The rotations in the different phases are:-

$$\begin{aligned}
&\text{Trigonal} - && \phi_x = \phi_y = \phi_z \neq 0 \\
&\text{Orthorhombic} - && \phi_x = \phi_y \neq 0;\ \phi_z = 0 \\
&\text{Monoclinic} - && \phi_x \neq \phi_y \neq 0;\ \phi_z = 0 \\
&\text{Tetragonal} - && \phi_x \neq 0;\ \phi_y = \phi_z = 0
\end{aligned} \qquad (4.1)$$

The potential energy, V, of the perovskite structure can be written in terms of these rotations as

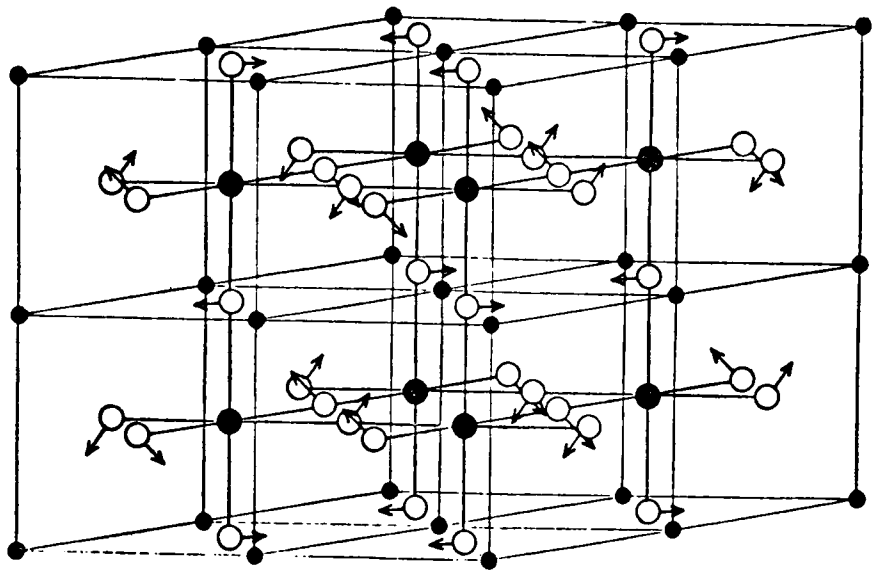
$$V = \tfrac{1}{2}a(\phi_x^2+\phi_y^2+\phi_z^2)+\tfrac{1}{4}b(\phi_x^4+\phi_y^4+\phi_z^4)+\tfrac{1}{2}c(\phi_x^2\phi_y^2+\phi_y^2\phi_z^2+\phi_z^2\phi_x^2) \qquad (4.2)$$

(from Thomas and Müller 1968). The parameters a,b,c are functions of temperature at high temperature, and the instability of the Γ_{25} R-point phonon is represented by allowing a to become negative below temperature T_a. For V to be stable against large rotations, $b > 0$ and $2c > -b$. The perovskite structure will then assume the configuration that minimizes V.

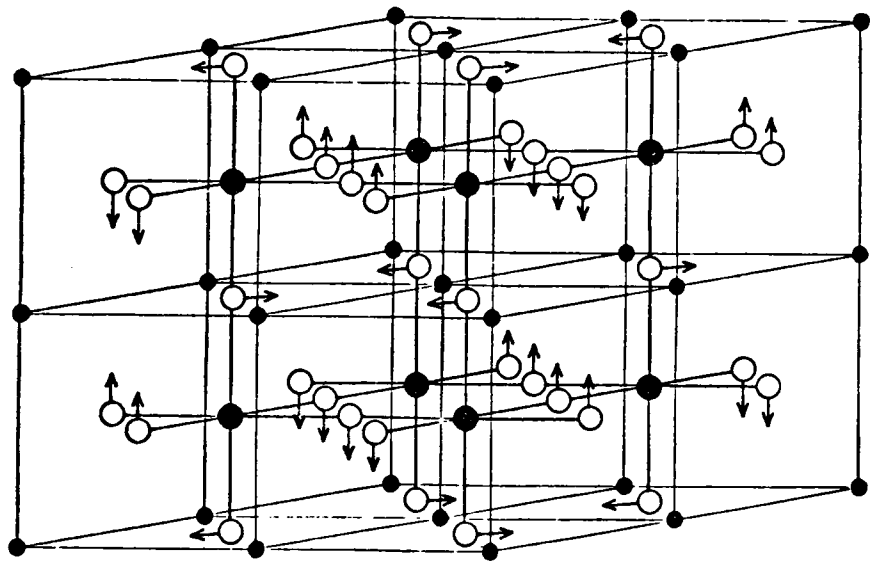
The values of the parameter a, b, c were estimated from the frequencies of the low frequency "soft" phonon modes which arise from the Γ_{25} R-point phonon of the cubic phase (Harley et al 1973(a).) At room temperature these phonon modes are an E_g doublet (frequency $43cm^{-1}$) and an A_{1g} singlet ($212cm^{-1}$),

Fig. 4.11.

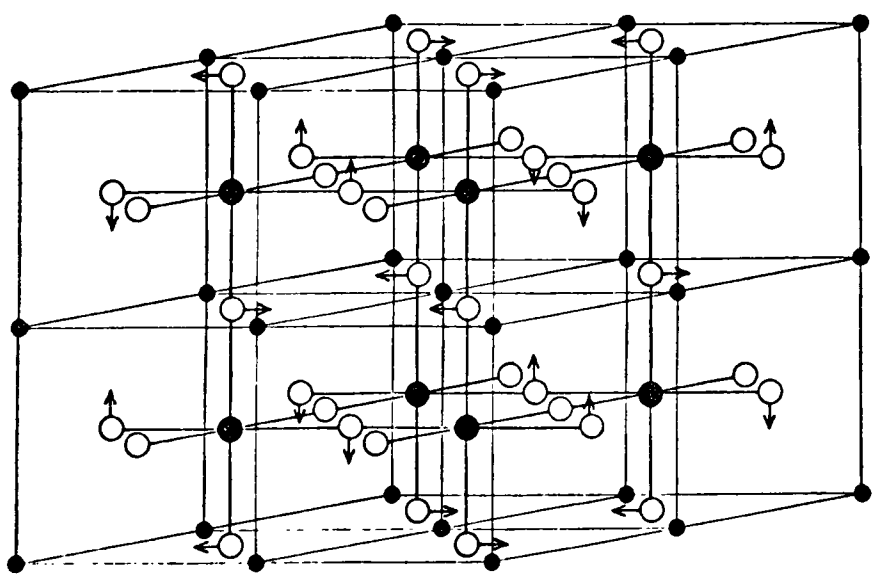
(a) Trigonal (D_{3d})



(b) Orthorhombic



(c) Tetragonal



Displacements of the oxygen ions in $PrAlO_3$ in (a) trigonal, (b) orthorhombic, (c) tetragonal phases • Pr, ● Al, O O.

(section 4.2). These frequencies, together with Burbank's (1970) estimate of the oxygen octahedra rotation angle at room temperature ($7^{o}56'$), gave :-

$$\left.\begin{aligned} a &= -1.66 \times 10^{5} \quad {}^{o}K \\ b &= 9.44 \times 10^{6} \quad {}^{o}K \\ c &= 8.40 \times 10^{6} \quad {}^{o}K \end{aligned}\right\} \qquad (4.3)$$

It was assumed that these values did not vary with temperature below room temperature.

The values of b and c (equation 4.3) are about equal. When b = c, all the four phases have equal energy. Hence in $PrAlO_3$ the phases must have nearly equal energy; it is for this reason that the ion-lattice coupling of Pr^{3+} is able to cause the crystallographic phase changes.

A Hamiltonian, H_{el}, was constructed which included this ion-lattice coupling of the Pr^{3+} electronic levels to the rotations $\emptyset$. For simplicity, only coupling to a distortion of E_g symmetry was taken into account. Only the lowest five electronic levels were considered; these originated from the E_g ground state and T_{2g} level of the high temperature cubic phase. If H_{el} has a set of eigenvalues λ_i , then the partition function for the Pr^{3+} site is

$$Z = \sum_{i} \exp(-\lambda_i / kT) \qquad (4.4)$$

and the Helmholtz free-energy (per Pr^{3+} site)

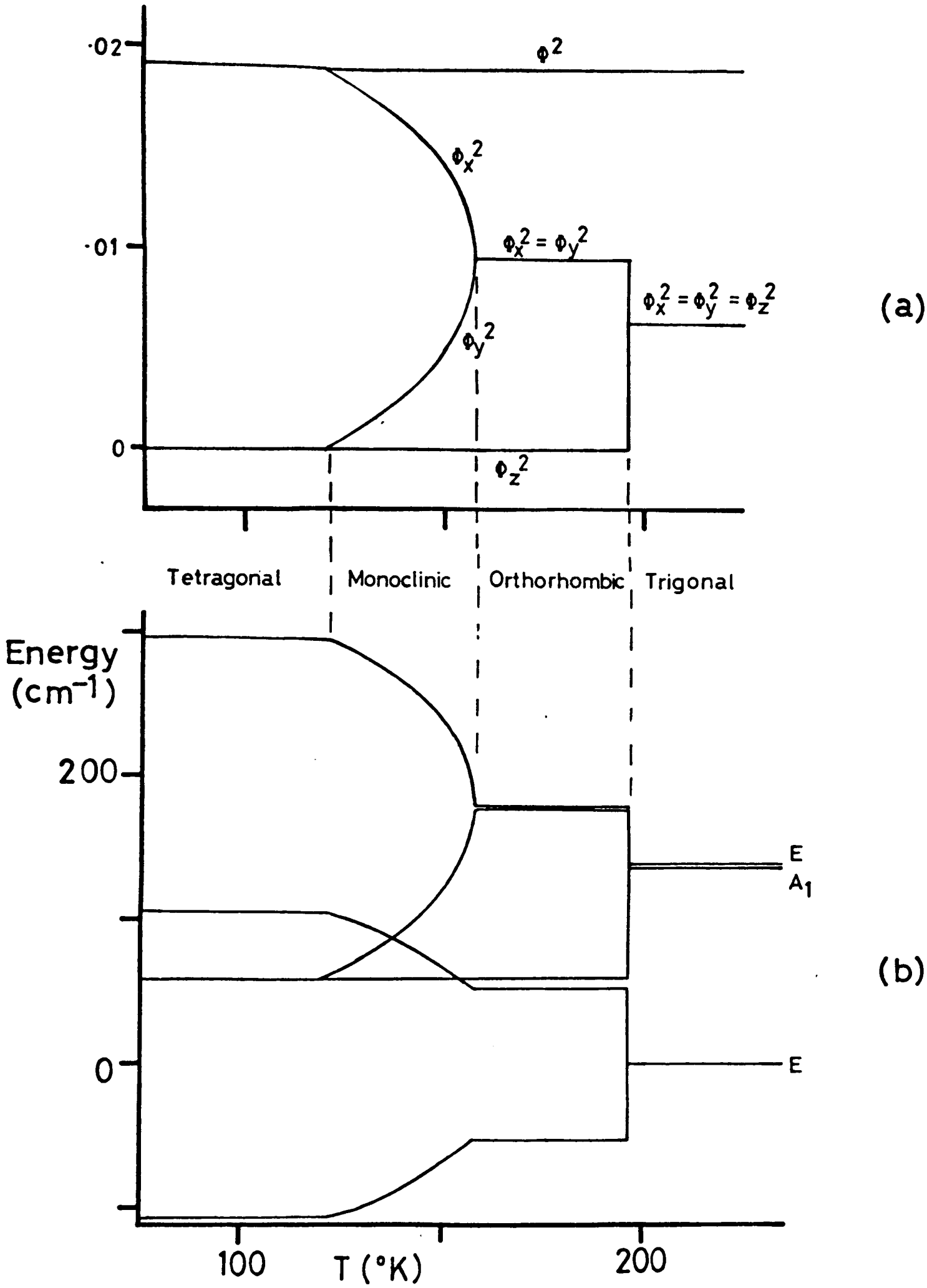
$$F = -kT \ln(z) + V \qquad (4.5)$$

where k is Boltzman's constant and V the potential energy given by equation (4.2). By finding the values of ϕ that minimized F at a given temperature, a molecular field description of the thermodynamic behaviour of the system was obtained.

The model predicted the following sequence of phases as $PrAlO_3$ is warmed from T = 0: Tetragonal, Monoclinic, Orthorhombic, Trigonal. Fig. 4.12a shows the squares of the equilibrium values of the rotations as a function of temperature for certain values of the ion-lattice coupling coefficients (Harley et al 1973(a).) There is a discontinuous (first-order) change from the trigonal phase ($\phi_x = \phi_y = \phi_z$) to an orthorhombic phase ($\phi_x = \phi_y = 0$; $\phi_z = 0$) at $T_1 = 196^{\circ}K$, and at $T_2 = 158^{\circ}K$ a mon clinic phase is obtained where ϕ_z remains zero, but ϕ_x and ϕ_y are no longer equal. As T decreases below T_2 ϕ_y falls and ϕ_x increases, the total rotation staying approximately constant, until ϕ_y becomes zero at $T_3 = 121^{\circ}K$, below which temperature a tetragonal phase ($\phi_y = \phi_z = 0$) occurs. In Fig. 4.12b the behaviour of the lowest five levels of Pr^{3+} is shown, as predicted by the model. It can be seen that the only significant variation of the energy levels occurs between T_2 and T_3 in the monoclinic phase. Note that while the model predicts a transition to a tetragonal phase, no such transition was observed experimentally (see section 4.6.)

The lower two phase transitions are second-order, whilst the transition at T_1 is first-order. These results are in accordance with the group theoretical properties of the

Fig. 4.12.



(a) Squares of equilibrium rotations of the AlO_6 octahedra about the three cubic axes of $PrAlO_3$ according to the model of Section 4.

(b) Corresponding temperature variations of the lowest five energy levels of Pr^{3+} showing their behaviour in the various phases.

model for the following reason. The group of the orthorhombic structure is not a subgroup of that of the trigonal structure, and so the trigonal to orthorhombic phase transition must be of first-order, on the other hand the group of the monoclinic structure is a subgroup of the groups of both the tetragonal and orthorhombic structure, and so the corresponding phase transitions will be of second-order.

4.6 Conclusions

The theoretical model of $PrAlO_3$ described in section 4.5 gives a qualitative description of the behaviour of this material. It predicts the existence of different phases, and the fact that the only significant changes occur at the first-order transition temperature T_1 and in the region $99^{o}K < T < T_2$.

Comparing the actual variation of the electronic energy levels as predicted by the model (Fig. 4.12b) with those measured by experiment (Figs. 4.8 and 4.2), it is seen that the behaviour of the E_g levels is well accounted for, but the order of the levels of the T_{2g} state appear to be inverted. The agreement with experiment is therefore only qualitative. The comparison could perhaps be improved by including more terms in H_{el} (section 4.5), and by including the remaining energy levels of the Pr^{3+} ion, but the data was not sufficient to enable a full crystal-field fit to be accomplished. In any

case it is unlikely that a molecular field treatment of this type is capable of better than a qualitative description of the temperature variation of the system because of the type of approximation inherent in using a phenomenological potential energy V as in equation (4.2). This has ignored the movements of the Pr^{3+} ions in the low temperature phases from their positions in the high temperature cubic phase, which were observed by X-ray methods (Burbank 1970). The model has also neglected coupling of the electronic levels to strains in the crystal.

At low temperatures, below about $99^{o}K$, the Raman, optical fluorescence and EPR measurements all indicate that $PrAlO_3$ has tetragonal symmetry, which was assumed to be D_{4h}. The main evidence for this came from the Raman experiments, which showed a splitting developing in some of the phonon lines at $99^{o}K$ as the temperature was increased (Fig. 4.3), indicating that at lower temperatures the modes were degenerate and hence that the crystal had a fourfold rotation axis. No other evidence of a phase transition at $99^{o}K$, such as a soft mode, could be found. Recent EPR and neutron scattering experiments by Birgeneau et al (private communication to W. Hayes), have shown that $PrAlO_3$ has a small distortion from tetragonal symmetry well below $99^{o}K$. Their results showed that the deviation from tetragonal symmetry decreased as the temperature was lowered, and that $PrAlO_3$ tended to become perfectly tetragonal only at $0^{o}K$. They also pointed out that the EPR linewidths of Gd^{3+} in their experiments were considerably less

than 100G (see section 4.4), which explains why their experiments were able to detect a small deviation from tetragonal symmetry whereas ours could not (private communication to S.R.P.Smith).

Presumably this deviation from D_{4h} symmetry is too small to be detected by Raman measurements. Exactly how large a deviation from tetragonal symmetry must be before it produces a noticeable effect on the Raman spectrum is hard to ascertain. A structural analysis at low temperatures ($<99^{o}K$) by X-ray methods would be helpful. No X-ray analysis below $135^{o}K$ has yet been reported. Another experiment of interest would be to study the EPR spectrum at low temperatures of $PrAlO_3$ doped with Fe^{3+}. The Fe^{3+} ion substitutes at the Al^{3+} site, and its spectrum should be very sensitive to the symmetry of the surrounding oxygen atoms.

In the vicinity of T_2, the $151^{o}K$ phase transition, the two low-lying broad modes in the Raman spectrum were identified as coupled electron-phonon modes of B_{2g} symmetry, (see section 4.2). These are thought to act as the soft mode for the transition, but fail to reach zero frequency due to coupling to acoustic phonons (Harley et al 1973(a).) Birgeneau (private communication to be published, Phys. Rev. Lett.), has shown that this transition may be treated as a Jahn-Teller phase transition in a similar manner to $DyVO_4$ (Elliott et al 1972). In $DyVO_4$, an electronic mode was seen to partially soften below the transition temperature, but did not go to zero frequency, due to coupling to an acoustic phonon. However, the

coupling caused the dispersion curve of this acoustic phonon to have zero slope at the zone centre at the transition temperature, thereby producing an anomaly in one of the elastic constants. Using neutron scattering Birgeneau et al confirmed our identification of this electron-phonon coupled mode, and were able to measure the coupling of the electronic level to the optic and acoustic modes separately. They found the total coupling to be quite large ($240cm^{-1}$) with approximately equal contributions from the optic and acoustic phonons. This coupling to the acoustic phonon in $PrAlO_3$ should produce an acoustic anomaly at T_2 which would be detectable by ultrasonic measurements or Brillouin scattering.

CHAPTER FIVE

EXPERIMENTS WITH

TERBIUM GADOLINIUM VANADATE

5.1 Introduction

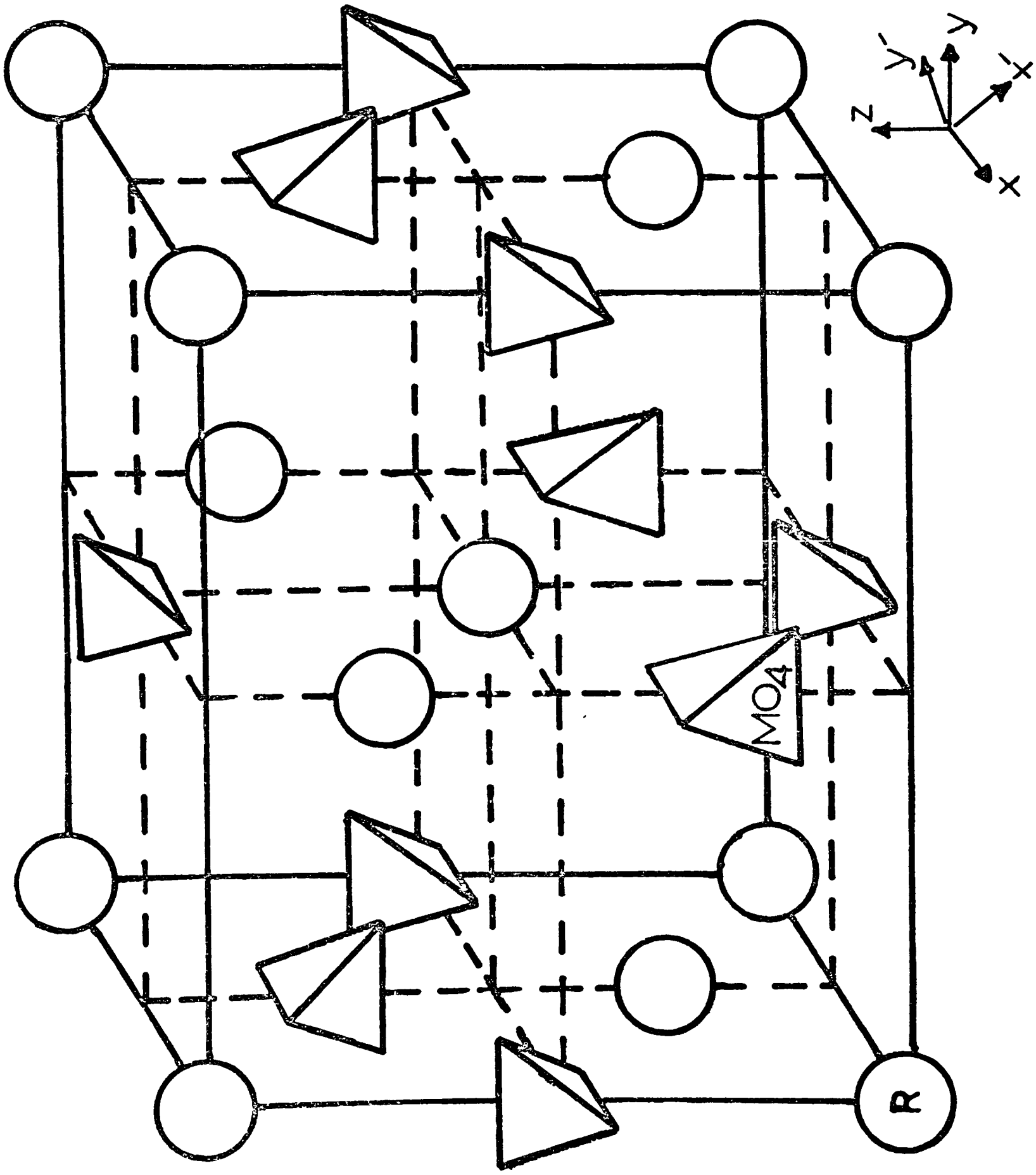
The Jahn-Teller phase transitions in Rare Earth vanadates and arsenates have recently been the subject of a wide range of experimental and theoretical studies (Elliott et al 1972; Sandercock et al 1972). These systems have the advantage that they can be treated in terms of simple theoretical models. In particular, the molecular field approximation (MFA) has been very successful in accounting quantitatively for measurements on $TbVO_4$, (Wells and Worswick 1972), suggesting that the co-operative interaction in this material is of long range.

In pure $TbVO_4$ the co-operative Jahn-Teller effect causes a second-order phase transition at 34^oK which takes the crystal from the tetragonal high temperature structure D_{4h}^{19} to the orthorhombic low temperature structure D_{2h}^{24}. Although there has been no detailed X-ray crystallographic study of the orthorhombic phase, the space group has been determined by optical absorption spectroscopy (Gehring et al 1971; Becker and Laugsch 1971). Below the transition temperature T_D a splitting develops in the ground electronic states of the Tb^{3+} ion, and this acts as the soft mode for the phase transition (Elliott et al 1972). $TbVO_4$ has not been observed to order magnetically above 1^oK. (Cooke et al 1971).

The structure of $TbVO_4$, the zircon structure, is shown in Fig. 5.1. There are two formula units per unit cell. The principal axes x' and y' lie at 45^o to the crystal faces. Above the transition these two axes are equivalent, but become

Fig. 5.1.

Schematic representation of the tetragonal zircon structure (D_{4h}^{19}) for RMO_4 (R = Rare Earth, M = V, As or P.) Two molecules in the unit cell are shown. Note the co-ordinate axes. (Elliott et al 1972).



inequivalent below T_D. At the transition a distortion occurs in a zone centre phonon mode of B_{2g} symmetry. In the tetragonal phase the unit cell contains two equivalent Tb^{3+} sites of D_{2d} symmetry, while below T_D the sites remain equivalent and have D_2 symmetry (Elliott et al 1972).

$GdVO_4$ has the same structure as $TbVO_4$ at high temperatures, but does not show a Jahn-Teller phase transition down to 0.5°K. (Elliott et al 1972; Cashion et al 1970). However, $GdVO_4$ does order anti-ferromagnetically at 2.55°K. (Cashion et al 1970).

$TbVO_4$ has 12 atoms in the unit cell, giving 36 zone-centre phonon branches. It was found to be convenient to separate these phonons into "internal" modes of the tetrahedral VO_4 group, and "external" modes, due to translation and rotation of these groups with respect to the Tb ion (Elliott et al 1972). The symmetries of the $\underline{k} = 0$ phonons for the D_{4h} phase are:-

acoustic modes :		$A_{2u} + E_u$
external modes :	odd	$A_{2u} + B_{1u} + 2E_u$
	even	$A_{2g} + 2B_{1g} + 3E_g$
internal modes :	odd	$A_{1u} + 2A_{2u} + 2B_{2u} + 2E_u$
	even	$2A_{1g} + 2B_{1g} + B_{2g} + 2E_g$

Of the 13 even-parity $\underline{k} = 0$ phonons, all except A_{2g} are Raman active.

Table 5.1 gives the measured frequencies of the Raman active phonons in several Rare Earth zircon structure materials (from Elliott et al 1972). The A_{1g}, B_{1g} and E_g phonons are labelled arbitrarily with Roman numerals. Most of the lines were observed, and it was assumed that the others were either too weak or obscured by nearby intense lines. Some sample-dependant mixing of the B_{1g} and B_{2g} phonons was found; this was later attributed to the finite solid angle of the collection optics (Chaves and Porto 1972).

Fig. 5.2 shows the Raman spectrum of pure $TbVO_4$ in zz and $(zx' + zy')$ polarizations above and below the phase transition. In these polarizations A_{1g} and E_g phonons are seen. The main effect of the transition on the spectra is the splitting of the doubly degenerate E_g phonons; the frequency of the singlet phonons hardly changed, (see also Table 5.1). None of the phonons showed any marked intensity changes at the transition. The B_{2g} phonon showed little change through the transition, even though the phase change was associated with a distortion of this symmetry. No new phonons were seen below T_D, but some electronic lines appeared (one can be seen in Fig. 5.2., marked "e") (Elliott et al 1972). These electronic lines are discussed below.

The E_g phonons split into two components below T_D, which were narrow and symmetric in $TbVO_4$ (Fig. 5.2). The magnitude of the splitting varied among the different E_g phonons (Table 5.1). This splitting occurred in a continuous manner below the transition temperature and smoothly approached a

Table 5. 1.

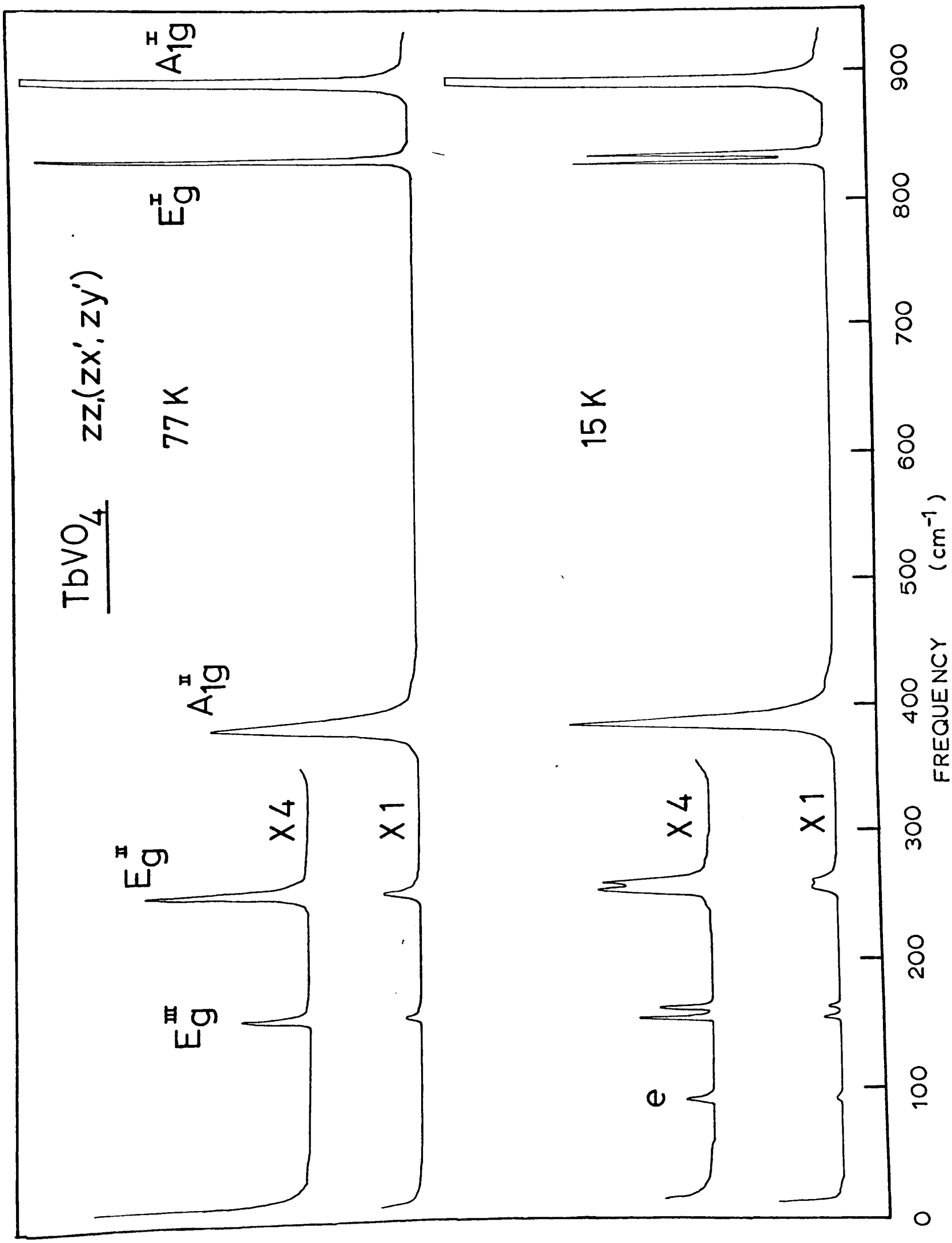
Frequencies (cm^{-1}) of Raman active phonon modes in some zircon structure crystals.

Accuracy $\pm$ 2cm^{-1} (from Elliott et al 1972).

Crystal and Temperature	Internal Modes							External Modes				
	A_{1g}^{I}	E_{g}^{I}	B_{1g}^{I}	B_{1g}^{II}	E_{g}^{IV}	A_{1g}^{II}	B_{2g}	B_{1g}^{IV}	E_{g}^{II}	E_{g}^{III}	B_{1g}^{III}	E_{g}^{V}
YVO_4 300K	891	839	817	490	-	379	260	265	260	164	156	-
77K	894	842	819	490	-	382	260	270	264	163	157	-
4.5K	895	843	819	490	-	383	261	270	264	163	157	-
$GdVO_4$ 300K	884	825	809	483	-	380	261	-	246	156	123	-
77K	886	827	811	482	-	381	260	-	248	155	123	-
10K	886	827	812	483	-	381	260	-	248	154	124	-
$TbVO_4$ 300K	882	824	808	484	-	380	261	-	246	155	121	-
77K	888	829	811	484	-	384	260	-	253	156	122	-
16K	889	826(zy) / 832(zx)	810	484	-	385	260	-	252(zx) / 257(zy)	152(zy) / 160(zx)	122	-
$DyVO_4$ 300K	886	828	812	486	-	381	260	-	249	156	117	-
77K	891	834	814	486	-	382	260	-	249	156	120	-
4.5K	893	829(zy) / 838(zx)	815	487	-	383	260	-	247(zx) / 265(zy)	154(zx) / 156(zy)	120	-
$DyAsO_4$ 300K	890	835	882	500	435	405	235	-	245	159	129	-
77K	894	837	884	501	435	403	235	-	250	161	129	-
4.5K	894	834(zy) / 837(zx)	884	504	435	404	234	-	243(zx) / 259(zy)	160(zx) / 163(zy)	129	-
$DyPO_4$ 300K	997	1017	1053	653	576	485	330	-	294	(184)	140	130
77K	998	1019	1057	655	577	488	330	-	297	(186)	140	132
4.5K	999	1021	1060	656	578	491	328	-	296	-	138	132

Fig. 5.2.

Raman spectra of $TbVO_4$ at 77°K and 15°K for superimposed zz and (zx′ zy′) polarizations. The line marked e is an electronic transition of the Tb^{3+} ions.



limiting value at low temperatures, indicating that the transition was of second order. This property was used to determine the transition temperature. The two components of the split E_g phonons had zx' and zy' polarizations respectively, showing that the principal axes were along x' and y' (see Fig. 5.1) The high frequency component of the E_g^I phonon was arbitrarily assigned to zx' in $TbVO_4$, from which the rest of the labelling of Table 5.1 follows, (Elliott et al 1972).

The components of the E_g phonons below T_D did not appear to have pure zx' or zy' polarization, because of superposition of signals from domains in the crystal with x' and y' axes interchanged. The size of these domains was estimated as at least 100 μm with the longest dimension along the z axis (Elliott et al 1972).

Fig. 5.3 shows the electronic energy level scheme for $Tb^{3+}(f^8, {}^7F_6)$ at 16, 36 and 77°K. Some of the electronic Raman spectra from which it was deduced are shown in Fig. 5.4. In (zx', zy') polarizations at 77°K transitions were seen from the A_1 and B_1 electronic levels to the higher E level with energies 73.5 and 90cm^{-1} respectively, and these transitions could be followed as a function of temperature (Fig. 5.4(a).) Of particular interest was the line which emerged from the wing of the laser line below T_D, and increased in frequency to 55cm^{-1} at 4°K, as this was the soft mode of the transition, Fig. 5.4(b) shows the electronic transition in $(x'x', y'y')$ polarizations from the A_1 to B_1 levels above T_D ($A_1 \rightarrow A_1$ levels

Fig. 5.3.

Electronic energy levels of $TbVO_4$ at 16°K, (below T_D=34°K) and at 36°K and 77°K (above T_D). The energies and polarizations of the observed Raman lines are indicated.

(from Elliott et al 1972).

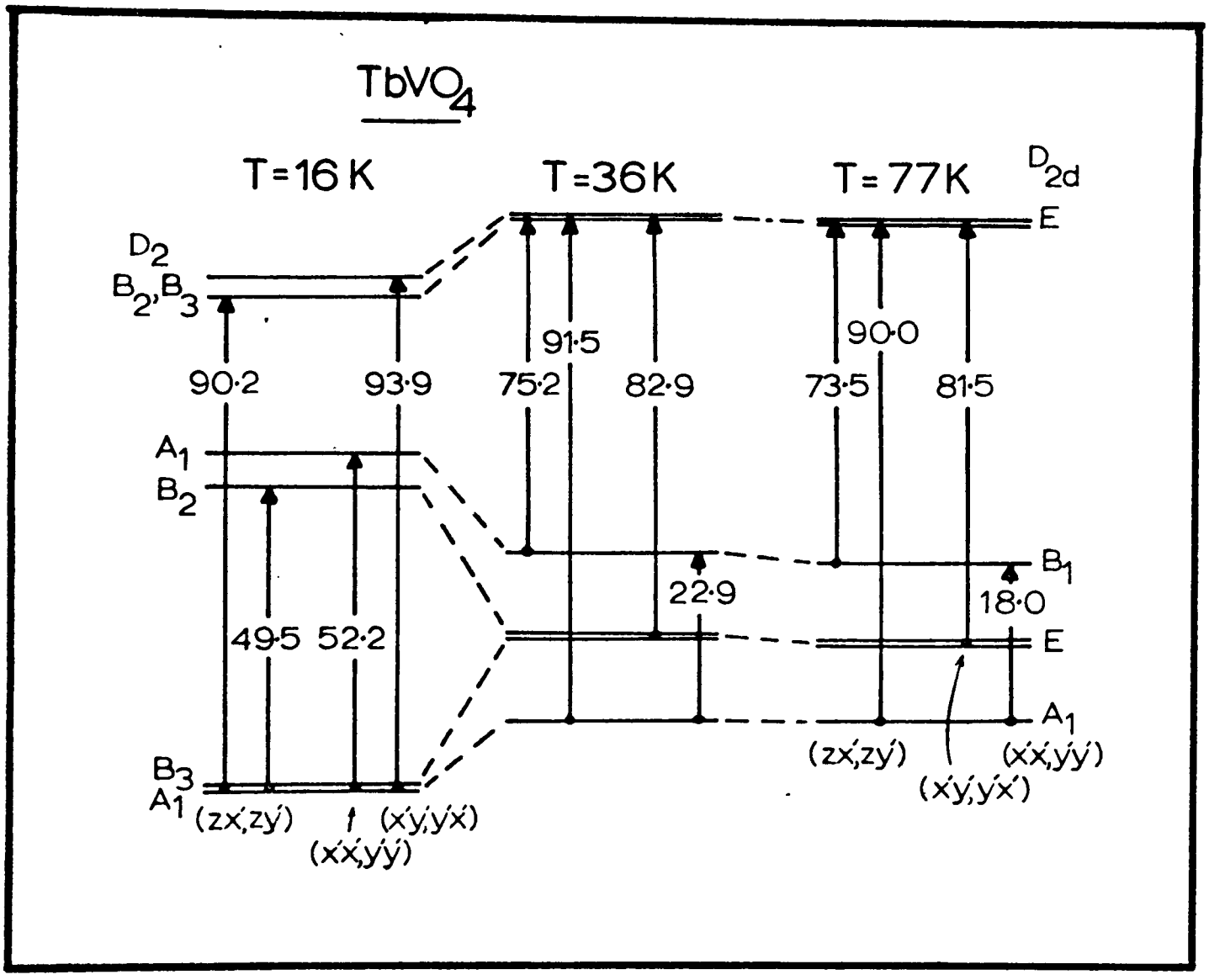
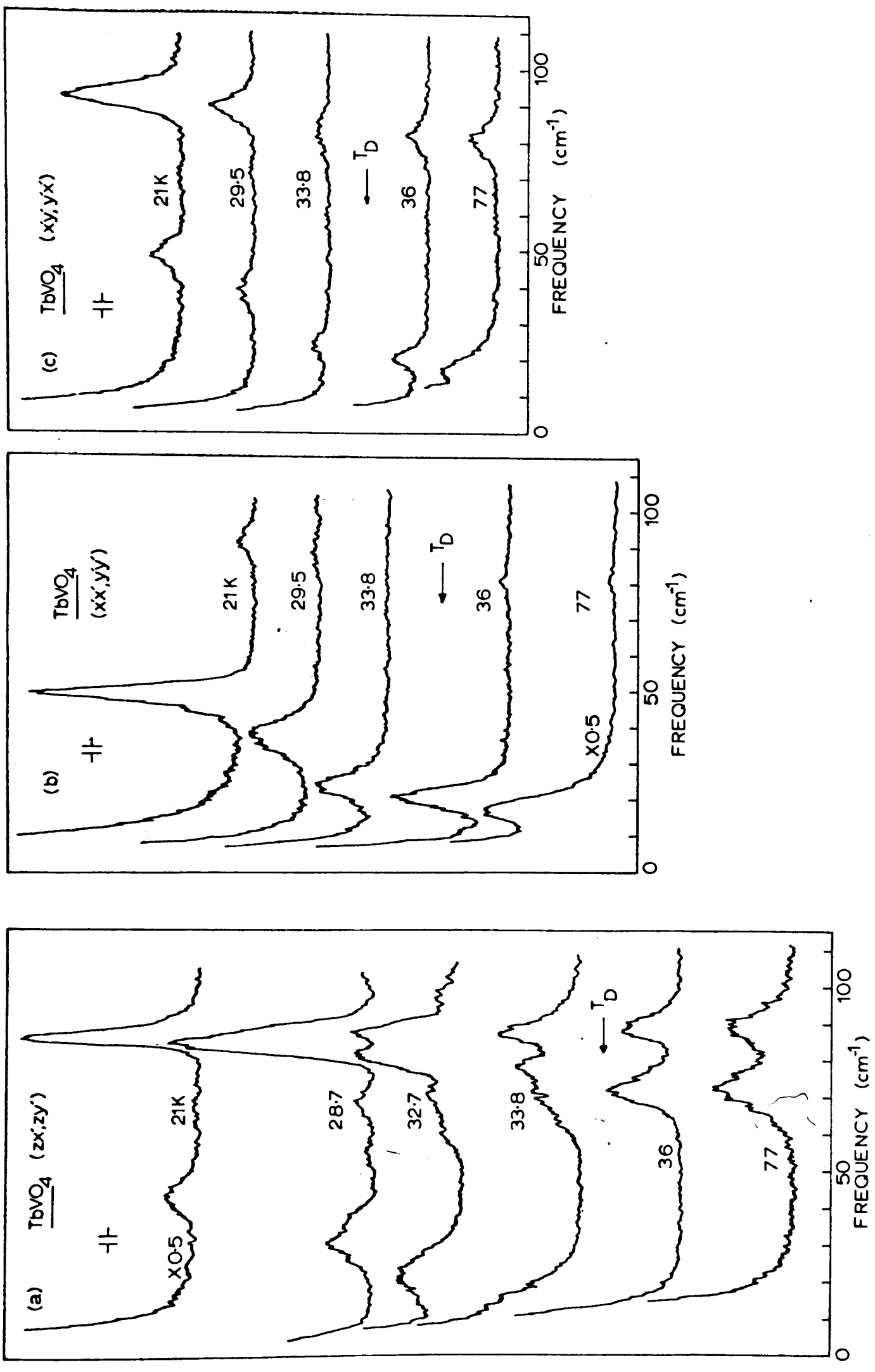


Fig. 5.4.



Electronic Raman spectra of $TbVO_4$ observed in three different polarizations for a range of temperatures. There was no measurable scattering in zz polarization.

(from Elliott et al 1972).

below T_D, see Fig. 5.3) This transition was studied in the mixed crystals (section 5.4). The ($x'y'$,$y'x'$) spectra showed some leakage of the ($x'x'$,$y'y'$) spectra due to the finite collection angle of the optics, together with a line at higher energy (Fig. 5.4(c)) which was interpreted as the E→E transition of the tetragonal phase (see also Fig. 5.3)(Elliott et al 1972).

A unique type of phase transition in the electronic energy level system of the type found in $TbVO_4$ was predicted theoretically by Elliott et al (1972) and Pytte and Stevens (1971) for a certain range of values of the electron-phonon coupling. In this case the crystal could exhibit a Jahn-Teller phase transition to a lower symmetry on cooling, but at a still lower temperature would go through a second transition, at which the crystal reverts to its original high temperature tetragonal structure. This effect does not occur in pure $TbVO_4$, but it seemed possible that the coupling in $TbVO_4$ might be brought into this critical range by diluting the crystals with Gadolinium. This chapter describes some experiments on the series of mixed crystals $Tb_cGd_{1-c}VO_4$ in which this effect was observed for a narrow concentration range. Although examples of phase changes in which the crystal symmetry increases on cooling are quite common, (e.g. $BaTiO_3$ and Rochelle salt; see Jona and Shirane 1962) it appears that this is the only clear example of a crystal which has the same symmetry at high and very low temperatures with an intermediate phase of lower symmetry.

Section 5.2 gives a review of the theory of Jahn-

Teller phase transitions in $TbVO_4$. In section 5.3 the experimental details of the work performed on these mixed crystals are given. The next two sections describe the results of the Raman scattering and birefringence studies respectively. Finally, the experimental results and the theory are compared in section 5.6.

5.2 Theory

Jahn and Teller (1937) showed that all non-linear molecules with a degenerate electronic ground state were unstable against a symmetry-lowering distortion. (Their theory excluded Kramer's or accidental degeneracies). The Jahn-Teller effect in solids arises from coupling between the electronic states and the phonons. The interaction Hamiltonian in the Rare Earth vanadates can be written as:-

$$\mathcal{H} = \sum_{\Gamma\alpha} B_\Gamma Q_{\Gamma\alpha} O_{\Gamma\alpha} \qquad (5.1)$$

where the summation is over all the components α of all the irreducible representations Γ of D_{2d}, the Rare Earth site symmetry. $Q_{\Gamma\alpha}$ represents a symmetrical combination of displacements on the ions surrounding the Rare Earth ion, and $O_{\Gamma\alpha}$ is an electronic operator. B_Γ is a coupling coefficient (Elliott et al (1972).

The ground state multiplet of Tb^{3+} is $^7F_6$. The

lowest four levels are two singlets separated by approximately $18cm^{-1}$ with a doublet almost midway between. All the remaining electronic levels are at a sufficiently high energy to be neglected. Measurements of the g-values of the lowest levels (below T_D) were made by Gehring et al (1971) and gave $g_{x'} = 16.3$, $g_{y'} = g_z = 0$. The maximum g-value is 18, so that the lowest states have almost the maximum allowed J. By considering the operations of the group D_{2d} on the four states, it can be shown that their symmetries are $A_1 + B_1 + E$. These states can be written down explicitly in terms of J_z (Elliott et al 1972).

The symmetric products of these states are $[A_1 \times A_1] = [B_1 \times B_1] = A_1$ and $[E \times E] = A_1 + B_1 + B_2$ while $A_1 \times E = E$ and $B_1 \times E = E$. Therefore the operators $O_{\Gamma\alpha}$ have non-zero matrix elements within these four levels for $\Gamma = A_1$, B_1, B_2 or E. Only lattice distortions with the same symmetries, (A_1, B_1, B_2 or E) will couple to the electronic levels. Theoretical estimates suggest that coupling to a B_1 symmetry distortion is at least an order of magnitude larger than coupling to any other symmetry. Either an A_{1u} or a B_{2g} lattice phonon will produce a B_1 symmetry displacement at a Tb^{3+} site, but from the known crystal space groups above and below T_D it was shown that the phase transition corresponded to a distortion of the lattice of B_{2g} symmetry (Elliott et al 1972). The electronic operators $O_{\Gamma\alpha}$ can be written in terms of six unitary 4 x 4 matrices.

$$\sigma^x = \begin{bmatrix} . & . & 1 & . \\ . & . & . & 1 \\ 1 & . & . & . \\ . & 1 & . & . \end{bmatrix} \quad \sigma^y = \begin{bmatrix} . & . & -i & . \\ . & . & . & -i \\ i & . & . & . \\ . & i & . & . \end{bmatrix} \quad \sigma^z = \begin{bmatrix} 1 & . & . & . \\ . & 1 & . & . \\ . & . & -1 & . \\ . & . & . & -1 \end{bmatrix}$$

$$\tau^x = \begin{bmatrix} . & 1 & . & . \\ 1 & . & . & . \\ . & . & . & 1 \\ . & . & 1 & . \end{bmatrix} \quad \tau^y = \begin{bmatrix} . & -i & . & . \\ i & . & . & . \\ . & . & . & -i \\ . & . & i & . \end{bmatrix} \quad \tau^z = \begin{bmatrix} 1 & . & . & . \\ . & -1 & . & . \\ . & . & 1 & . \\ . & . & . & -1 \end{bmatrix}$$

chosen so that terms in σ^z produce the distortion. On the Molecular Field model, the spin Hamiltonian for a Tb^{3+} site is given by

$$\mathcal{H}_{mf} = \left[\epsilon + \lambda_{A_{1g}} \langle \tfrac{1}{2}(1+\tau^z)\sigma^x \rangle\right] \tfrac{1}{2}(1+\tau^z)\sigma^x + \lambda_{B_{2g}} \langle \sigma^z \rangle \sigma^z \qquad (5.2)$$

assuming the lattice distortion has B_{2g} symmetry (Elliott et al 1972). Nelgecting the A_{1g} coupling as this does not lower the symmetry, and dropping the subscript B_{2g}, the Hamiltonian becomes

$$\mathcal{H} = \frac{\epsilon}{2}(1+\tau^z)\sigma^x + \lambda \langle \sigma^z \rangle \sigma^z \qquad (5.3)$$

The term in ϵ describes the unperturbed singlet-doublet-singlet level scheme, 2ϵ being the separation of the singlets above T_D. The operator σ^z produces the Jahn-Teller splitting in which the components of the doublet are split by $2\lambda\langle\sigma^z\rangle$ and the singlet levels by $2\left[\epsilon^2 + (\lambda\langle\sigma^z\rangle)^2\right]^{\frac{1}{2}}$.

$$\sigma^x = \begin{bmatrix} . & . & 1 & . \\ . & . & . & 1 \\ 1 & . & . & . \\ . & 1 & . & . \end{bmatrix} \quad \sigma^y = \begin{bmatrix} . & . & -i & . \\ . & . & . & -i \\ i & . & . & . \\ . & i & . & . \end{bmatrix} \quad \sigma^z = \begin{bmatrix} 1 & . & . & . \\ . & 1 & . & . \\ . & . & -1 & . \\ . & . & . & -1 \end{bmatrix}$$

$$\tau^x = \begin{bmatrix} . & 1 & . & . \\ 1 & . & . & . \\ . & . & . & 1 \\ . & . & 1 & . \end{bmatrix} \quad \tau^y = \begin{bmatrix} . & -i & . & . \\ i & . & . & . \\ . & . & . & -i \\ . & . & i & . \end{bmatrix} \quad \tau^z = \begin{bmatrix} 1 & . & . & . \\ . & -1 & . & . \\ . & . & 1 & . \\ . & . & . & -1 \end{bmatrix}$$

chosen so that terms in σ^z produce the distortion. On the Molecular Field model, the spin Hamiltonian for a Tb^{3+} site is given by

$$\mathcal{H}_{mf} = \left[\epsilon + \lambda_{A_{1g}} \langle \tfrac{1}{2}(1+\tau^z)\sigma^x \rangle\right] \tfrac{1}{2}(1+\tau^z)\sigma^x + \lambda_{B_{2g}} \langle \sigma^z \rangle \sigma^z \qquad (5.2)$$

assuming the lattice distortion has B_{2g} symmetry (Elliott et al 1972). Nelgecting the A_{1g} coupling as this does not lower the symmetry, and dropping the subscript B_{2g}, the Hamiltonian becomes

$$\mathcal{H} = \frac{\epsilon}{2}(1+\tau^z)\sigma^x + \lambda \langle \sigma^z \rangle \sigma^z \qquad (5.3)$$

The term in ϵ describes the unperturbed singlet-doublet-singlet level scheme, 2ϵ being the separation of the singlets above T_D. The operator σ^z produces the Jahn-Teller splitting in which the components of the doublet are split by $2\lambda\langle\sigma^z\rangle$ and the singlet levels by $2\left[\epsilon^2 + (\lambda\langle\sigma^z\rangle)^2\right]^{\frac{1}{2}}$.

The transition temperature, at which $\langle \sigma^z \rangle \to 0$, is given by

$$\frac{\lambda}{kT_D} + \frac{\lambda}{\epsilon} \operatorname{Sinh}\left(\frac{\epsilon}{kT_D}\right) = 1 + \operatorname{Cosh}\left(\frac{\epsilon}{kT_D}\right) \qquad (5.4)$$

For the mixed crystals the effect of changing the Tb concentration c can be represented by replacing λ by $c\lambda_0$ in equations (5.3) and (5.4,) where λ_0 is the value appropriate to pure $TbVO_4$ (Harley et al 1973(b)).

The splitting of the E_g phonon modes is expected to be proportional to the strain in the crystal, i.e. proportional to $c\langle \sigma^z \rangle$. $\langle \sigma^z \rangle$ and $\langle \sigma^x \rangle$ as a function of temperature are given by Elliott et al (1972).

For $T < T_D$.

$$\left.\begin{aligned} \langle \sigma^z \rangle &= \left[\frac{\lambda\langle \sigma^z \rangle}{W_1} \operatorname{Sinh}\left(\frac{W_1}{kT}\right) + \operatorname{Sinh}\left(\frac{W_2}{kT}\right)\right]\left[\operatorname{Cosh}\left(\frac{W_1}{kT}\right) + \operatorname{Cosh}\left(\frac{W_2}{kT}\right)\right]^{-1} \\ \langle \sigma^x \rangle &= \frac{\epsilon}{W_1} \operatorname{Sinh}\left(\frac{W_1}{kT}\right)\left[\operatorname{Cosh}\left(\frac{W_1}{kT}\right) + \operatorname{Cosh}\left(\frac{W_2}{kT}\right)\right]^{-1} \end{aligned}\right\} \qquad (5.5)$$

where $$W_1 = \left[\epsilon^2 + (\lambda\langle \sigma^z \rangle)^2\right]^{\frac{1}{2}}$$

and $$W_2 = \lambda\langle \sigma^z \rangle \qquad (5.6)$$

and for $T \gg T_D$

$$\left.\begin{aligned} \langle \sigma^z \rangle &= 0 \\ \langle \sigma^x \rangle &= \operatorname{Tanh}\frac{\epsilon}{2kT} \end{aligned}\right\} \qquad (5.7)$$

Equation (5.5) was used to calculate $c\langle \sigma^z \rangle$ which gave the solid lines plotted in Figs. 5.6 → 5.9. These are normalized to the experimental phonon splittings

in pure $TbVO_4$ at low temperatures.

Equation (5.4) has a single solution for T_D if $\lambda > \epsilon$ and no solution if $\lambda < 0.83\epsilon$. For the intermediate range $\epsilon > \lambda > 0.83\epsilon$ there are two solutions. Values of $\lambda = c\lambda_0$ satisfy the two solution condition in a narrow concentration range centred on $c = 0.34$ for $Tb_cGd_{1-c}VO_4$.

Physically, this behaviour can be explained by considering the situation which gives the minimum free energy. At T = 0 only the lowest singlet level is populated, and there is no distortion unless $\lambda > \epsilon$ (Elliott et al 1972). However, if $\lambda < \epsilon$ it is possible for a Jahn-Teller distortion to occur as the temperature is raised from T = 0. The doublet level then becomes thermally populated, and a doublet level by itself can have a distortion for any value of λ. As the temperature is raised still further any distortion eventually vanishes when the upper components of the four level system become thermally populated and cause the unperturbed phase to have the minimum free energy. Thus a situation can be visualized in which the crystal goes through a Jahn-Teller phase transition to a lower symmetry on cooling, but at lower temperatures has a second transition at which the crystal reverts to its original high temperature symmetry.

The electronic excitations measured by Raman scattering are essentially at $\underline{k} = 0$, whereas the Molecular Field theory used so far is a single-ion theory and gives a result for the energies which represents an average over $\underline{k}$

space. A more general theory was developed by Elliott et al (1972) which gave the exact equations of motion of the operators σ and τ. These were decoupled using the Random Phase Approximation, and produced dispersion curves for the coupled electron-phonon modes. From this theory the frequency of the singlet-singlet electronic transition at small $\underline{k}$ is found to be

$$\hbar^2\omega(\underline{k})^2 = 4\left\{\left[J'\langle\sigma^z\rangle\right]^2 + \epsilon\left[\epsilon - \left\{J(\underline{k}) - k_a(\underline{k})\right\}\langle\sigma^x\rangle\right]\right\} \quad (5.8)$$

where J' includes the strain coupling and $K_a(\underline{k})$ is the acoustic mode coupling coefficient. This equation was used to plot the theoretical lines in Figs. 5.13 - 5.16.

Above T_D, and at $\underline{k} = 0$ this becomes

$$\left.\begin{aligned}\hbar^2\omega(0)^2 &= 4\epsilon\left[\epsilon - J(0)\langle\sigma^x\rangle\right] \\ &\simeq 4\epsilon^2\left[1 - J(0)/2kT\right]\end{aligned}\right\} \quad (5.9)$$

where $$J(0) = \left[J(\underline{k}) - k_a(\underline{k})\right]_{k=0} \quad (5.10)$$

and $$\langle\sigma^x\rangle = \tanh\left(\epsilon/2kT\right) \quad (5.11)$$

above T_D.

Elliott et al (1972) showed that the width of the electronic excitations seen in Raman scattering decreased with the number of interacting neighbours. Above T_D, and assuming equal coupling to each of the n neighbours, they found

$$\left(\frac{\omega(0)}{\Delta\omega}\right)^2 \simeq n \quad (5.12)$$

where $\omega(\circ)$ is the frequency of the singlet-singlet electronic transition at T = 0 and $\Delta\omega$ is its width just above T_D. For $TbVO_4$ this gave $n \simeq 25$, further evidence that the interaction is relatively long range. The corresponding value for $DyVO_4$ was $n \simeq 4$, where the interaction is of much shorter range and the MFA inapplicable.

5.3 Experimental

The mixed crystals of $Tb_cGd_{1-c}VO_4$ were flux grown by Dr. S.H.Smith in this laboratory. They were pale green in colour, and of good optical quality. A typical size of crystal was 5 x 1 x 1m.m., and their growth habit was with the z axis parallel to the longest side, and the x' and y' axes at 45° to the other faces. The crystal faces were all polished with diamond paste. The compositions of the mixed crystals were determined by X-ray fluorescence analyses on powdered samples. This determined the Tb concentration, c, to within $\pm$ 2%.

A series of $Tb_cY_{1-c}VO_4$ crystals were also grown, but thes were found to have gross internal strains at room temperature (presumably because of the size mismatch between Tb^{3+} and Y^{3+}) and were not used in this investigation.

The Raman spectra were obtained with the crystals mounted in the variable temperature cryostat (section 3.5). The crystals were lightly glued at one end and the laser focused onto the crystal near the other end. This ensured

that the method of mounting did not strain the region of the crystal that was being studied. The spectra were obtained using about 50mW of 514.5n.m. laser light, (the crystals fluoresced strongly when illuminated with 488.0n.m. radiation). The lowest possible power was used to minimize local heating in the crystal. An estimate of the local heating was obtained by fixing the temperature just below the observed transition point (where the splitting of the E_g phonon mode varied most rapidly with temperature) and noting any change in the splitting as the laser power was reduced. The spectrometer slit settings used gave a measured resolution of $0.6cm^{-1}$.

The birefringence experiments were performed in the same cryostat, using the method described in section 3.7. The light source used was a high pressure mercury lamp made approximately monochromatic ($\lambda \sim 500$n.m.) by the use of suitable filters. The interference patterns obtained when convergent polarized light propagated along the c-axis of the crystal were observed as a function of temperature. For both Raman and the birefringence measurements the temperatures were measured above $4^{o}K$ by a thermocouple in contact with the crystal, and below $4^{o}K$ from the helium vapour pressure.

5.4 Raman Spectra

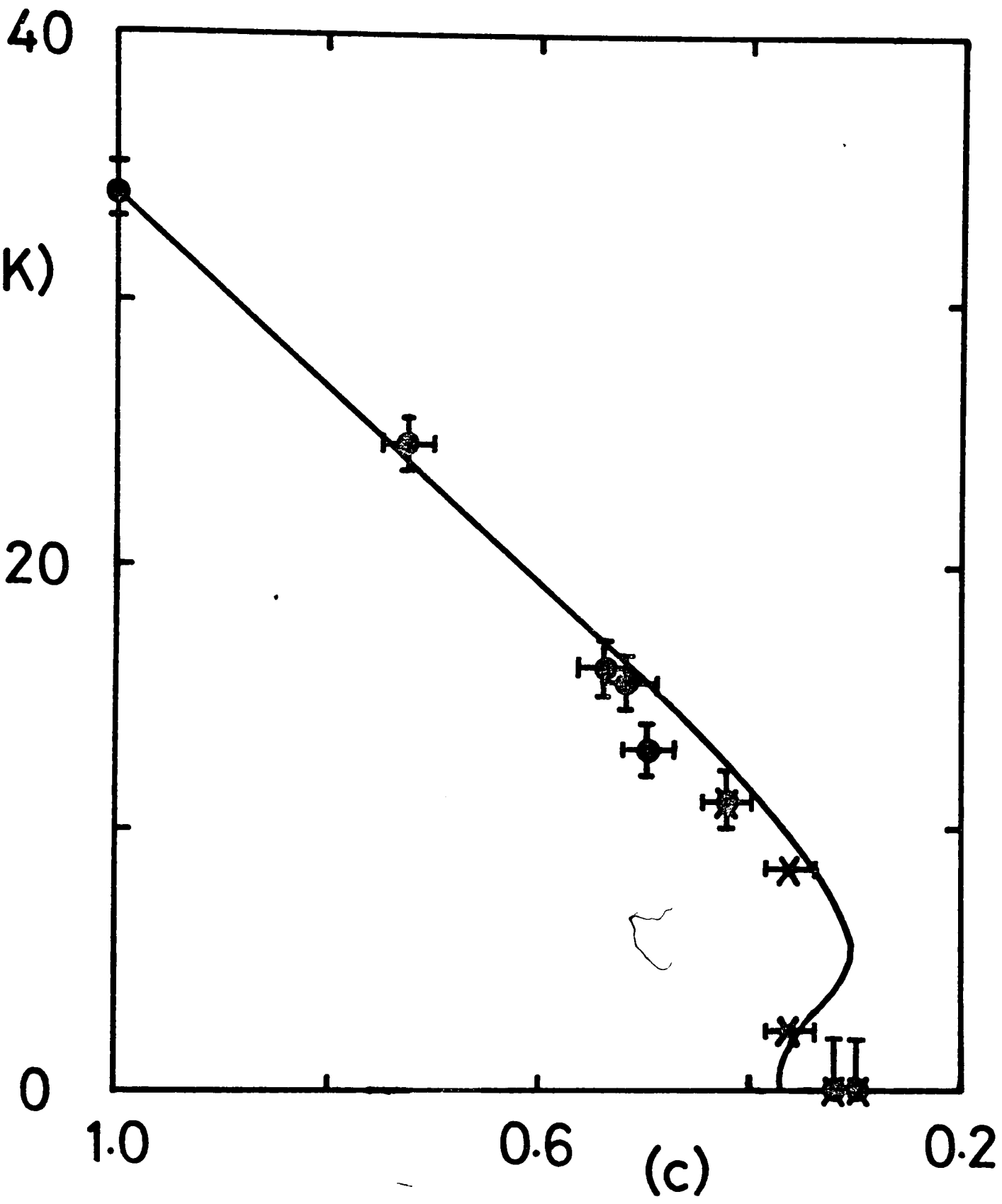
The transition temperatures, T_D of all the mixed

crystals are shown as a function of Tb concentration in Fig. 5.5. The crosses were obtained from the birefringence experiments (next section) and the circles from Raman measurements. The latter were determined from the splittings in the D_{2h}^{24} phase of the doubly degenerate E_g phonon modes of the tetragonal phase; the splittings tended to zero at T_D. One of the crystals, with c = 0.365, showed the two phase transitions predicted by the theory (section 5.2). For Tb concentrations less than c = 0.32 no Jahn-Teller phase transition was observed down to the lowest attainable temperature, 1.8°K. The solid line was obtained from the MFA and is discussed in section 5.6.

Fig. 5.6 shows the splittings of two of the E_g phonons as a function of temperature for the c = 0.725 crystal. The circles denote E_g^{I} and the crosses E_g^{III}, using the notation of Elliott et al (1972). One other E_g mode could be seen in the spectrum, but leakage of the nearby intense B_{2g} mode made measurements of the splitting difficult. Corresponding results for c = 0.72 are shown in Fig. 5.7, and for c = 0.425 in Fig. 5.8. The lines show the theoretical predictions of the MFA, (section 5.6).

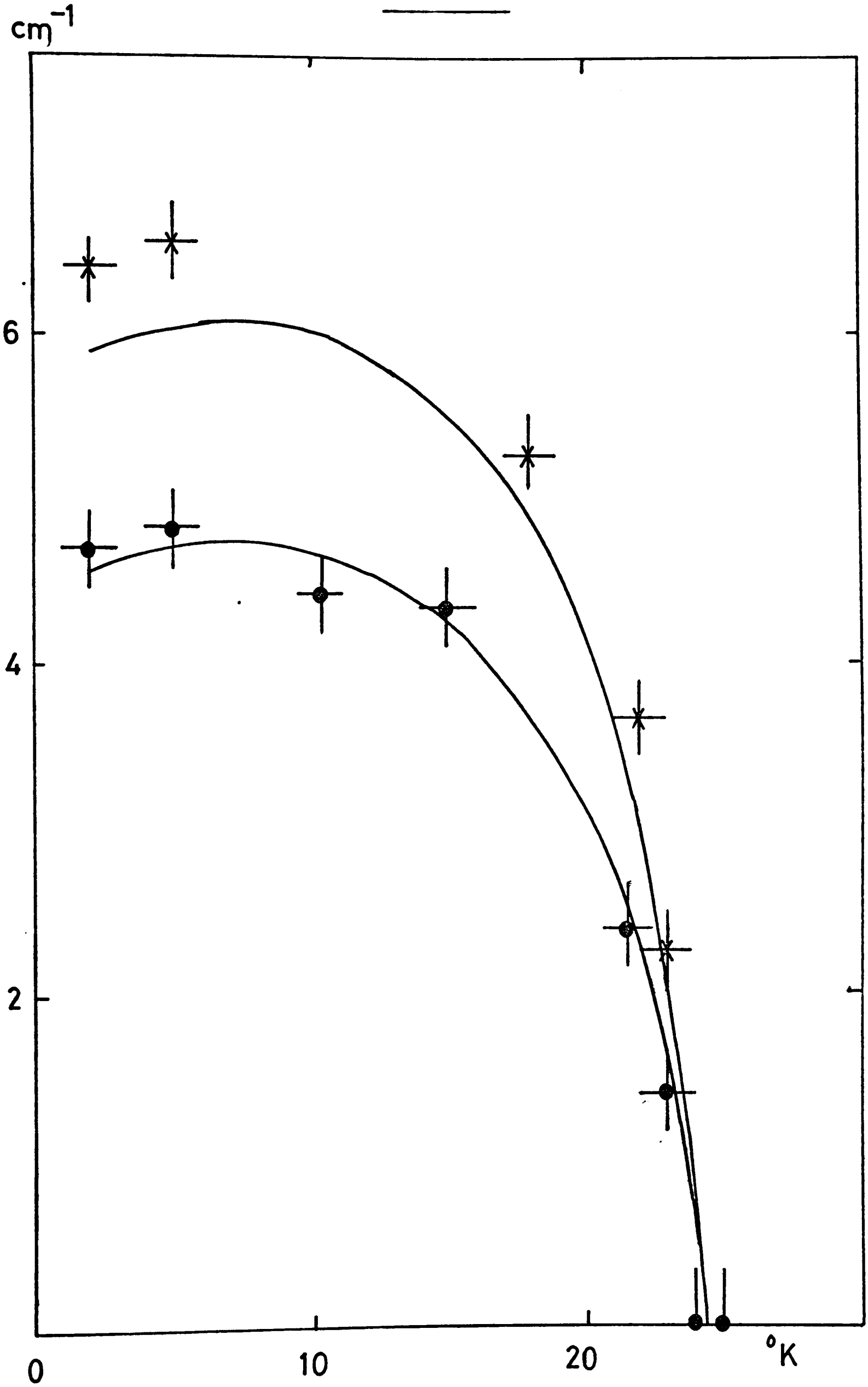
Fig. 5.9. shows the splitting of the $827cm^{-1}$ E_g phonon mode for $Tb_{0.365}Gd_{0.635}VO_4$ as a function of temperature. Although the splitting is clearly resolvable at 5°K local heating caused by the focused laser beam (power ~ 50mW) made the determination of temperature imprecise. The measured values of temperature plotted in Fig. 5.9 are therefore lower

Fig. 5.5.



Transition temperatures of $Tb_cGd_{1-c}VO_4$ determined by Raman measurements (circles) and optical birefringence (crosses.) Solid line is given by the MFA.

Fig. 5.6.



c = 0.725. Eg phonon splittings as a function of temperature
Circles = E_g^I; Crosses = E_g^{III}. Solid lines given by MFA

Fig. 5.7.

c = 0.52. E_g phonon splittings as a function of temperature. Circles = E_g^{I}; Crosses = E_g^{III}. Solid lines given by MFA (section 5.6).

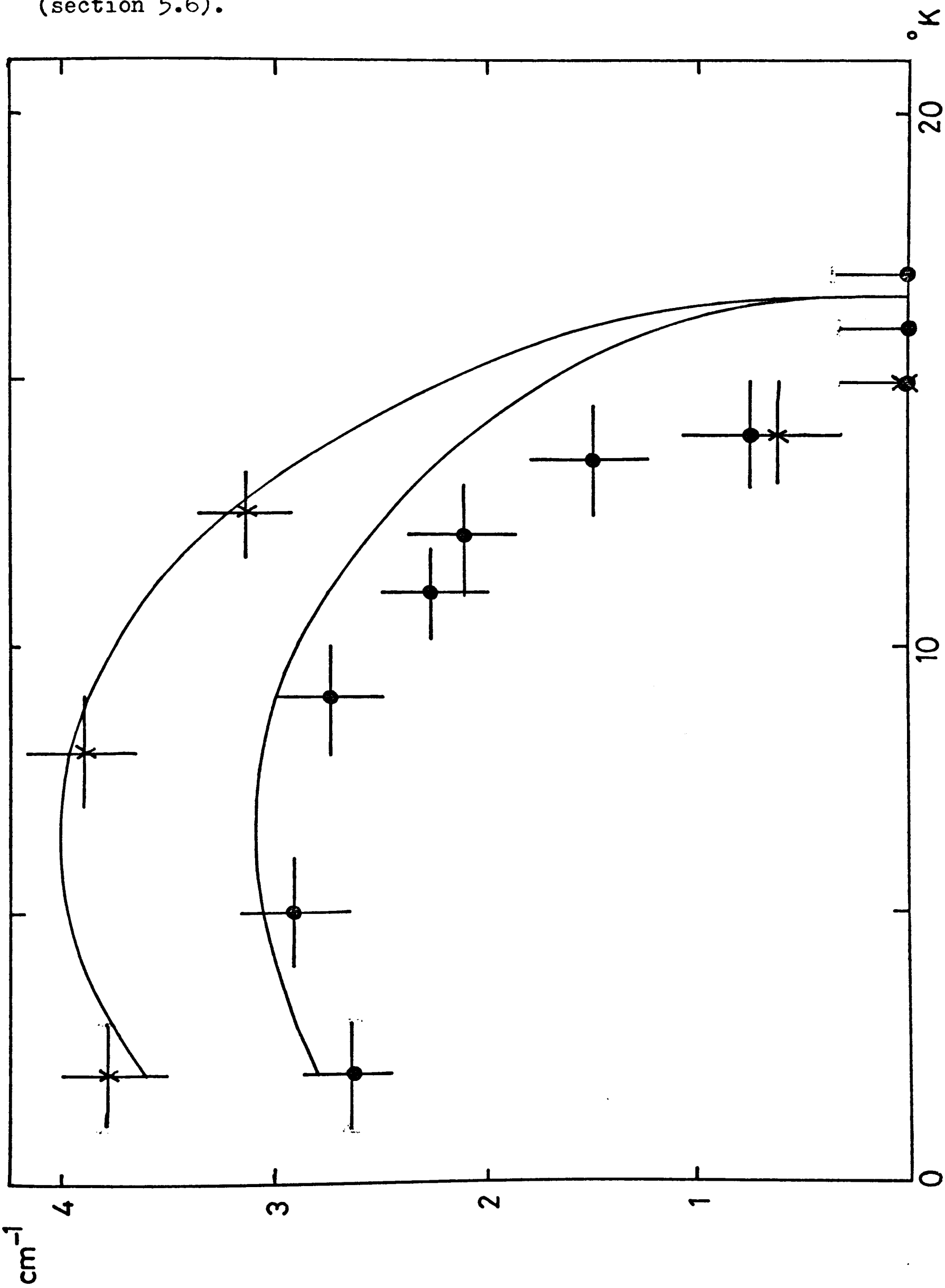


Fig. 5.8.

c = 0.425. E_g phonon splittings as a function of temperature. Circles = E_g^I; Crosses = E_g^{III}. Solid lines given by MFA (section 5.6).

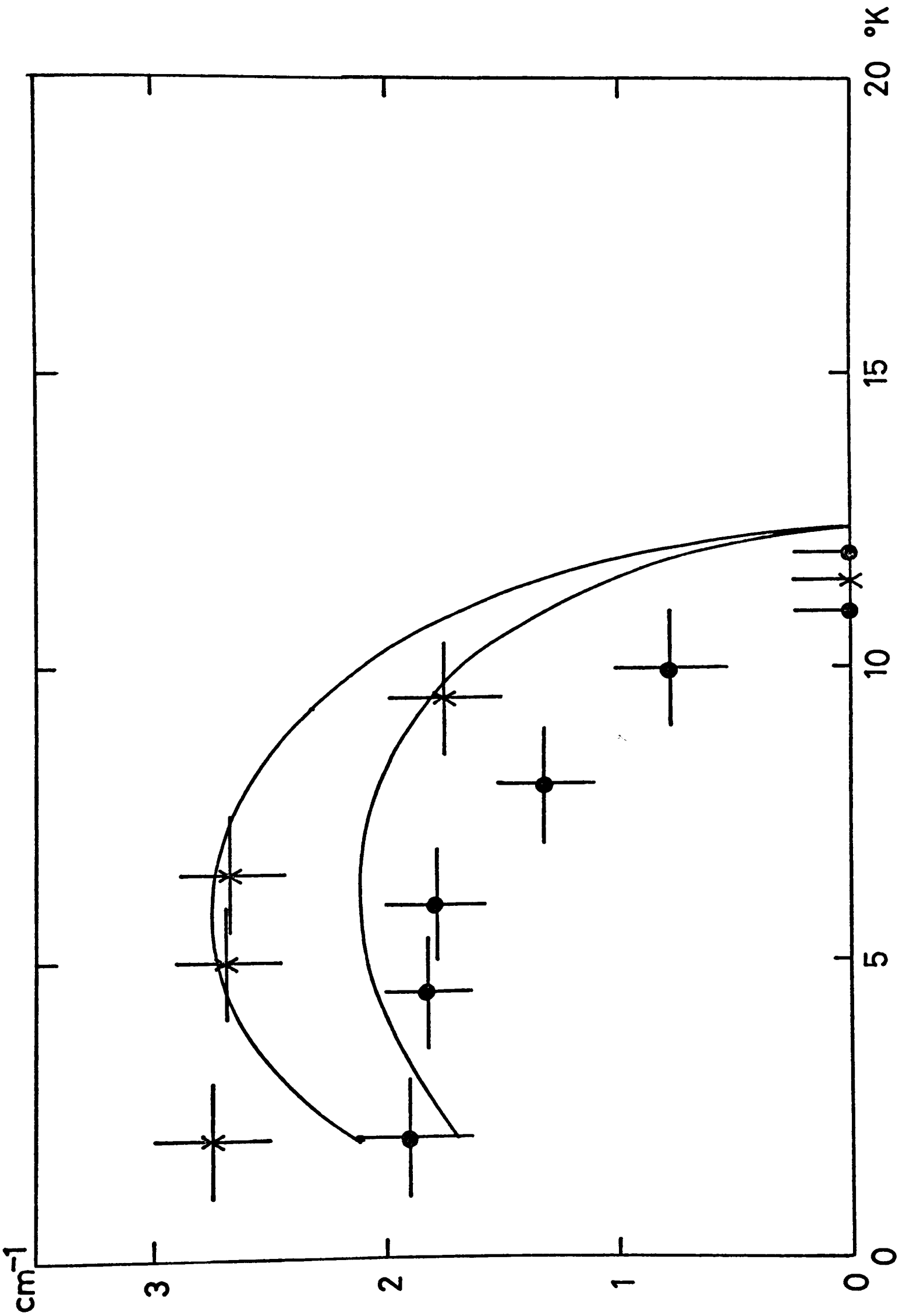
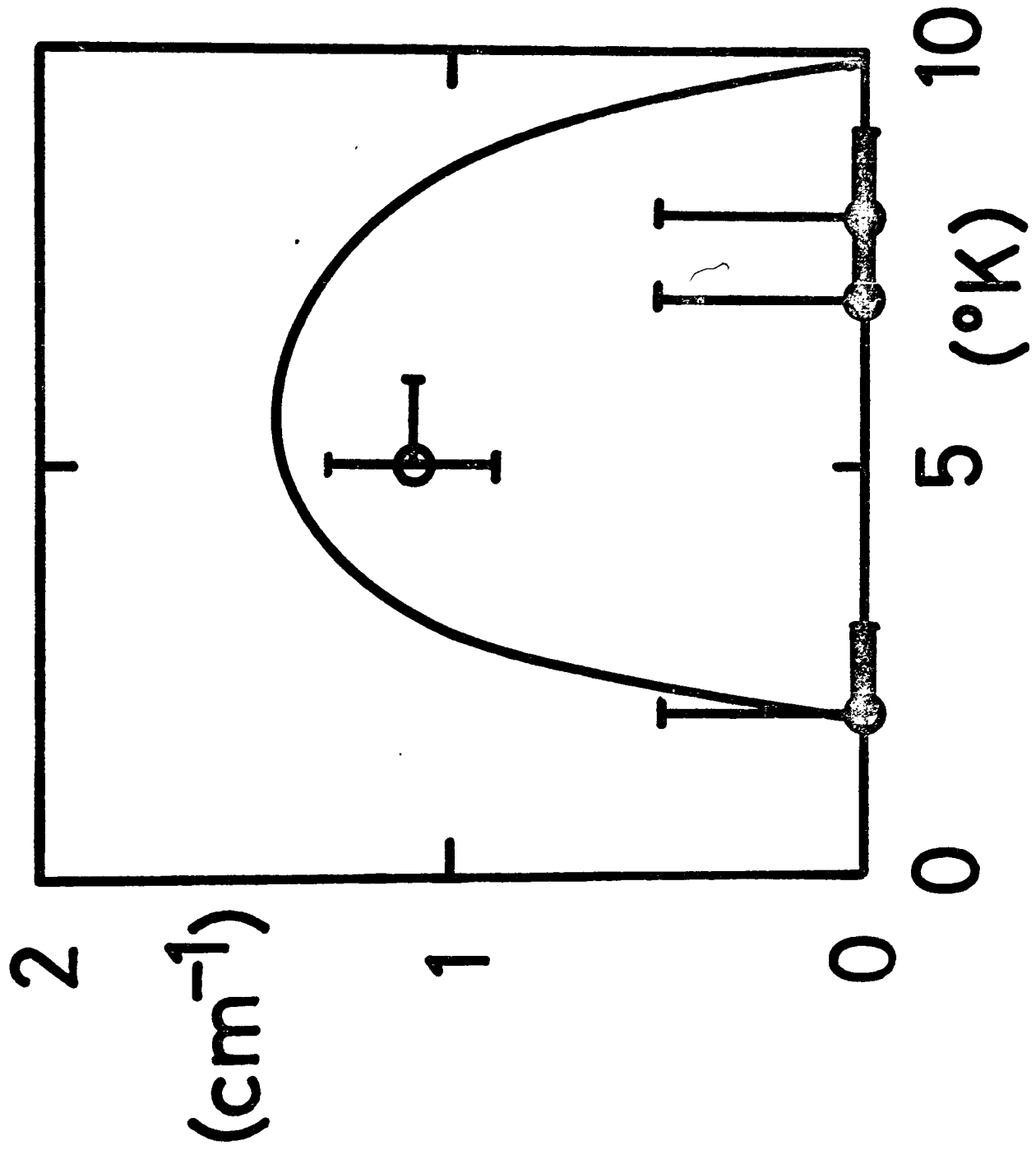


Fig. 5. 9.

Temperature dependance of the splitting of the E_g^I phonon mode at $827cm^{-1}$ in the Raman spectrum for $c = 0.365$. Solid curve given by MFA (section 5.6).



limits to the true temperature of the scattering volume, as indicated by the horizontal error bars (see also Fig 5.10) In another experiment with the crystal immersed in superfluid helium the laser power was progressively increased and a splitting developed in the E_g mode which disappeared at higher laser power as the local heating due to the laser raised the temperature through the two phase transitions. Thus, the Raman measurements show that the crystal is orthorhombic at 5^oK and tetragonal at both higher and lower temperatures. The solid curve is calculated from the MFA (section 5.6). The E_g^{III} phonon was less intense and so a slightly higher laser power was required to observe it. This unfortunately increased the local heating so that no splitting could be detected.

Traces of the actual E_g^{I} modes spectra at 4.2^oK and 1.9^oK for this crystal are given in Fig. 5.10. The resolution was $0.6cm^{-1}$, and the splitting can just be resolved at 4.2^oK. On cooling to 1.9^oK the splitting could no longer be detected, and the overall width of the line had decreased by about 40%

The E_g^{I} phonon splittings at 5^oK are plotted against the Tb concentration in Fig. 5.11. The solid line is the molecular field theory prediction, (see section 5.6) and is fitted only to the observed splitting in pure $TbVO_4$. Corresponding results for the E_g^{III} phonon are given in Fig.5.12.

As well as the phonon spectra, electronic transitions between the levels of the Tb^{3+} ions were measured in the mixed

Fig. 5.10.

Raman spectra showing E_g^I phonon at 4.2°K and 1.9°K for c = 0.365. Resolution = 0.6cm^{-1}.

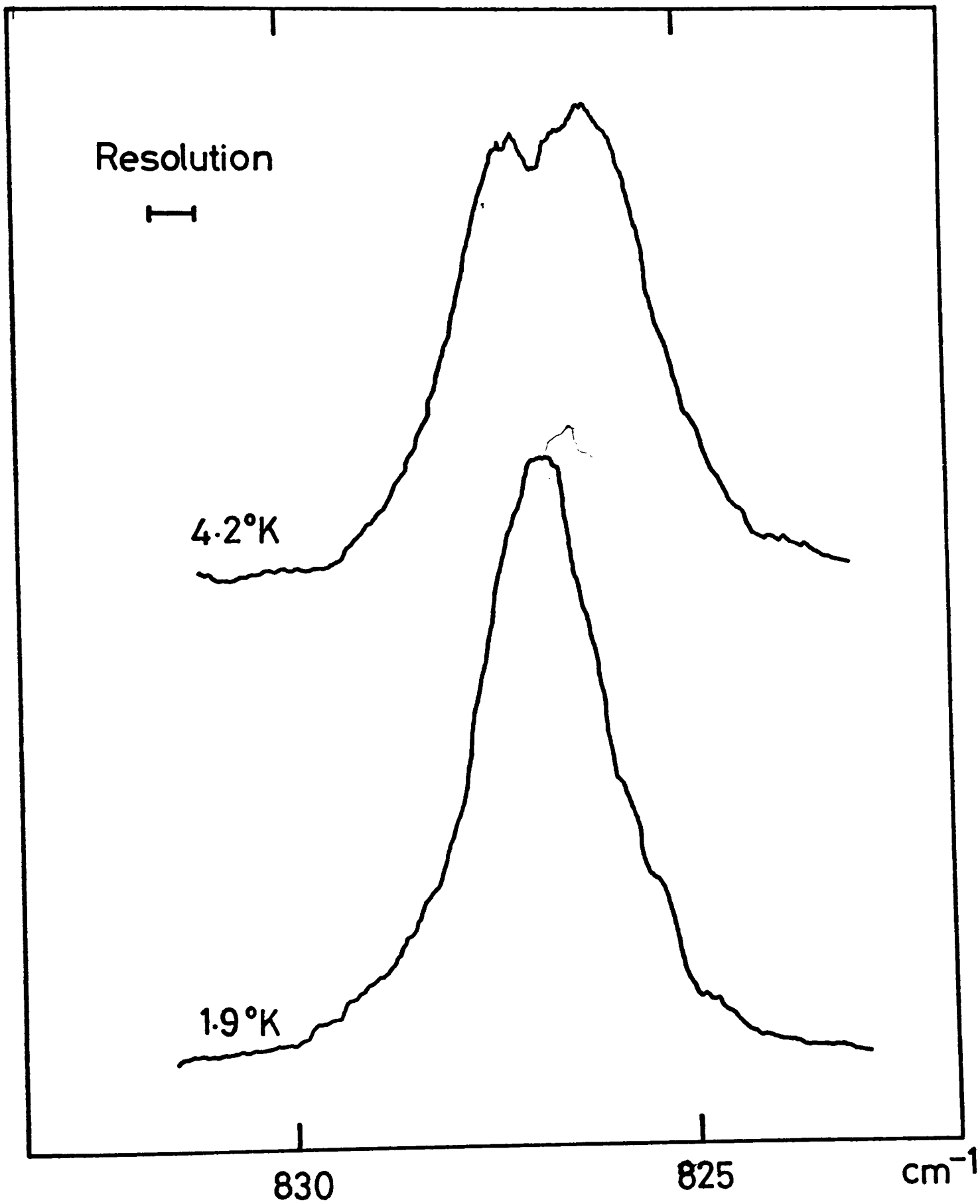


Fig. 5.11.

E_g^I phonon splittings at 5^oK as a function of c. Solid line given by MFA (section 5.6).

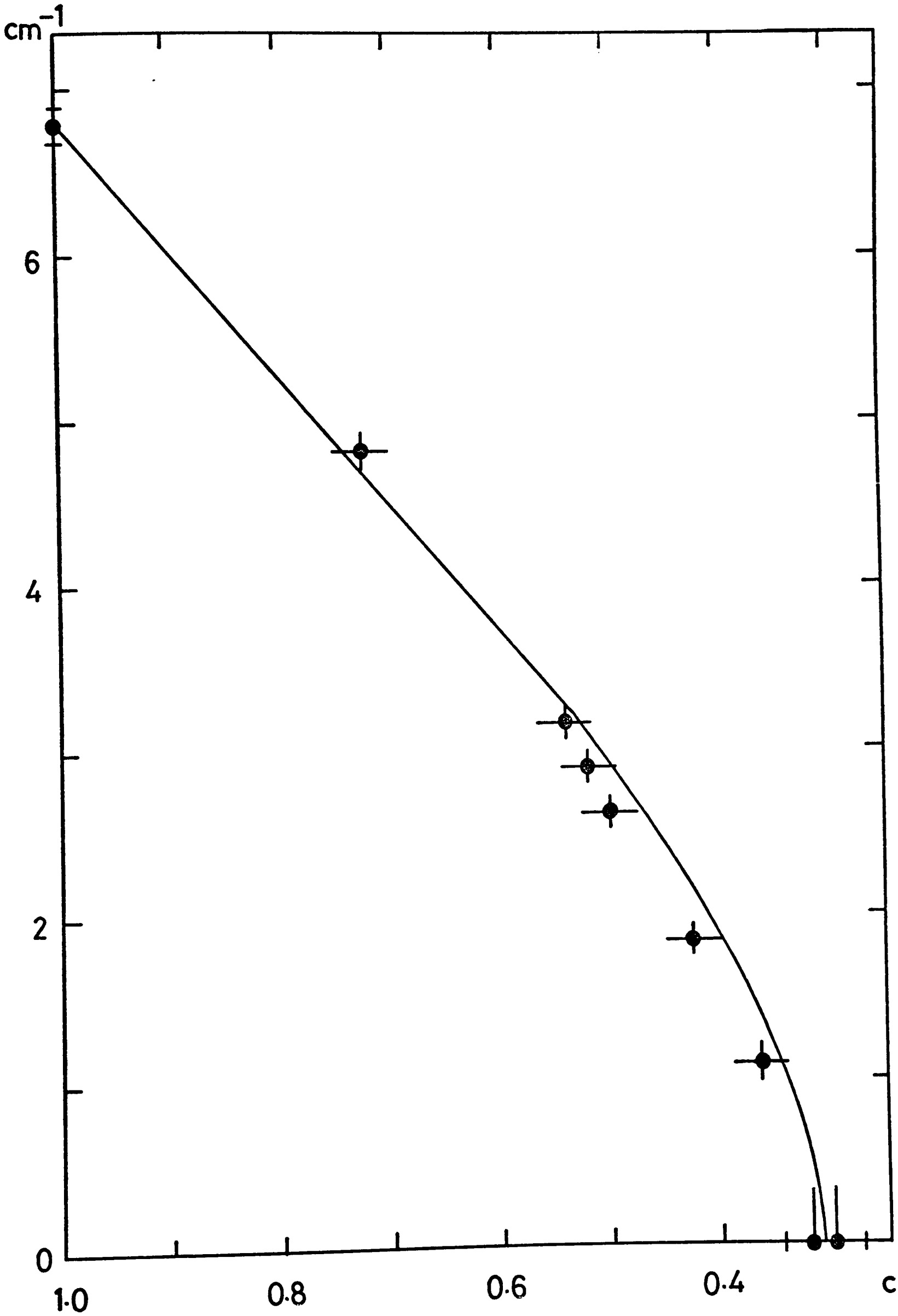
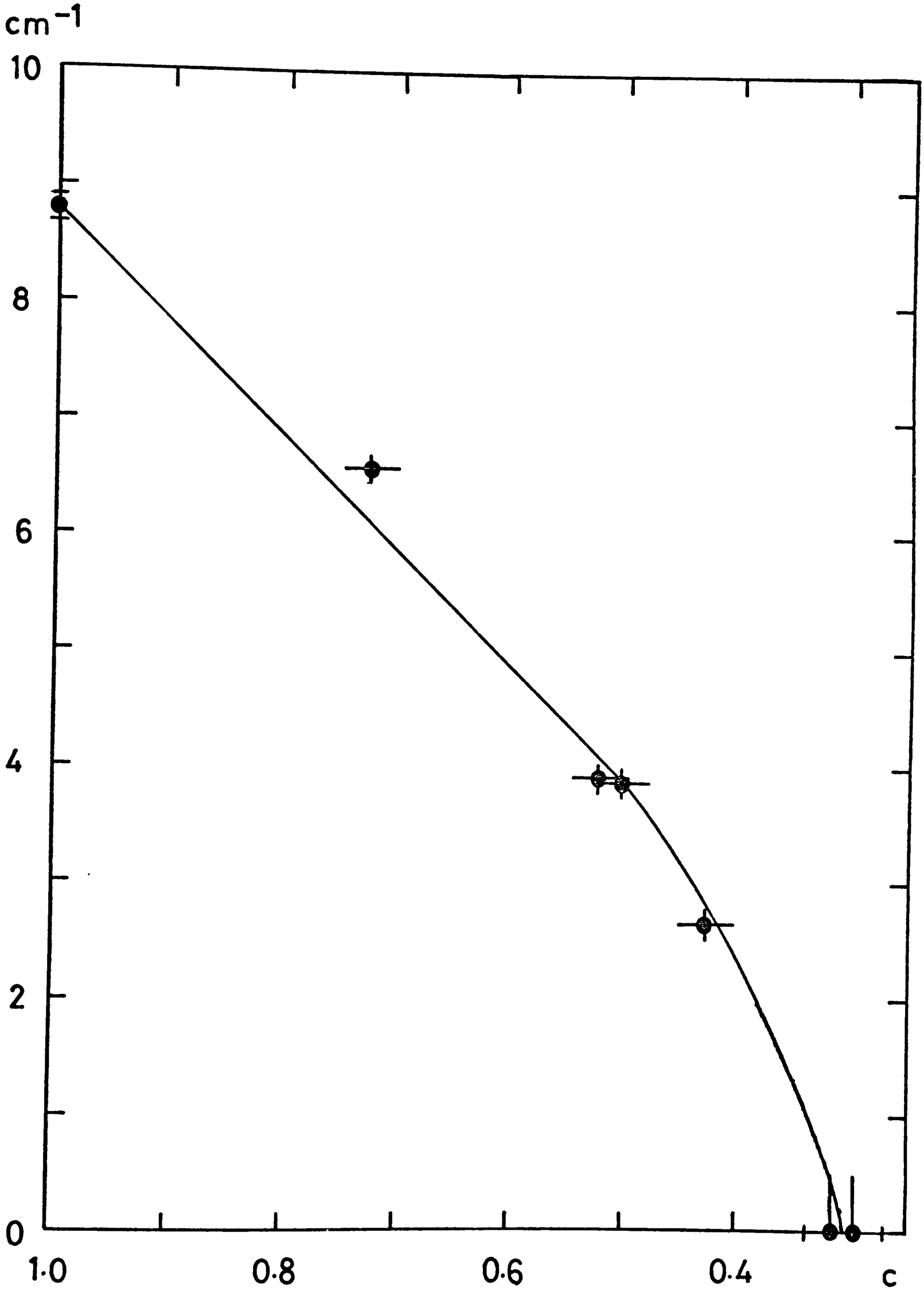


Fig. 5.12.

E_g^{III} phonon splittings at 5^oK as a function of c.
Solid line given by MFA (section 5.6.)



crystals. Of particular interest was the $A_1 \rightarrow A_1$ transition (see Fig. 5.3) in the orthorhombic phase, ($A_1 \rightarrow B_1$ in the tetragonal phase), which should have appeared in ($x'x'$) and ($y'y'$) polarizations. The spectra were recorded in the (xy) polarization, consistent with the principal axes x' and y' being at 45^o to the crystal faces (x and y axes), see Fig 5.1. The energy of this electronic transition is plotted as a function of temperature for c = 0.725 in Fig. 5.13. The results for the c = 0.52 crystal are given in Fig. 5.14, for c = 0.425 in Fig. 5.15, and for c = 0.365 in Fig. 5.16. Again, the solid lines are the predictions of the MFA (see section 5.6).

5.5 Birefringence Experiments

Four of the mixed crystals were studied using the birefringence technique discussed in Chapter 3. These were the crystals with c = 0.425, 0.365, 0.320 and 0.300. The patterns obtained for the c = 0.365 crystal at various temperatures are shown in Figs. 5.17(a) and (b). The patterns at 9.0^oK and 2.2^oK indicate that the crystal is uniaxial (with perhaps some slight strain frozen in during the growth of the crystal) whereas those at 8.3^oK and 4.2^oK show that the crystal is biaxial with optic axes at 45^o to the growth faces of the crystal. (The crystal faces were parallel to the sides of the page). The two photographs at 4.2^oK were taken with the light passing through different portions of the crystal.

Fig. 5.13.

c = 0.725. Temperature dependance of the lowest electronic Raman mode. Solid curve given by MFA (section 5.6).

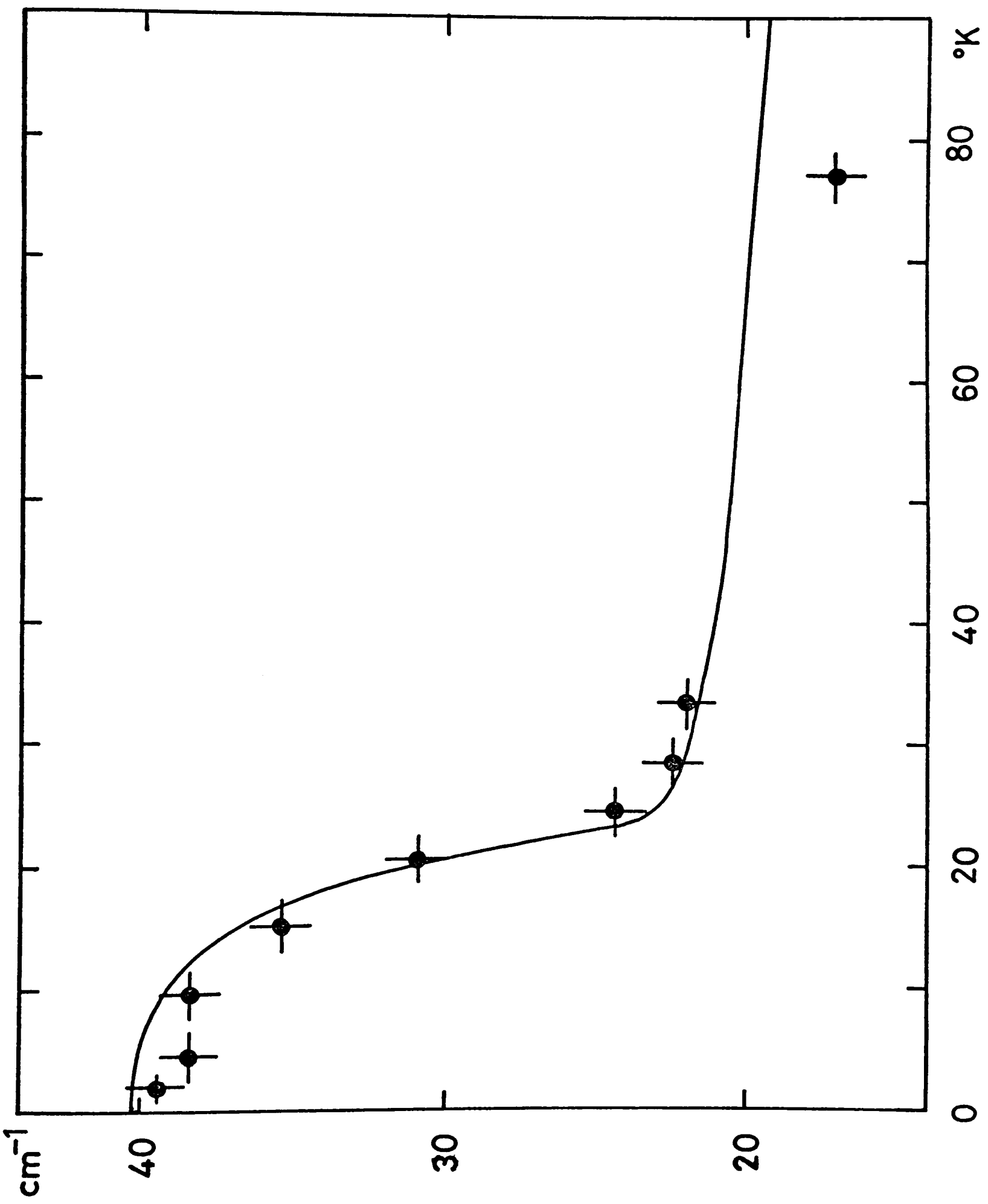


Fig. 5.14.

c = 0.52. Temperature dependance of the lowest electronic Raman mode. Solid curve given by MFA (section 5.6).

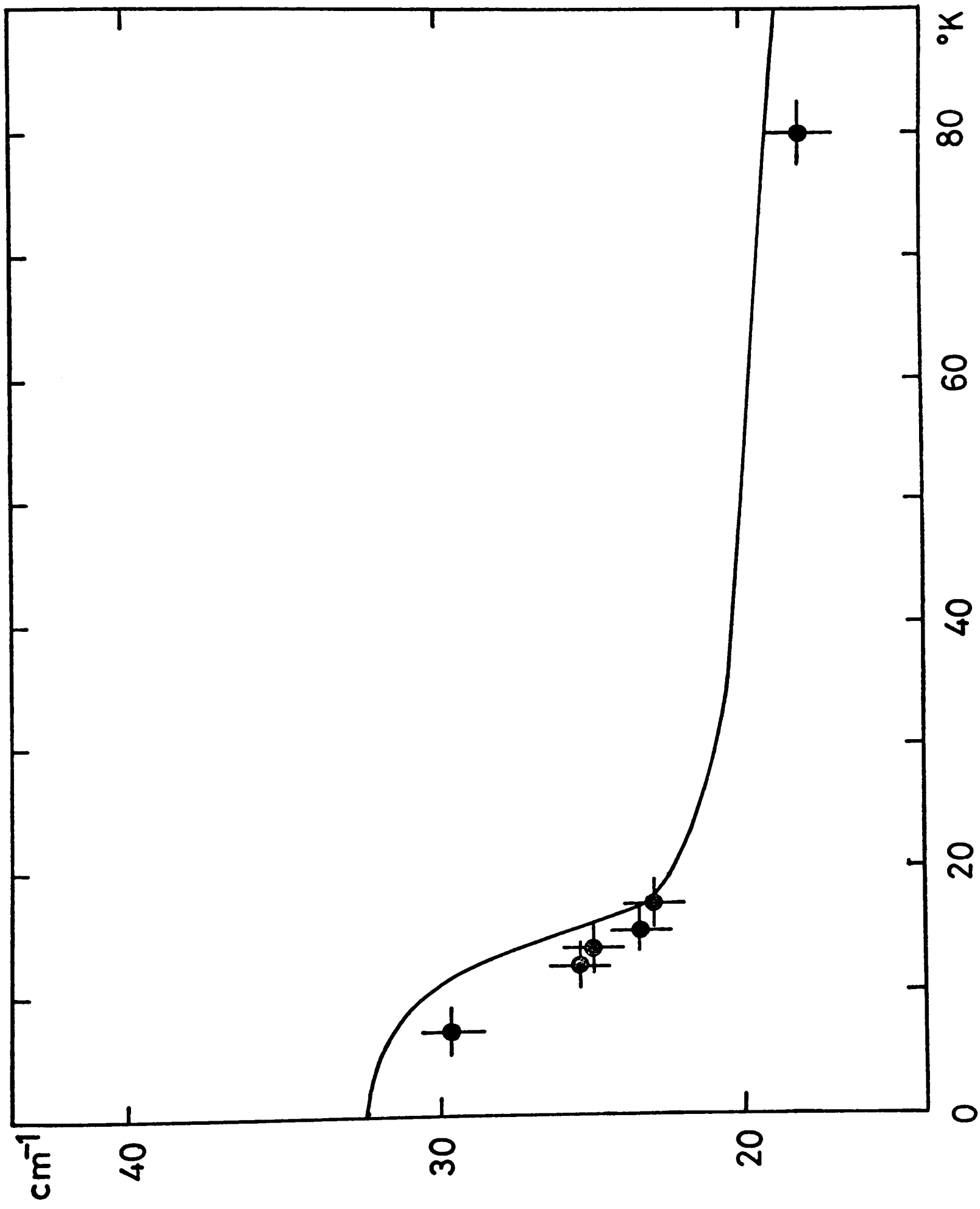


Fig. 5.15.

c = 0.425. Temperature dependance of the lowest electronic Raman mode. Solid curve given by MFA (section 5.6).

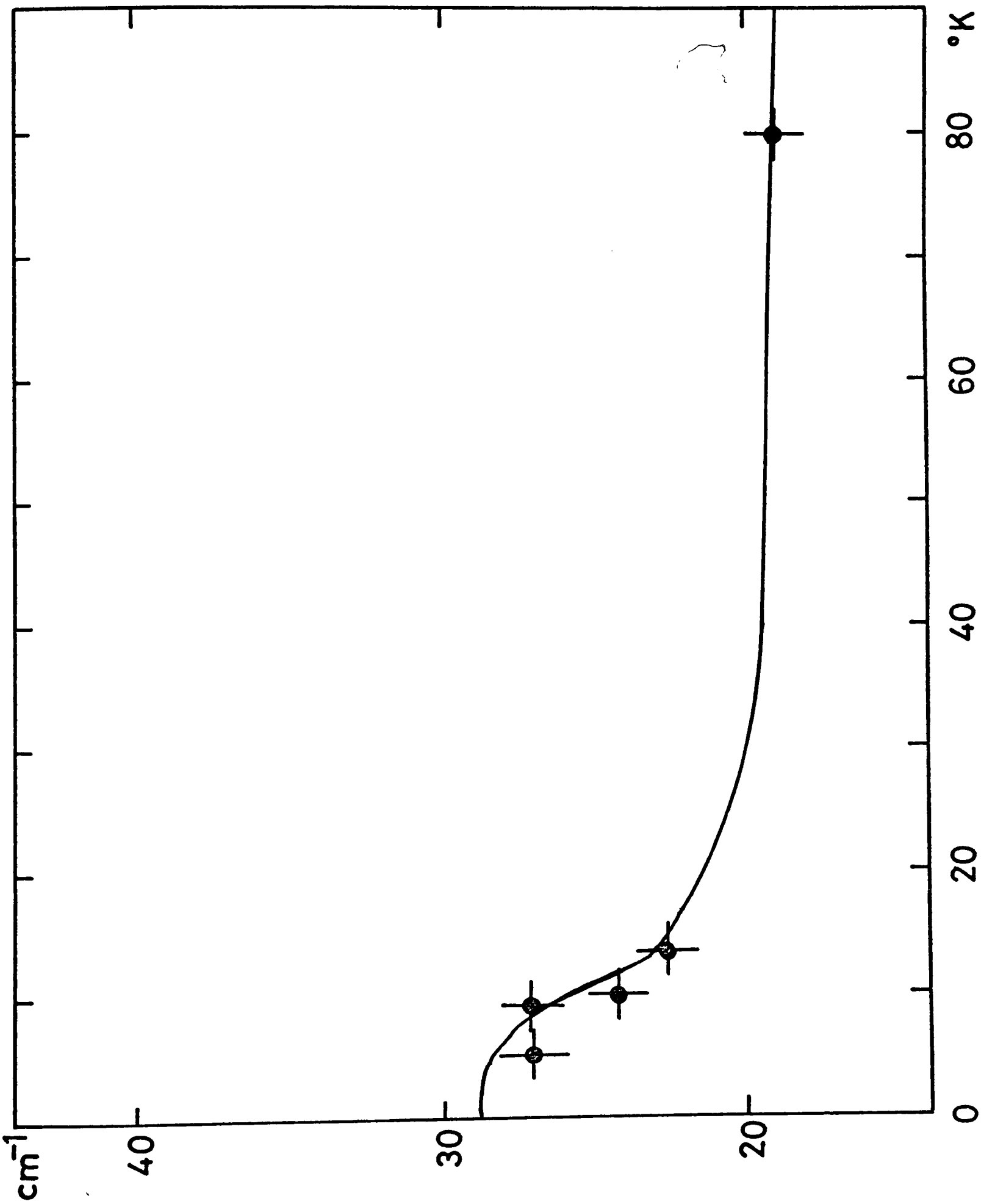
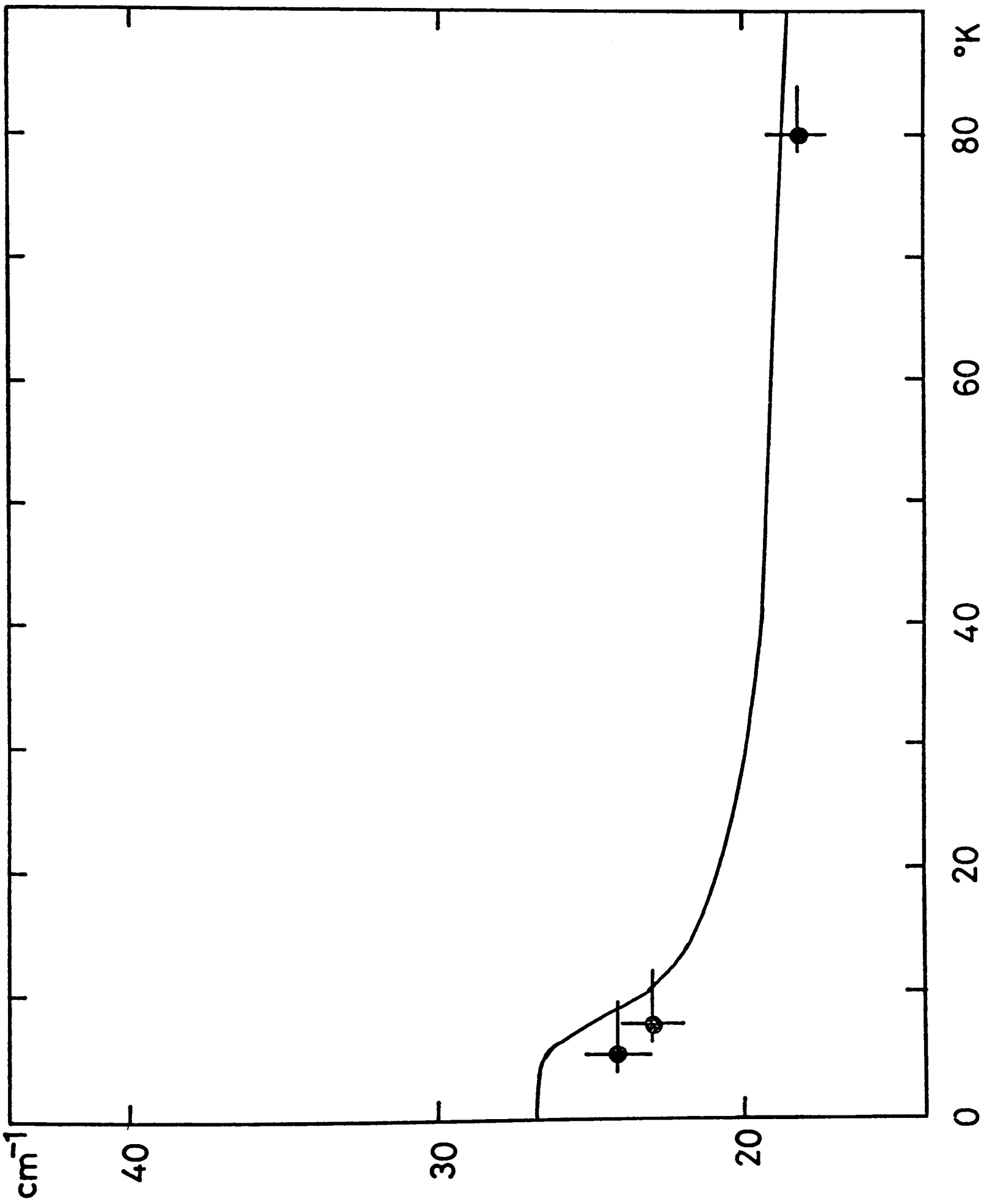
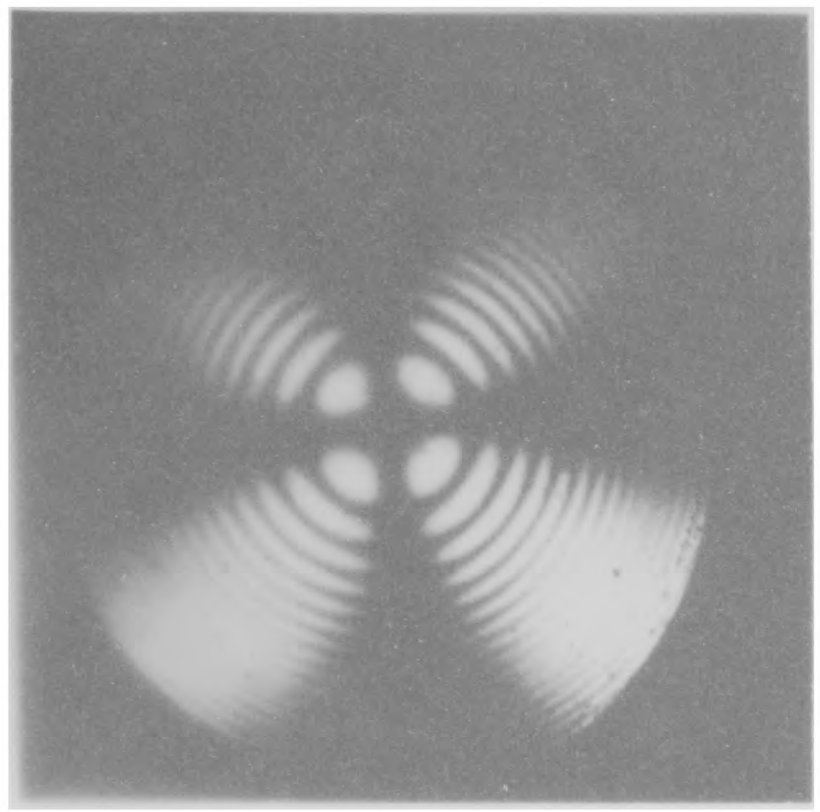


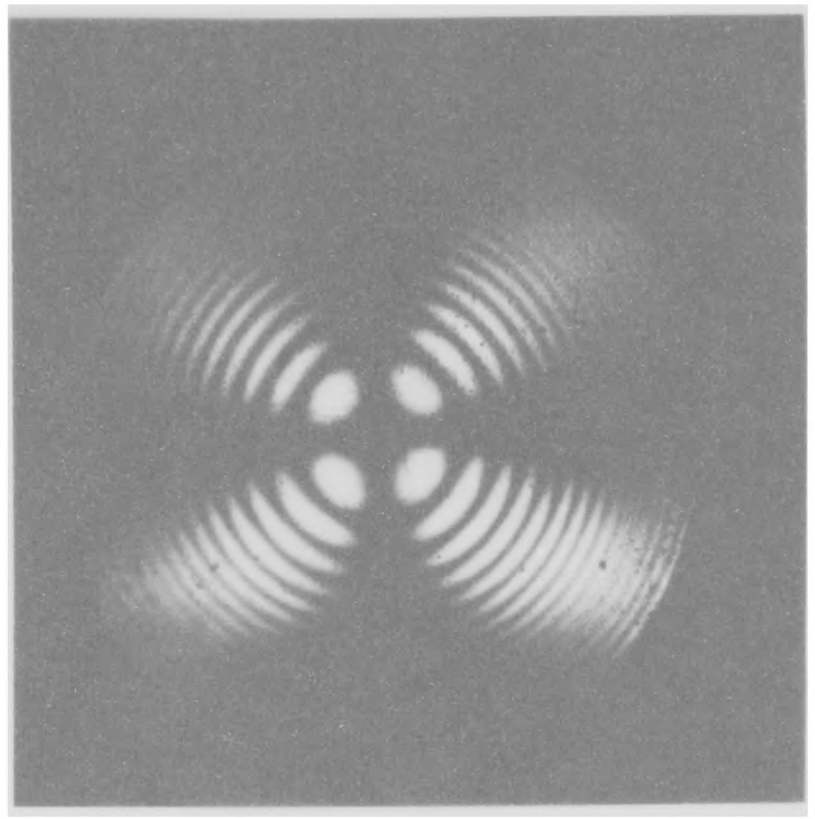
Fig. 5.16.

c = 0.365. Temperature dependance of the lowest electronic Raman mode. Solid curve given by MFA (section 5.6).

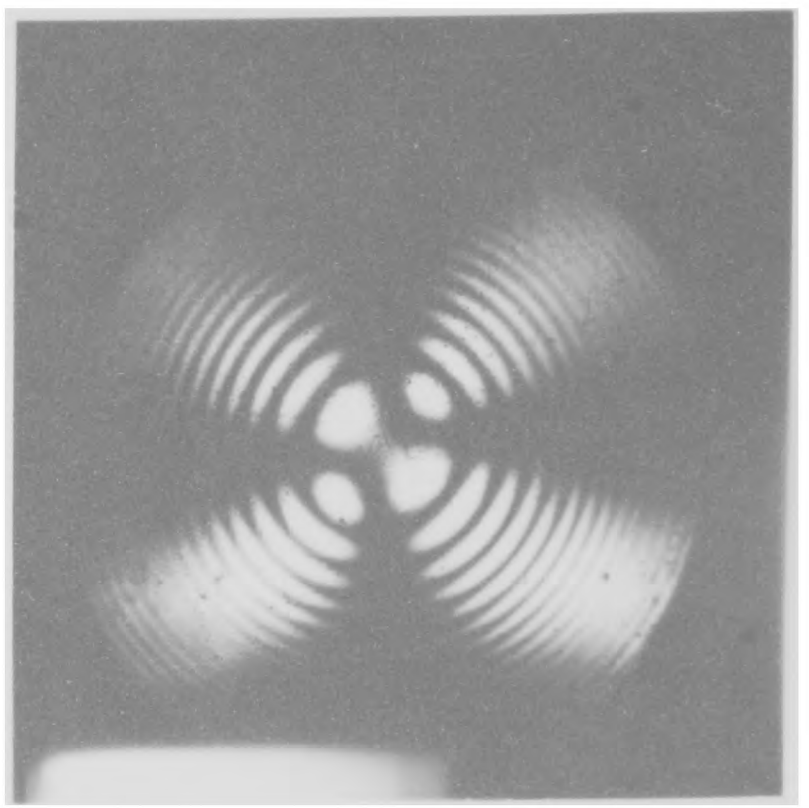




18 5 °K



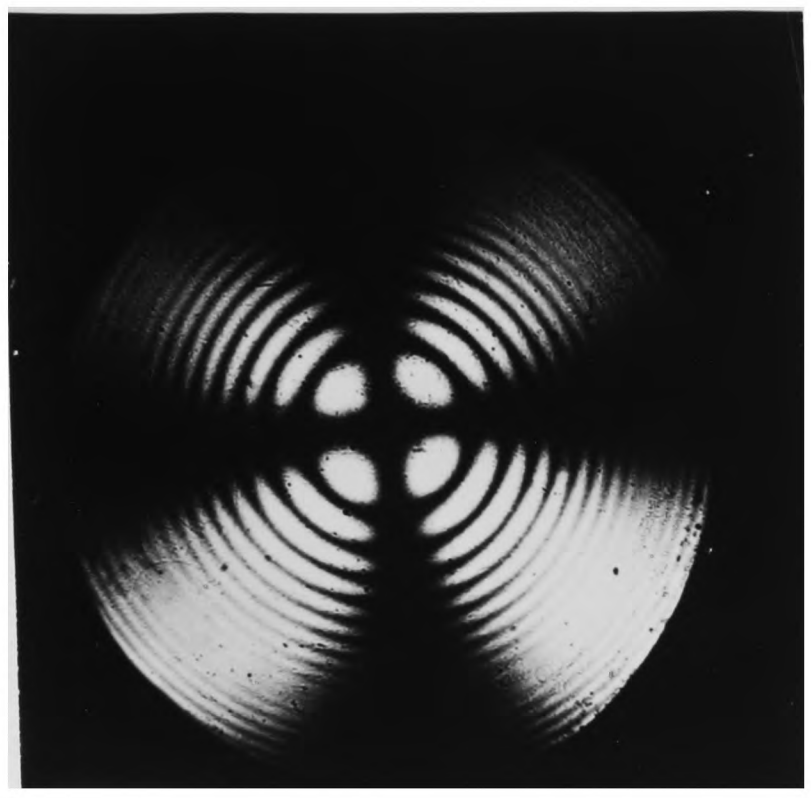
9.0 °K



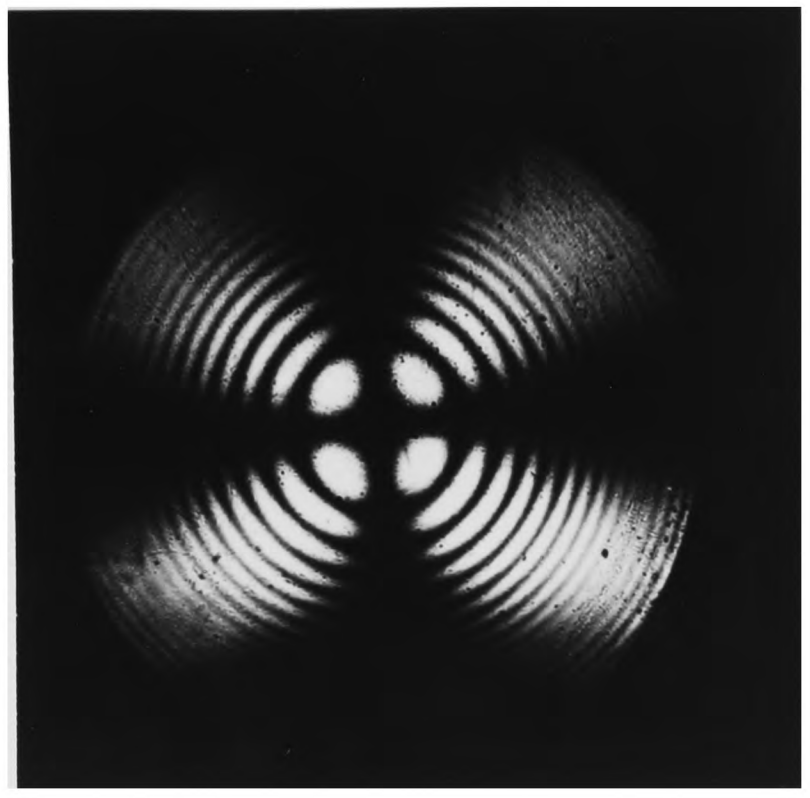
8.3 °K

Interference patterns obtained at 18.5, 9.0, 8.3°K using convergent polarized light for c = 0.365.

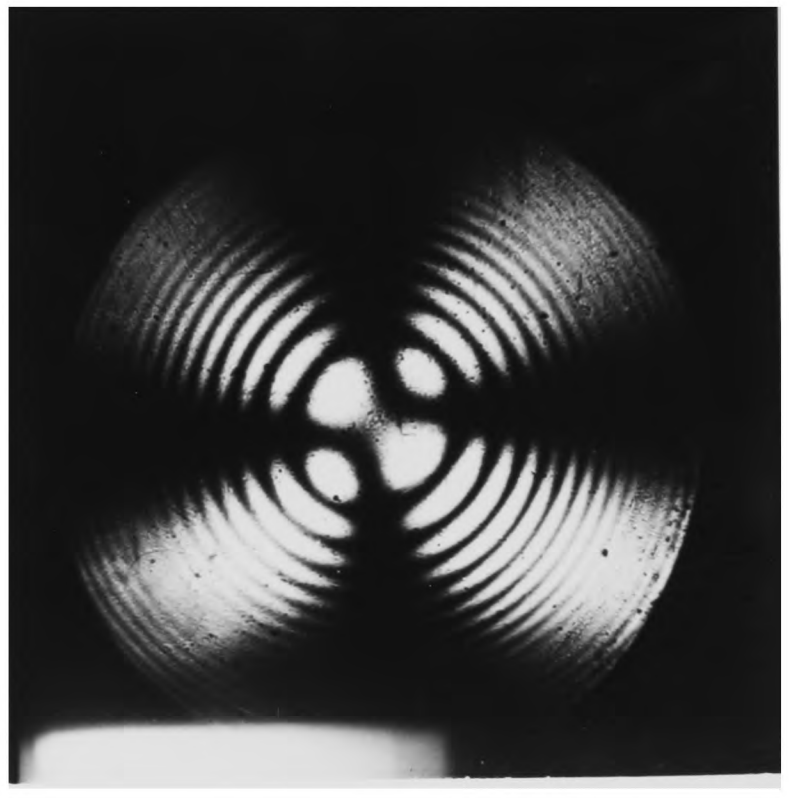
Fig. 5.17(a).



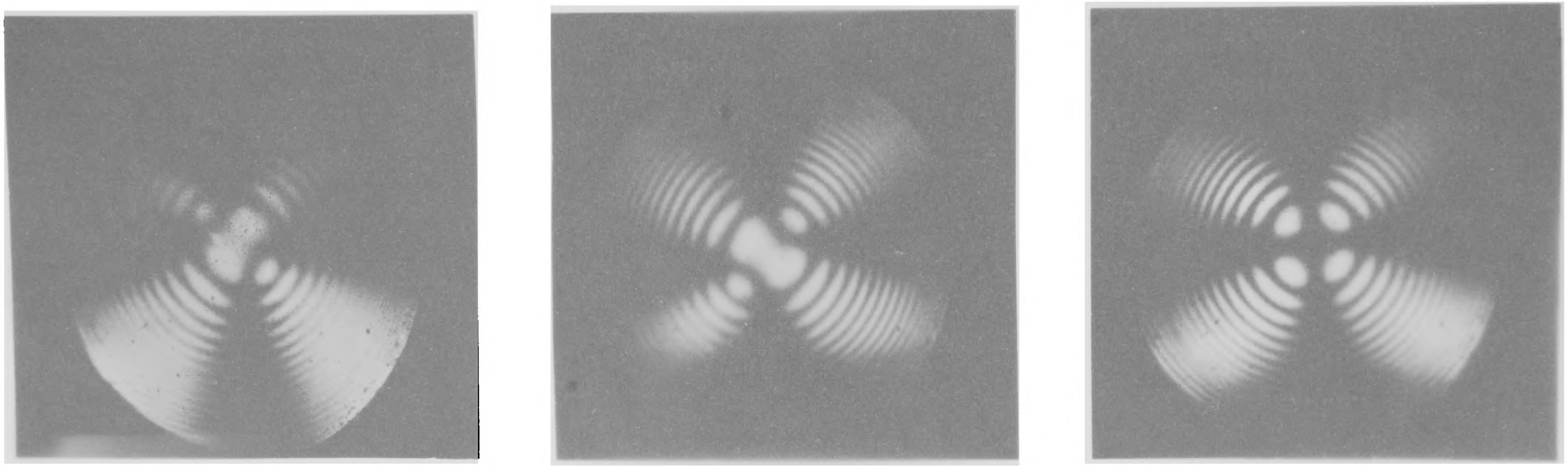
18.5 °K



9.0 °K

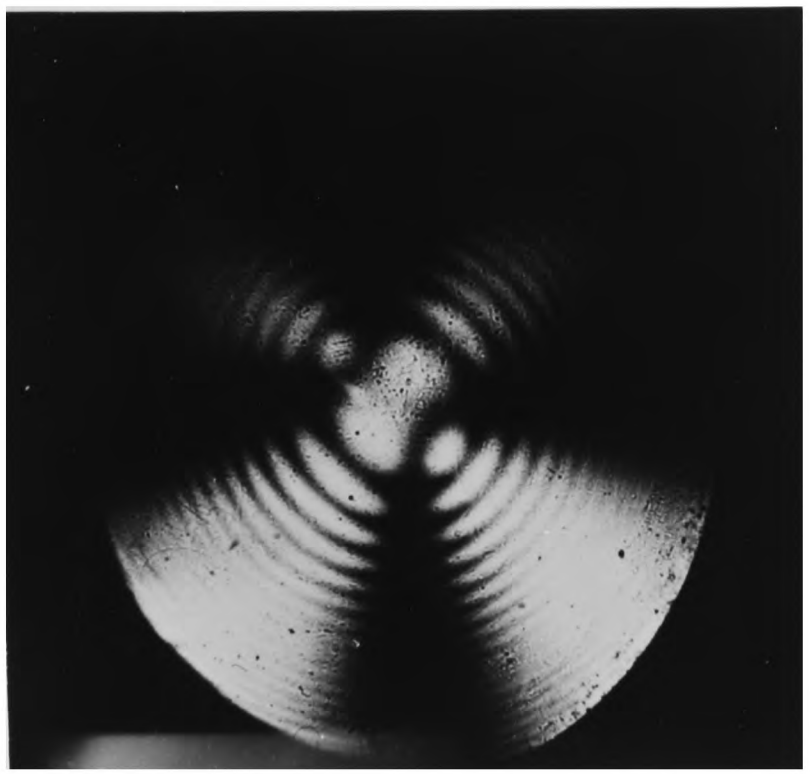


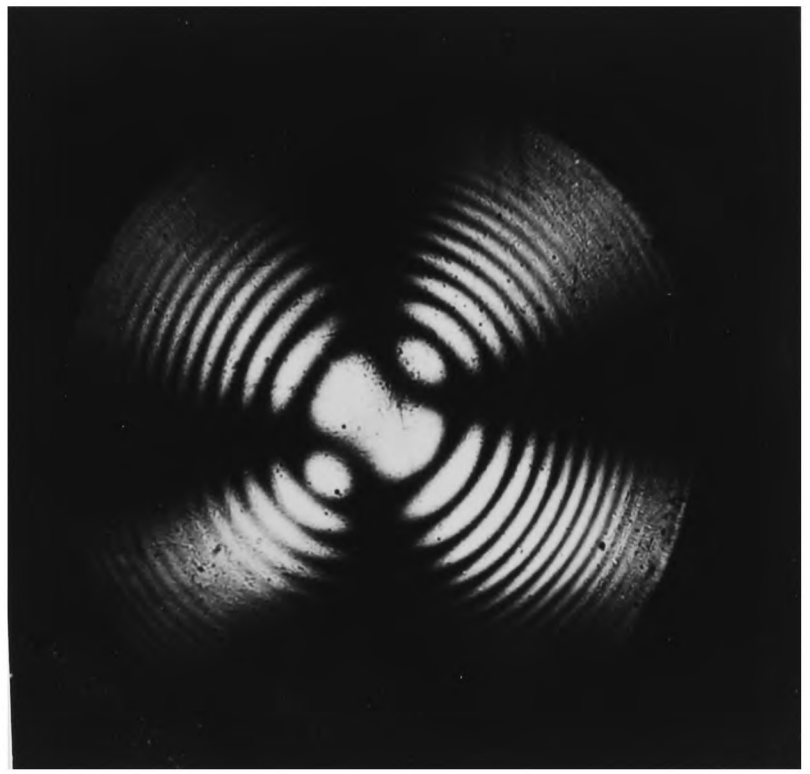
8.3 °K



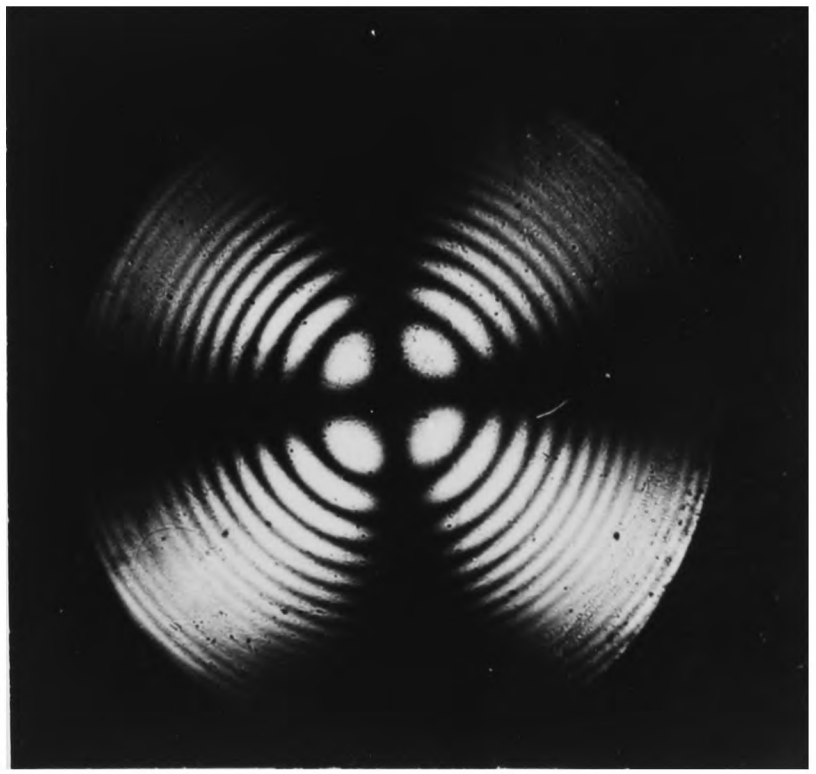
Interference patterns obtained at 4.2°K (two different regions of crystal) and 2.16°K using convergent polarized light for c = 0.365.

Fig. 5.17(b).





4.2 °K



2.16 °K

These indicate the existence of two different ty`es of orthorhombic domain with principal axes in the basal plane parallel to the x' and y' axes defined in Fig. 5.1. The transitions from biaxial to uniaxial interference patterns took place smoothly indicating that the phase transitions are of second order.

Several crystals from the same batch were examined in this way and all showed the same behaviour. The transition temperatures were reproducible within the experimental errors.

In contrast to the Raman measurements there was very little local heating of the sample and transition temperatures could be determined with good accuracy (see crosses in Fig. 5.5) For the c = 0.425 sample the transition temperature agreed with that obtained from the Raman measurements. The two transition temperatures for the c = 0.365 crystal were $8.5 \pm 0.5^{\circ}K$ and $2.3 \pm 0.1^{\circ}K$. Due to the small splitting of the E_g phonon in this crystal at $5^{\circ}K$ the transition temperatures could not be determined with any accuracy from the Raman spectra. No phase transitions could be detected down to $2^{\circ}K$ in the c = 0.320 and 0.300 samples, in agreement with the Raman data.

A short account of some of these results is in the course of publication (Harley et al 1973 (b).)

5.6 Comparison of Theory and Experiment

The theoretical work by Elliott et al (1972) showed that the molecular field approximation (MFA) gave a good account of the behaviour of pure $TbVO_4$. The overall agreement between the experimental results and the predictions of the MFA shows that this theory still gives an excellent account of the effects in the mixed crystals of $Tb_cGd_{1-c}VO_4$. This section will discuss the correlation between theory and experiment in detail.

In Fig. 5.5 the solid line was calculated from equation (5.4), where λ was replaced by $c\lambda_o$. The energy level separation, ϵ, was taken as $9cm^{-1}$, equal to half the singlet level separation at high temperature while λ_o was put equal to $24.3cm^{-1}$ in order to fit the observed transition temperature in pure $TbVO_4$ (34^oK). This is in good agreement with the value of $25.6cm^{-1}$ obtained from the low temperature limit of the electronic doublet separation. The MFA predicts that two transitions should occur for $0.310 < c < 0.380$, and this effect has been observed for $c = 0.365$. The experimentally determined transition temperatures agree quite closely with the theory. They are on the whole slightly less than the predicted values. This is to be expected, as the MFA essentially assumes an interaction of infinite range.

It might be argued that the two phase transitions that occurred in the $c = 0.365$ crystal were due in some way to magnetic ordering of the Gd^{3+} ions. This is unlikely to be the case, because if the Gd^{3+} ions order magnetically along

c - axis (which would be expected at a temperature no greater than 63.5% of 2.55°K, i.e. 1.63°K) there will be very little effect on the Tb^{3+} ions, since the c - axis magnetic splitting factor is almost zero, (Becker et al 1972). If, on the other hand, there was an interaction which caused the Gd^{3+} ions to order in the plane normal to the c - axis this would actually tend to assist the Jahn-Teller interaction , and would certainly not be expected to cause the distortion to vanish below 2.3°K (Harley et al (1973 b)). Pure $TbVO_4$ does not order above 1°K.

In Figs. 5.6 - 5.9 the solid lines show the theoretical variation of the E_g phonon mode splittings as a function of temperature for several values of c. This splitting was assumed to be proportional to the strain in the crystal, i.e. proportional to $c\langle\sigma^2\rangle$. Values of $\langle\sigma^2\rangle$ were calculated self-consistently from equation (5.5), using the values of ϵ and λ_o given above. The curves were normalized at 5°K using the experimentally determined values of the E_g phonon splitting in pure $TbVO_4$. These splittings were taken as $6.8cm^{-1}$ for the E_g^{I} phonon and $8.8cm^{-1}$ for E_g^{III}, from Elliott et al (1972).

Note that the theory predicts a <u>decrease</u> in the splitting of these phonons in the mixed crystals as the temperature is lowered below about 5°K due to thermal depopulation of the electronic doublet. The effect in $Tb_cGd_{1-c}VO_4$ becomes more pronounced as c is reduced, until for the c = 0.365 crystal the splitting becomes zero at a finite

temperature. A slight reduction in the splitting was observed experimentally for c = 0.725 and c = 0.520 on cooling from $5^{\circ}K$ to $2^{\circ}K$. In the c = 0.425 sample the splitting remained constant within the experimental error. This was probably due to increased local heating in this sample. Varying amounts of flux included in the crystals made the local heating sample dependant.

At low temperatures the agreement between the experimental and theoretical phonon splitting is good, but gets worse near the transition temperature. In this region the theoretical lines (Figs. 5.6 - 5.9) have a very steep slope, and a small difference between the experimental and theoretical transition temperature leads to a large discrepancy in the actual and predicted splittings. The E_g phonon splittings at $5^{\circ}K$ are plotted as a function of c in Figs. 5.11 and 5.12, and show quite clearly how accurately the MFA predicts the observed behaviour. The MFA should represent an upper limit on these parameters, as it assumes an infinite range interaction, while in reality the interaction must be of finite range.

For the sample with the two phase transitions the E_g mode splitting at $5^{\circ}K$ was quite close to the theoretical prediction, but as the maximum splitting was only just resolvable it was not possible to make any realistic comparison at other temperatures. The two transition temperatures for this crystal determined by the birefringence experiments agreed with the MFA prediction within the experimental error.

The birefringence experiments also showed that the distortion in the mixed crystals was still along the x' and y' axes, as in pure $TbVO_4$, (see Figs. 5.17(a) and (b).)

While the MFA predicts that the $A_1 \rightarrow B_1$ (Fig. 5.3) electronic transition should have a constant energy 2ϵ above T_D (see section 5.2) experimental results show that it decreases slowly with temperature, (Figs. 5.13 - 5.16). The solid lines in these figures were calculated from the coupled mode theory at $\underline{k} = 0$, equations (5.8) and (5.9). From equation (5.9) it can be seen that J(0) must be negative for the frequency to decrease with temperature. This term J(0) was taken as $-30cm^{-1}$ (from Elliott et al 1972) and represents the difference between the optic and acoustic mode coupling. Thus $J(0) < 0$ implies that the acoustic mode coupling is still larger in the mixed crystals, as in pure $TbVO_4$. The results of the coupled mode theory give quite good agreement with the experimental results. The positions of the two singlet levels at high temperature were found from the Raman spectra to be independant of the Gd concentration (within $\pm$ $1cm^{-1}$).

The coupled mode theory for the c = 0.365 crystal, (solid line, Fig. 5.16) shows that even below the second phase transition, when the sample has reverted to tetragonal symmetry, this electronic transition does not decrease in frequency. In the low temperature tetragonal phase, $\langle\sigma^z\rangle = 0$ and the frequency of the electronic transition is given by the first equation (5.9). However, at low temperatures the

approximation that was used before above T_D that

$$\langle \sigma^x \rangle = \text{Tanh} \frac{\epsilon}{2kT} \simeq \frac{\epsilon}{2kT} \qquad (5.13)$$

is no longer valid. At low temperatures Tanh $\frac{\epsilon}{2KT}$ increases as T decreases, reaching a limiting value given by

$$\lim_{T \to 0} \langle \sigma^x \rangle = \lim_{T \to 0} \text{Tanh} \left(\frac{\epsilon}{2KT} \right) = 1 \qquad (5.14)$$

No decrease in frequency was observed experimentally. As the transition was of low intensity in this crystal a relatively high laser power had to be used and local heating made the temperature measurements imprecise (Fig. 5.16).

The widths of the electronic excitations were almost independant of c. For c = 0.52 the width above T_D was still only about $10cm^{-1}$, giving an estimate of approximately 10 for the number of neighbours, (from equation (5.12).)

In conclusion, these studies of $Tb_cGd_{1-c}VO_4$ have shown that the MFA continues to provide an excellent description of the behaviour of the systems, and confirms the existence of the unique double phase transitions predicted by Elliott et al (1972). This constitutes further evidence that the Jahn-Teller interaction between Tb^{3+} ions is long range.

More information about the system might be obtained from a study of the variation of the elastic constants with temperature through the double phase transition. The work

of Elliott et al (1972) predicted an acoustic anomaly in the elastic constant C_{66} of pure $TbVO_4$ at the transition temperature, and this was subsequently observed by ultrasonic and Brillouin scattering methods (Sandercock et al 1972). Although no detailed calculations have been made it seems likely that two acoustic anomalies will be seen, one at each transition temperature. These experiments should give a better estimate of the acoustic mode coupling in the mixed crystals.

CHAPTER SIX

EXPERIMENTS WITH

MANGANESE ZINC FLUORIDE

6.1 Introduction

Both MnF_2 and ZnF_2 have the rutile structure D_{4h}^{14}, with two formula units per unit cell (Wyckoff 1960). While ZnF_2 is non-magnetic, MnF_2 has been found to order anti-ferromagnetically below $67^{o}K$. (Baker, Lourens and Stevenson 1961).

The two-magnon spectrum of pure MnF_2 has been studied both by infra-red absorption (Allen, Loudon and Richards 1966) and by Raman scattering (Fleury and Loudon 1968). They found that the second order spectra were remarkably strong in comparison with the one-magnon spectrum. In a concentrated crystal the optical selection rules require the simultaneous creation of two magnons with wavevectors $\underline{q}$ and $-\underline{q}$. Since the density of states of anti-ferromagnets is strongly peaked at the maximum frequency (which occur with $\underline{q}$ on the Brillouin zone boundary) the infra-red and Raman spectra also show a sharp peak near twice the maximum spin-wave frequency. The localized magnons of Co^{2+} in MnF_2 have been observed by Raman scattering by Moch, Gosso and Dugautier (1970).

Until recently there has been little experimental evidence of the nature of spin excitations in magnetic crystals diluted with non-magnetic constituents. Such crystals show effects which are different from those found in mixed magnetic systems (Cowley and Buyers 1972). It is knownthat as the concentration c of non-magnetic atoms increases the transition temperature T_c falls. At low c this fall off varies linearly with c. In systems dominated by short range exchange

interactions T_c falls to zero at a finite critical concentration c_0. Dilution can be thought of as giving rise to a weakening of the co-operative forces comparable with that caused by thermal disorder.

MnF_2 diluted with Zn provided a good system in which to study dilution effects. The magnetic structure was well known and relatively simple, and the similar sizes of Mn and Zn enabled good quality mixed crystals to be grown for the whole concentration range. Baker et al (1961) first studied the dependance of T_c on c using nuclear magnetic resonance. They found $c_0 \simeq 0.75$ compared with the best estimate of 0.76 from percolation theory (Sykes and Essam 1964; Elliott and Heap 1962). Recently Coombs et al (private communication) examined the spin-wave spectrum of this mixed system using inelastic neutron scattering techniques. They found that anti-ferromagnetic order, indicated by the presence of Bragg peaks, disappeared for $c = 0.72 \pm 0.005$. Their results also showed that the one-magnon peaks shift and broaden with increasing dilution. So far the one-magnon excitations have not been observed by Raman scattering.

Crystals of $(Mn,Zn)F_2$ were studied optically by Misetich et al (1968) and by Greene et al (1968). More recently infra-red and Raman studies have been carried out by Mitlehner et al (1971), for $c < 0.1$. The experiments described in this thesis extend across the whole concentration range, and are discussed in section 6.3.

Sections 6.2 and 6.3 give an account of the experiments that were carried out on $(Mn,Zn)F_2$. A review of several

theories of the two-magnon excitations in this system is given in sections 6.5 and 6.6 and a comparison of experiment and theory given in 6.7. The Raman-active phonons exhibited some unusual behaviour and these results are described in section 6.8.

6.2 Experimental

The single crystals of good optical quality $Mn_{(1-c)}Zn_cF_2$ with c covering the range 0 to 1 were grown by Mr. J. Storey in the Clarendon Laboratory, using the Kyropolous method. Reagent grade MnF_2 was found to be adequately pure for the purpose, but the commercially available ZnF_2 required zone refining before use. The crystals were oriented by X-ray methods and cut into cubes with (100) faces, of side approximately 3mm. The faces were polished with diamond paste before use, and the tetragonal axis located by observing the interference patterns of the crystal viewed between crossed polarizers.

The relative concentration (mole fraction) of the Mn and Zn was measured for all crystals by X-ray fluorescence methods. A one gram powder sample was taken for each of the concentrations. Each sample was mixed with a small amount of "Araldite" and spread uniformly over a perspex disc about 3cm in diameter. The relative intensities of the K_β lines of the Mn and Zn were then measured. The X-ray fluorescence spectrometer was calibrated using similar samples made from

known mixtures of MnF_2 and ZnF_2. The crystals were shown to be good solutions of MnF_2 and ZnF_2 by checking with an X-ray diffractometer. No lines due to MnF_2 or ZnF_2 alone could be detected in the mixed crystal spectra. The X-ray diffraction lines corresponded to a gradual change of lattice parameters with c on going from pure MnF_2 to pure ZnF_2.

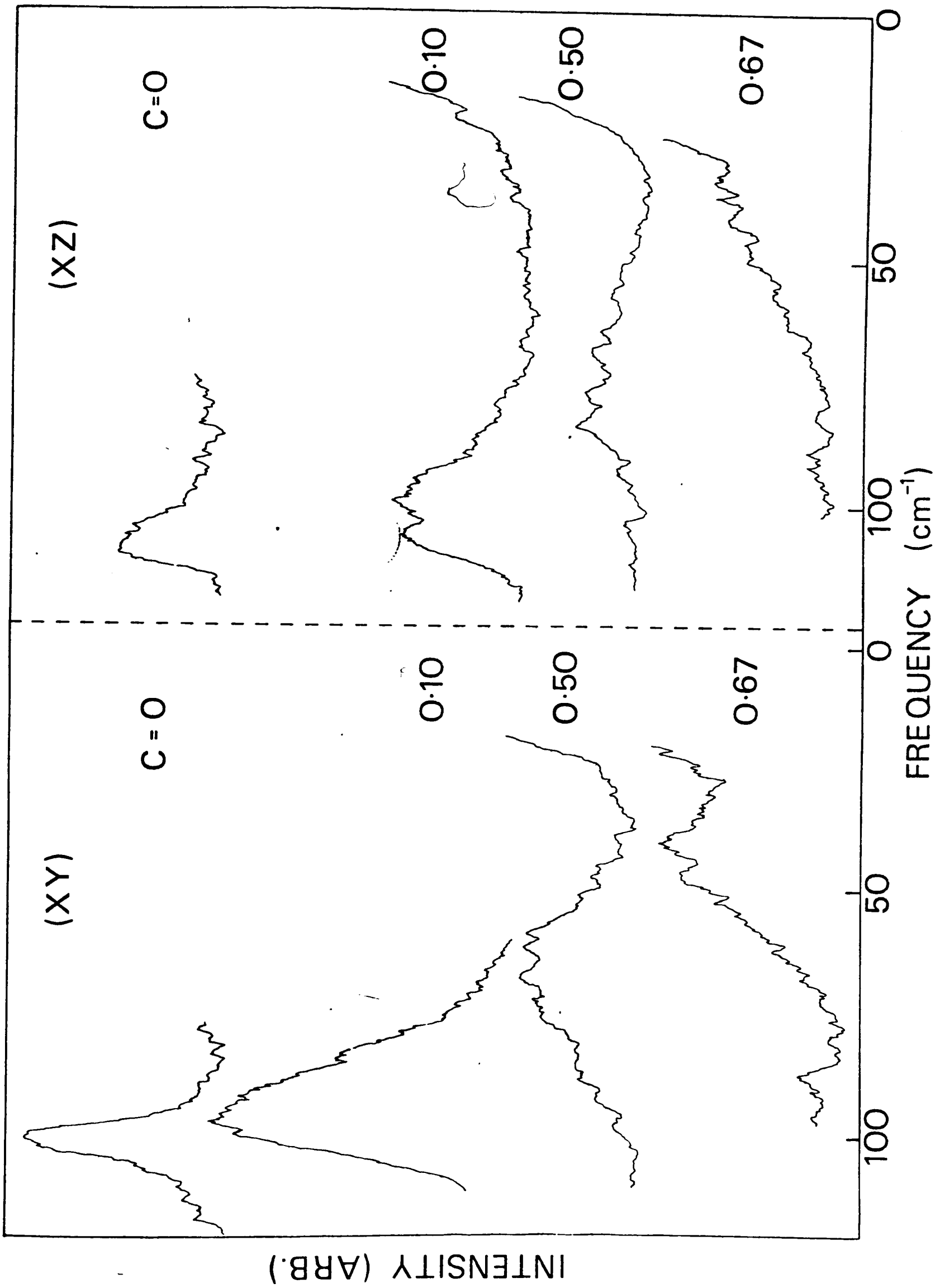
The Raman measurements were made on crystals immersed in superfluid helium at $1.7^{o}K$. Spectra were obtained using 1W of 488.0nm linearly polarized light from an argon ion laser. Even with such a high laser power, the two-magnon spectra were still very weak, ($\sim$25 counts $sec.^{-1}$) in the mixed crystals. To obtain a reasonable signal-to-noise ratio a time constant of 25 sec. was used on the ratemeter. The resolution of the spectra was about $3cm^{-1}$.

It was estimated that the local heating due to the laser did not cause more than a $5^{o}K$ rise in temperature of the illuminated crystal region.

6.3 The Raman Spectra

The results of these experiments on $Mn_{(1-c)}Zn_cF_2$ have been published previously (see Buchanan et al 1972). Two-magnon Raman lines were recorded only in the xy and xz polarizations, where z coincides with the c axis of the tetragonal structure and x and y are in the basal plane, parallel to the edges of the tetragonal cation sublattice. Some of the spectra obtained are shown in Fig. 6.1. It is seen that

Fig. 6.1.

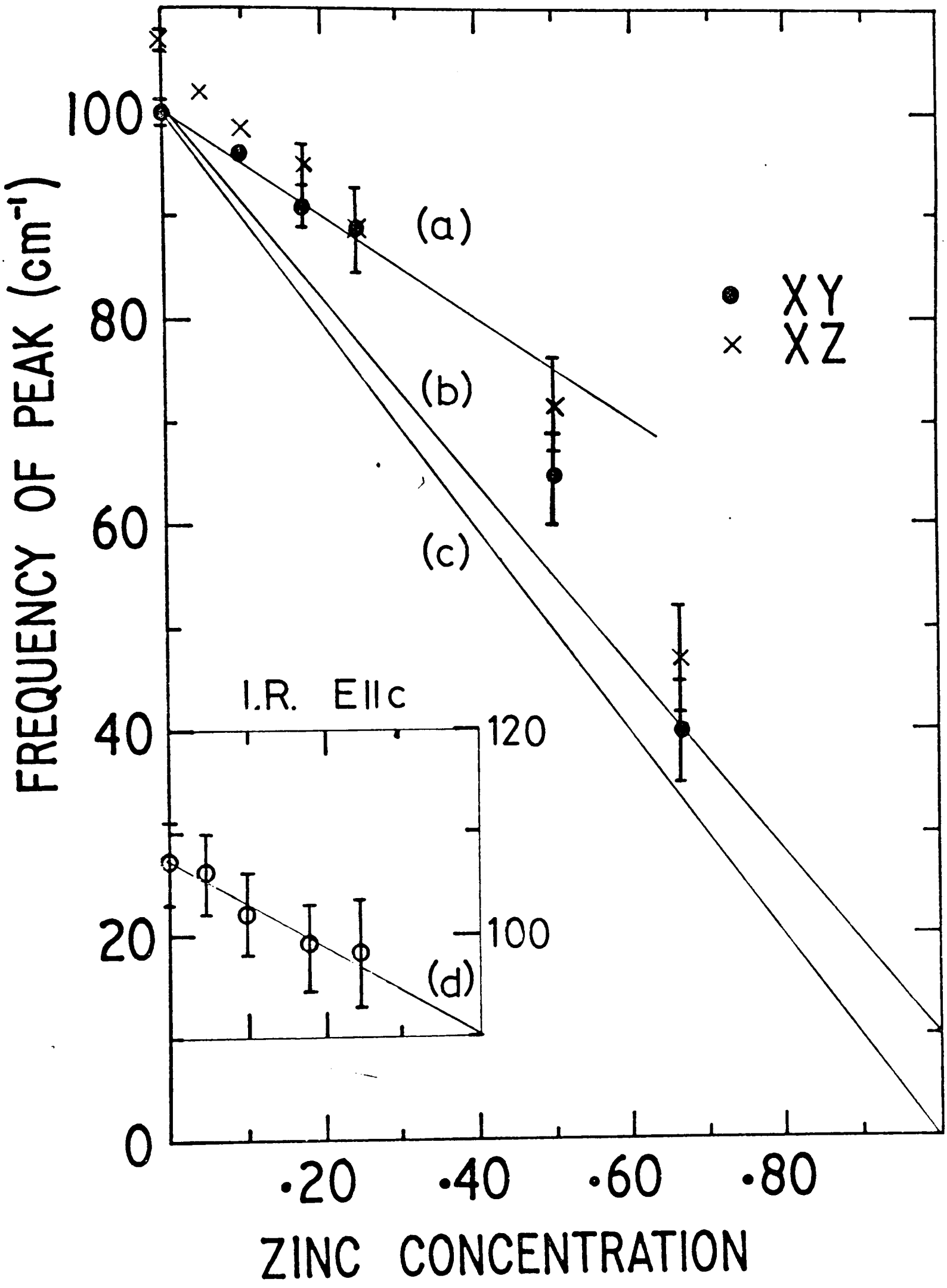


Two-magnon Raman scattering with xy and xz polarization in $(Mn_{1-c}Zn_c)F_2$ crystals at $5^{\circ}K$ for various values of c.

the lineshapes for pure MnF_2 are asymmetrical, especially in xy polarization. For a finite concentration c of zinc the peaks move to lower energy. They are broadened and the asymmetry is reduced; for c = 0.5 the bands are fairly symmetrical. The two-magnon peak is observable up to $c \simeq 0.7$ (see Fig. 6.1), but at higher zinc concentrations it was difficult to distinguish unambiguously the magnetic scattering from the background and Rayleigh scattering. These spectra for pure MnF_2 agree with previously published results (see e.g. Fleury 1971).

The behaviour of the peak positions of the two-magnon bands is shown in Fig. 6.2. Line "a" gives the slope of the experimental points for xy polarization with $c < 0.25$. The two lines b and c are theoretical and are discussed in sections 6.5 and 6.6. The peak positions of the two-magnon Raman lines decrease linearly with c up to $c \simeq 0.25$ and thereafter decrease more rapidly. At c = 0.5 the transition temperature T_c is $\sim 20^{\circ}K$, (Baker, Lourens and Stevenson 1961) so that up to this concentration the temperature of the measurements may be regarded as effectively $0^{\circ}K$. (As stated above, it was estimated that the heating effect of the laser did not raise the temperature of the crystals by more than $5^{\circ}K$). For larger values of c the actual temperature of measurement was an appreciable fraction of T_c and therefore the measured peak position for c = 0.67 (Fig. 6.2) was somewhat lower in energy than values appropriate to $0^{\circ}K$. The linear portions of the experimental curves in Fig. 6.2 extrapolate to finite energies

Fig. 6.2.



Peak positions of two-magnon Raman bands at $5^{\circ}K$. Inset gives peak position of two-magnon I.R. absorption at $1.7^{\circ}K$ for $\epsilon \parallel \underline{c}$ and $c < 0.25$. See text for discussion.

for c = 1 and have slopes $d\omega/dc = -45 \pm 10$ and $-62 \pm 12 cm^{-1}$ per unit Zn concentration for xy and xz respectively.

The widths of the two-magnon lines showed a rapid increase with increasing zinc concentration for low c and at c = 0.1 the widths were about twice those observed in pure MnF_2. The rate of increase fell off at higher c. Up to $c \simeq 0.5$ the two-magnon peaks were separated from the Rayleigh line, and the full widths at half height were measured directly. However, for $c \gtrsim 0.5$ the magnetic scattering overlapped the Rayleigh line, as can be seen in Fig. 6.1 and the widths were estimated from the high energy part of the band. It was assumed that the line had a symmetric shape.

It was not possible to measure accurately the integrated intensity of the magnon lines as a function of c because of the difficulty in allowing for the background scattering due to crystal imperfections and impurity induced phonon scattering. For this reason the intensities in Fig. 6.1 may not be compared for different value of c, although for a given c the xy and xz intensities may be directly compared. The uncertainty in the background also prevented a moment analysis of the spectra being made, as was done for pure MnF_2 as a function of temperature by Brya and Richards (1972). This was the reason for plotting peak positions rather than first moments in Fig. 6.2. The crystals used by Brya and Richards appear to have been of better optical quality so that the magnon scattering could be distinguished more easily from the background (Richards 1973

private communication). $(Mn,Zn)F_2$ crystals absorb strongly in the vicinity of the 514.5nm argon laser line (Greene et al 1968) and it was therefore not possible to use an iodine cell to improve the signal-to-noise ratio. The use of an iodine cell is described by Devlin et al (1971). (Iodine vapour has a narrow absorption band at about 514.5nm to which the laser can be tuned. If a cell containing iodine vapour is placed in the scattered light beam, the Rayleigh component is partly absorbed, increasing the signal-to-noise ratio for low energy excitations). Thus it was impossible to investigate the interesting but relatively weak magnetic scattering in the vicinity of c_0 , the critical concentration.

The $(Mn,Zn)F_2$ spectra described in this thesis are significantly different from those obtained by Mitlehner et al (1971). They measured the two-magnon Raman peak positions in the range $0 < c < 0.1$ and found $d\omega/dc \simeq -170$ cm $^{-1}$ per unit Zn concentration for xy polarization; their measured linewidths are also considerably greater than those shown in Fig. 6.5 in this range. This disagreement appeared to be due to an error in the analyses of the mixed crystals by Mitlehner et al (private communication).

6.4 Raman scattering from $(Mn,Zn)F_2$

The Hamiltonian describing the spin states of $(Mn,Zn)F_2$ is, to a good approximation, just the Heinsenberg

interaction between Mn ions with S = $^5/_2$. The dominant interaction is the exchange interaction between a Mn ion and its eight magnetic neighbours in positions $\delta = \frac{1}{2}(a,a,1)$ (Nicotin et al 1969). There is a small anisotropic interaction of the dipole type and a negligible single-ion anisotropy, but both of these have been neglected in the theories reviewed here. The Hamiltonian for an antiferromagnet given in Chapter 2. then simplifies to

$$\mathcal{H} = \sum_{\underline{l},\underline{\delta}} J\underline{S}(\underline{l}).\underline{S}(\underline{l}+\underline{\delta}) \qquad (6.1)$$

where the sum is over the lattice points, $\underline{l}$, $\underline{l}+\underline{\delta}$ occupied by Mn ions. For MnF_2, the spin waves are given by

$$\hbar\omega(\underline{q}) = \left[A^2 - B^2(\underline{q})\right]^{\frac{1}{2}} \qquad (6.2)$$

where $B(\underline{q}) = 2JS\sum_{\delta} \exp.\ (i\underline{k}.\underline{\delta})$
and $A = B(0) = 2zJS$ (6.3)

where z is the number of nearest neighbours (8 for the rutile structure).

The two-magnon lineshape is determined by the magnon density of states, which is large near the zone boundary (Fleury and Loudon 1968). Zone boundary magnons have an energy A, which also corresponds to the energy of spin reversal in the Ising model. The Ising Hamiltonian is given by

$$\mathcal{H}' = \sum_{\underline{l},\underline{\delta}} JS_z(\underline{l})S_z(\underline{l}+\underline{\delta}) \qquad (6.4)$$

This approximation is used in section 6.6.

Fleury and Loudon (1968) showed that the magnon pairs observed in two-magnon Raman scattering in MnF_2 had even parity and $S_z = 0$. Only even parity excitations are ever produced in Raman scattering, and the magnetic field independence of the line showed that $S_z = 0$. While equation (6.2) predicts that magnons have a constant frequency over the zone boundary, experimental results give frequencies of 50 and 55cm^{-1} at the X and Z points respectively, in the low temperature limit (Okazaki et al 1964). This can be accounted for by including a small ferromagnetic exchange between neighbours on the same sublattice (Fleury and Loudon 1968).

The mechanism for the two-magnon Raman scattering in MnF_2 is the exchange scattering discussed in Chapter 2. Following Fleury and Loudon the interaction Hamiltonian can be written (Buchanan et al 1972).

$$\mathcal{H}^{R} = \sum_{\alpha,\beta} E_\alpha E'_\beta B_{\alpha\beta}(\delta)\underline{S}(\underline{1}).S(\underline{1}+\underline{\delta}) \equiv \sum_{\alpha,\beta} E_\alpha R_{\alpha\beta} E'_\beta \qquad (6.5)$$

where E_α and E'_β are the components of the electric field of the incoming and outgoing photons. For the xy and xz polarizations in which the magnons were observed

$$\left.\begin{aligned} B_{xy}(\underline{\delta}) = B_{yx}(\underline{\delta}) &= B_3 \sigma_{\delta}^{x} \sigma_{\delta}^{y} \\ B_{xz}(\underline{\delta}) = B_{zx}(\underline{\delta}) &= B_4 \sigma_{\delta}^{x} \sigma_{\delta}^{z} \end{aligned}\right\} \qquad (6.6)$$

where $\sigma_{\underline{\delta}}^{\alpha}$ = sign ($\underline{\delta}^{\alpha}$) i.e. the sign of component in the α direction.

The two-magnon Raman scattering is characterized by an extinction coefficient given by Fleury and Loudon as

$$k_{\alpha\beta\alpha\beta} = K\sum_{ij} p_i |\langle i|R_{\alpha\beta}|j\rangle|^2 \delta(E_i - E_j + \hbar\omega_r - \hbar\omega_r') \quad (6.7)$$

where ω_r, ω_r' are the frequencies of the incident and scattered light and p_i is the thermal probability of finding the system in the state $\langle i|$. It is assumed that the temperature is sufficiently low so that $\langle i|$ is the magnon ground state.

The transverse part of the Hamiltonian 6.5 which may be written as $\frac{1}{2}(S^+S^- + S^-S^+)$ is responsible for the main part of the two-magnon scattering at low temperature. By expanding in spin-wave operators Fleury and Loudon obtained Raman scattering cross-section for non-interacting spin-waves given by

$$64KS^2B_3^2 \sum_{\underline{q}} \left(\frac{A}{\hbar\omega(\underline{q})}\right)^2 \sin^2(\tfrac{1}{2}aq_x)\sin^2(\tfrac{1}{2}aq_y)\cos^2(\tfrac{1}{2}cq_z)\,\delta(\omega_r - \omega_r' - 2\omega(\underline{q})) \quad (6.8a)$$

for xy polarization and

$$64KS^2B_4^2 \left(\frac{A}{\hbar\omega(\underline{q})}\right)^2 \sin^2(\tfrac{1}{2}aq_x)\cos^2(\tfrac{1}{2}aq_y)\sin^2(\tfrac{1}{2}cq_z)\,\delta(\omega_r - \omega_r' - 2\omega(\underline{q})) \quad (6.8b)$$

for xz polarization. This corresponds to the creation of pairs of spin-waves with wavevectors $\underline{q}$ and $-\underline{q}$. The trigonometric factors in equations (6.8a) and (6.8b) provide the weightings of the magnon density of states which emphasize particular regions in the Brillouin zone and thus determine

the shape of the spectrum. Thus the magnon pairs observed in xy polarization originate from the M point in the Brillouin zone, and those in xz from the R point. Magnons in each pair are generated on opposite sublattices. Although Elliott and Thorpe (1969) showed that final state interaction between the magnons created close together shifted the two-magnon peak to lower energy by an amount 2J, this is negligible compared to A in MnF_2 and has little effect in the mixed crystals.

6.5 Moment Calculations

In this and the next section two different theories of the spin waves in $(Mn,Zn)F_2$ alloys are reviewed, and their predictions compared with our experimental results in section 6.7. The moment calculations are due to Elliott and Saville, and the cluster model was developed by Buyers, (See Buchanan et al 1972).

The moments of the Raman spectrum were calculated from the following relations:-

$$\hbar\langle\omega\rangle = \langle[\mathcal{H}, R_{\alpha\beta}]R_{\alpha\beta}\rangle / \langle R_{\alpha\beta}R_{\alpha\beta}\rangle$$

$$\hbar^2\langle\omega^2\rangle = \langle[\mathcal{H}, R_{\alpha\beta}][\mathcal{H}, R_{\alpha\beta}]\rangle / \langle R_{\alpha\beta}R_{\alpha\beta}\rangle \qquad (6.9)$$

$$\hbar^3\langle\omega^3\rangle = \langle[\mathcal{H}, [\mathcal{H}, R_{\alpha\beta}]][\mathcal{H}, R_{\alpha\beta}]\rangle / \langle R_{\alpha\beta}R_{\alpha\beta}\rangle$$

where $\langle\omega\rangle$ denotes the mean frequency shift $\langle\omega_r - \omega_{r'}\rangle$.

The problem was to evaluate the commutators of the Heisenberg Hamiltonian 6.1 and the interaction 6.5 , and then calculate the thermal averages. The process rapidly increased in complexity with higher order moments, so that only the first few could be found, although in principle the method was applicable to any order.

The thermal averages were calculated in the low temperature approximation, i.e. in the ground state. This was approximated by using the Néel ground state, in which all the spins aligned anti-parallel along the c - axis. Correlations between spins on different sites were also ignored.

The total intensity I of the scattered light was obtained by integrating the extinction coefficient, equation (6.7) over all frequencies, ω'_r . Using the Néel ground state this intensity included a large component at zero frequency, which was subtracted to obtain realistic moments. The expressions for the first three moments calculated from this theory are :-

$$\begin{aligned} \hbar \langle \omega \rangle &= 42JS(1 - c) = 2A(1 - c) \\ h^2 \langle (\omega - \langle \omega \rangle)^2 \rangle &= 16zJ^2S^2c(1 - c) \\ h^3 \langle (\omega - \langle \omega \rangle)^3 \rangle &= 32zJ^3S^3c(1 - c)(7c - 5) \end{aligned} \qquad (6.10)$$

For pure MnF_2 (c = 0) these equations give a delta function, the result which would be expected from the Ising model. The first moment is plotted (line c) in Fig. 6.2.

6.6 Cluster Model

This is based on the Ising approximation, which gives a simple model of an anti-ferromagnet. The justification for this is that the Ising model predicts an energy for a single spin reversal at a frequency equal to that of a critical point in the spin wave density of states. The magnons observed in the Raman spectra originate from just such a point in the zone.

On this model, the energy of a spin reversal depends on the number of magnetic nearest-neighbours of a Mn ion. If there is a Mn ion at a site $\underline{l}$, then one of its neighbouring sites, say $\underline{l} + \underline{\delta}$ must also be occupied by a Mn ion for a two-magnon excitation to be observable. Let the remaining (z-1) neighbours include r_1 zinc atoms while the (z-1) neighbours of $\underline{l} + \underline{\delta}$ (apart from $\underline{l}$) include r_2 zinc atoms. Then, the two-magnon frequency is given by

$$\begin{aligned} \omega_2 &= 2SJ\left[(z-1-r_1) + (z-1-r_2)\right] + 2SJ + 2(S-1)J \\ &= 2A\left[1-\tfrac{1}{2}\left(\frac{r}{z}\right)\right] - 2J \end{aligned} \qquad (6.11)$$

where $r = r_1+r_2$. The final term 2J in equation (6.11) represents the interaction between adjacent spins discussed by Elliott and Thorpe (1969) and its effect is small. The mean frequency, $\langle\omega\rangle$, was calculated in terms of the zinc concentration from equation (6.11) by assuming that the average value of r_1 and r_2 was $c(z-1)$. Neglecting the interaction 2J this gave a mean frequency.

$$\hbar\langle\omega\rangle = 2A(1-\tfrac{7}{8}c) \qquad (6.12)$$

Including the interaction, it is found that

$$\hbar\langle\omega\rangle = 2A'\left(1 - \frac{35}{39}c\right) \qquad (6.13)$$

where $2A' = 2A - 2J$, in agreement with Mitlehner et al (1971). The difference between these two equations is small, and equation (6.12) is compared with the experimental results in Fig. 6.2 (line b). The main difference between equations (6.12) and (6.10) is that the cluster model predicts a finite frequency at c = 1. This follows from the requirements that pairs of Mn ions must occur as neighbours to contribute to the scattering.

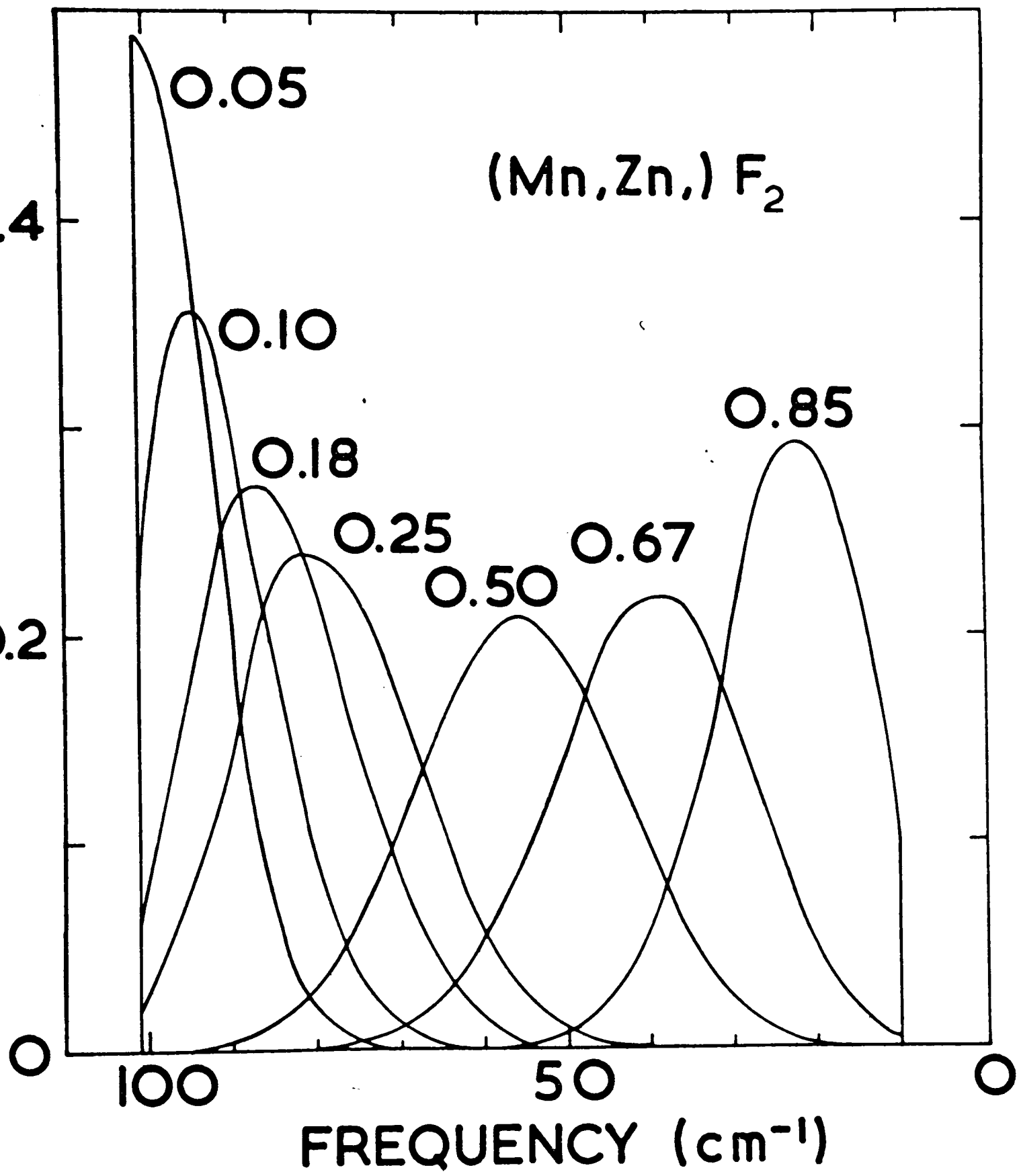
The spectral lineshape was also calculated from the cluster model. The energy of each configuration was found from equation (6.11) and weighted by the probability of that configuration occurring to form a histogram for each value of c. The probability of obtained clusters with r_1 and r_2 neighbouring zinc atoms was given by

$$P(r_1,r_2) = P\begin{pmatrix} r_1 \\ z-1 \end{pmatrix} \times P\begin{pmatrix} r_2 \\ z-2 \end{pmatrix} \qquad (6.14)$$

where $$P\begin{pmatrix} r \\ z \end{pmatrix} = c^r(1-c)^{z-r}\ {}^zC_r$$

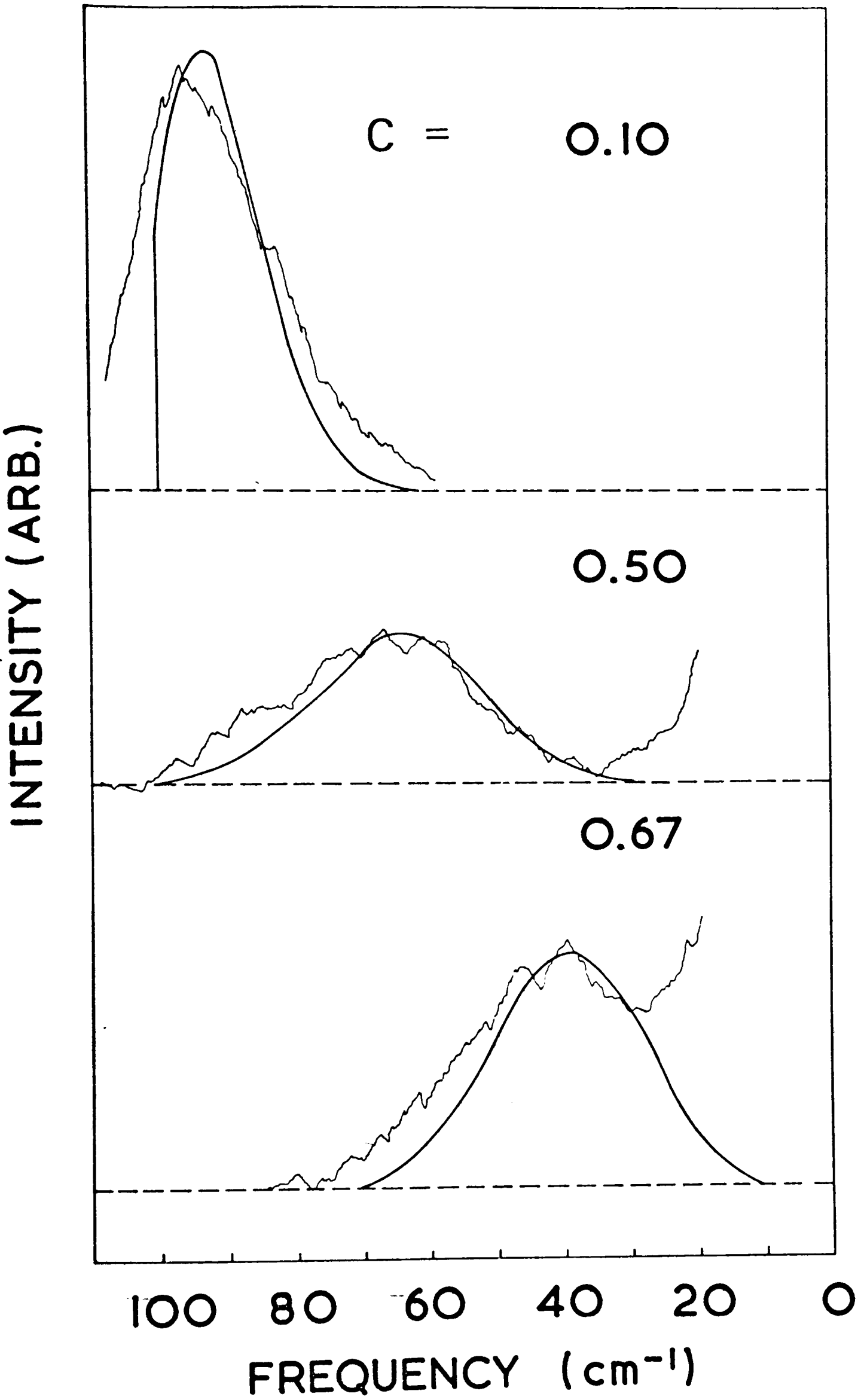
The smoothed histograms are shown in Fig. 6.3, and are compared with the experimental spectra for three values of c in Fig. 6.4. The full widths at half height were measured from the smoothed histograms, and are plotted as a function of c in Fig. 6.5.

Fig. 6.3.



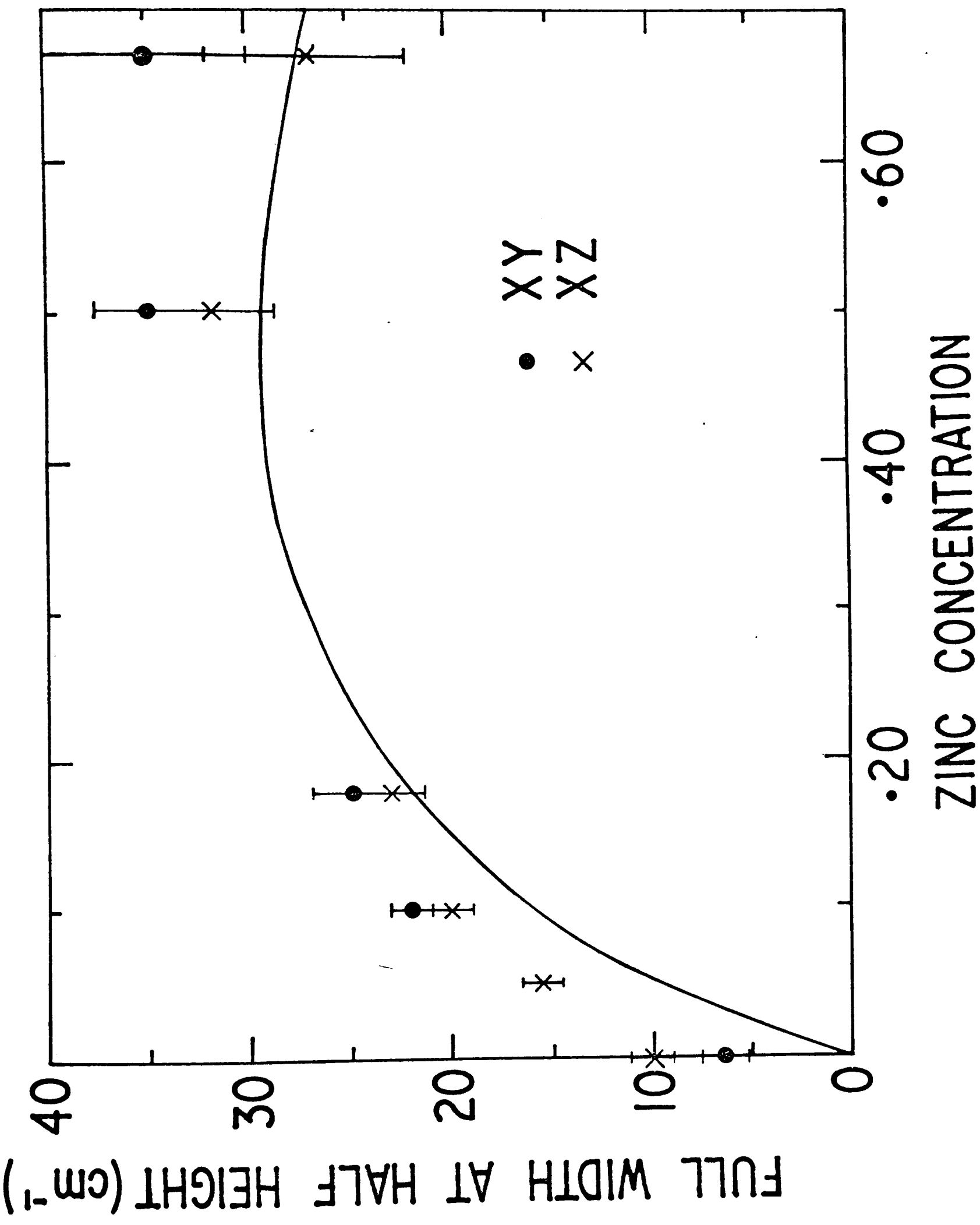
Two-magnon line shapes calculated from Cluster model. Zn concentration c is given for each curve. Vertical scale measures intensity in arbitrary units.

Fig. 6.4.



Comparison of calculated and measured two-magnon bands in xy polarization for three values of c.

Fig. 6.5.



Variation with c of full width at half height of two-magnon Raman band at ∿ 5°K for xy and xz polarizations. Continuous line obtained from Cluster model, (section 6.6).

6.7. Comparison of Experiment and Theory

The most obvious features of the two-magnon Raman spectra are that the peak shifts to lower energy and broadens as the zinc concentration c increases. The experimentally determined shifts are compared with the predictions of the moment theory (line c) and cluster model (line b) in Fig. 6.2. The inset shows the two-magnon frequency determined by infra-red absorption with $\epsilon \| z$ (Buchanan et al 1972). This has a slope $d\omega/dc = -42 \pm 10 cm^{-1}$ per unit Zn concentration, in close agreement with the Raman measurements, (cf. section 6.3).

The measured energy for c = 0 in xy polarization was $100.8 cm^{-1}$, and this was used to evaluate A in the theory. Allowing for the interaction 2J this corresponds to a one-magnon energy of $51.7 cm^{-1}$ which lies between the spin wave energies at the M point ($48.4 cm^{-1}$) and the A point ($53.2 cm^{-1}$) (Nicotin et al 1969), as predicted by equation (6.8a). For xz polarization the c = 0 two-magnon peak was observed at $107.0 cm^{-1}$, close to twice the R point spin wave frequency ($53.7 cm^{-1}$) given by equation (6.8b).

The cluster model gave better agreement with experiment than did the moments method. The experimental points lay consistently higher than either of the theories, especially in the c = 0.2 - 0.5 range. This could be partly accounted for by the mixing of xy and xz polarizations as a result of the random canting of the spins away from the z axis. Such mixing may also be responsible for the structure observed in the xz scattering with c = 0.1 (Fig.6.1). This randomness of spin

direction of each Mn atom caused by the neighbouring Zn atoms was ignored in the theory. Also neglected was the small variation in exchange constant with lattice constant as c varied. The resonance mode at $44cm^{-1}$ observed in neutron scattering (Svensson et al 1969) could not be seen in the Raman spectrum.

The spectral line shapes obtained from the cluster model (Fig. 6.3) are compared with experiment in Fig. 6.4 for c = 0.1, 0.5 and 0.67. This theory gave an asymmetric band at c = 0.1 and a symmetric band at c = 0.5 in reasonable agreement with experiment. The cluster model gave a direct measure of the linewidth which is compared with the experimental results in Fig. 6.5. It gave widths which were about 10% smaller than those observed; the narrowing of the two-magnon band at high c was seen (Fig. 6.5) as predicted.

It was not possible to compare directly the experimental widths with the results of the moments calculations, as the full width at half height is not simply related to the second moment unless the shape (i.e. all the higher moments), is known. Assuming arbitrarily that the lineshape was Gaussian, the moment theory gave the shape of the width/concentration curve as an ellipse which rose with infinite slope at c = 0 and reached a maximum of $44.6cm^{-1}$ at $c = \frac{1}{2}$ (Buchanan et al 1972). This always overestimated the width, but as the lineshape was not Gaussian this discrepancy is not necessarily significant. A later, more complex, theory by Buyers, Pepper and Elliott (1973) using the Coherent Potential Approximation (CPA) gave estimates of the widths which were

slightly better than the cluster model. The CPA theory gave a width of $\sim 40 cm^{-1}$ at c = 0.6, in good agreement with experiment.

In measuring the linewidths no allowance was made for the experimental Raman resolution ($\sim 3 cm^{-1}$) but this was much smaller than the observed widths in all cases. It was not possible to determine experimentally whether the asymmetry of the observed Raman line became zero at c = 0.5, as suggested by the cluster model, or at c = 0.71 given by the moment results (equation (6.10),) due to the low signal -to-noise ratio.

Both theory and experiment agreed in showing that as the critical concentration c_0 was approached no critical behaviour was apparent in the two-magnon Raman cross-section. This was probably due to the fact that the light scattering was sensitive largely to short wavelength modes which depended more on immediate surroundings than on the long range order which disappeared at c_0 and was consistent with the fact that neutron results for zone boundary modes showed little dependance on long range order near c_0 (Coombs et al private communication).

6.8 Phonons in $(Mn,Zn)F_2$.

The rutile structure of MnF_2 and ZnF_2, D_{4h}^{14}, has two molecules per unit cell. This has 15 optic vibrational

modes, which at $\underline{k} = 0$ belong to the following irreducible representations

Raman active	A_{1g}, B_{1g}, B_{2g}, E_g.
Infra-red active	A_{2u}, $3E_u$.
Optically inactive	A_{2g}, $2B_{1u}$.

A discussion of these phonons is given by Gabanov and Shur (1966). The Raman active phonons in several rutile materials, including MnF_2 and ZnF_2 have been measured experimentally by Porto, Fleury and Damen (1967). As all the Mn (or Zn) atoms lie at centres of inversion, these must remain stationary in all the $\underline{k} = 0$ even modes. Therefore the Raman active modes involve only motion of fluorine atoms.

All the Raman active modes in the $(Mn,Zn)F_2$ mixed crystals were measured at 300, 80 and 10°K. At 300°K the results for pure MnF_2 and ZnF_2 agree with those of Porto et al (1967). On cooling the crystals all the lines in the pure crystals (except the B_{1g} mode) moved to slightly higher frequencies. The phonon frequencies for MnF_2 and ZnF_2 are given in Table 6.1. At low temperature the frequencies of the singly degenerate modes in the mixed crystals varied linearly between the corresponding values of MnF_2 and ZnF_2. The behaviour of the A_{1g} phonon is shown in Fig.6.6 where it should be noted that the vertical bars indicate the full width at half height of the line, and not the uncertainty in its

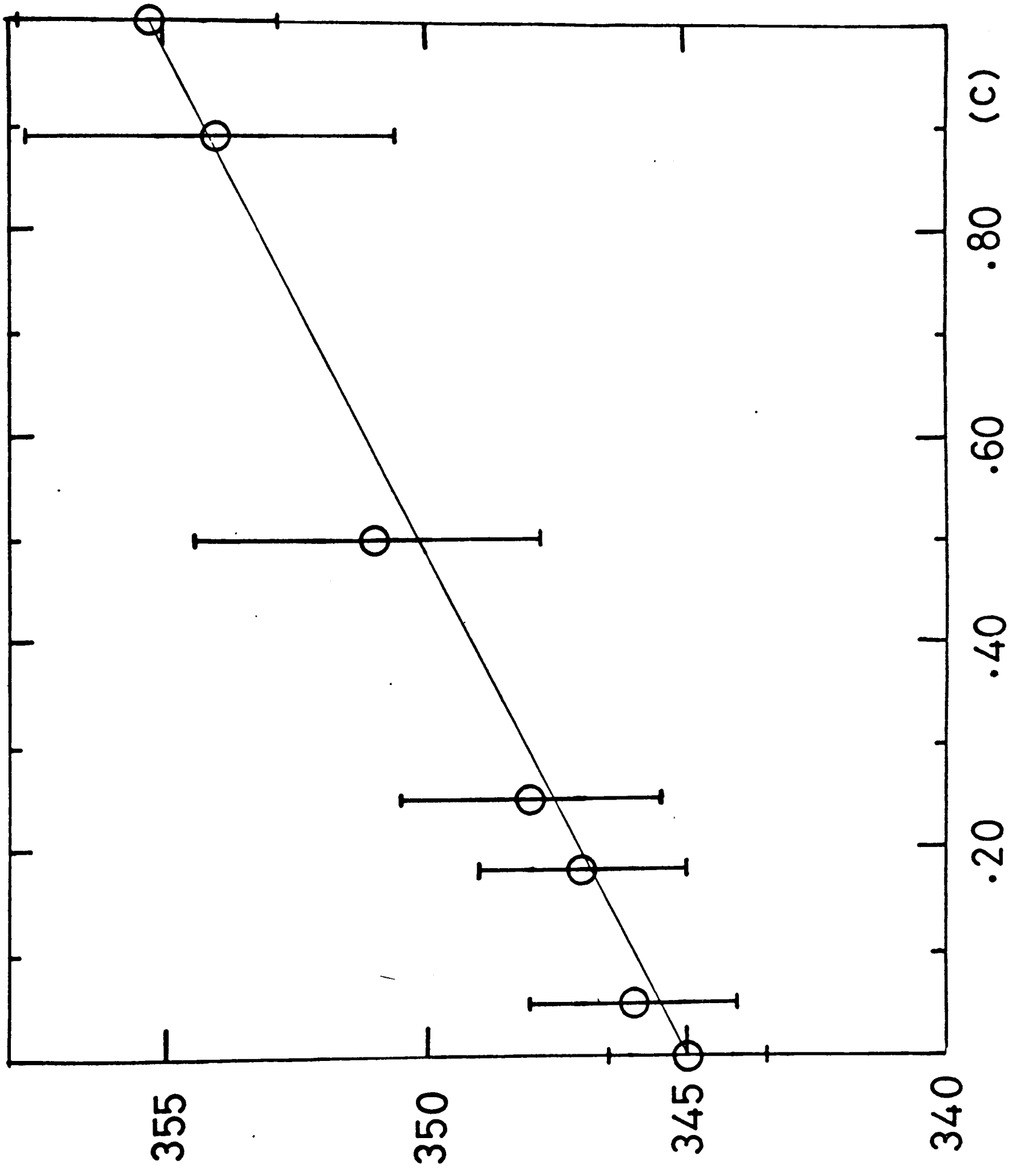
Table 6. 1.

Wave numbers of the Raman active phonon modes in MnF_2 and ZnF_2. Accuracy $\pm$ 2 cm $^{-1}$

Crystal and Temperature		Symmetry B_{1g}	E_g	A_{1g}	B_{2g}
MnF_2	300K	59	246	340	475
	77K	51	248	345	480
	10K	52	248	347	482
ZnF_2	300K	70$^+$	250	349	522$^+$
	77K	64	253	355	529
	10K	65	254	355	532

+ From Porto et al (1967).

Fig. 6.6.



Variation in peak position at 80°K of the A_{1g} Raman vibrational mode with c. Vertical bars indicate full width at half-height of the line.

frequency. This is the normal single-mode type of behaviour which would be expected in mixed crystals whose constituents have corresponding vibrational frequencies close to each other (Chang and Mitra 1971).

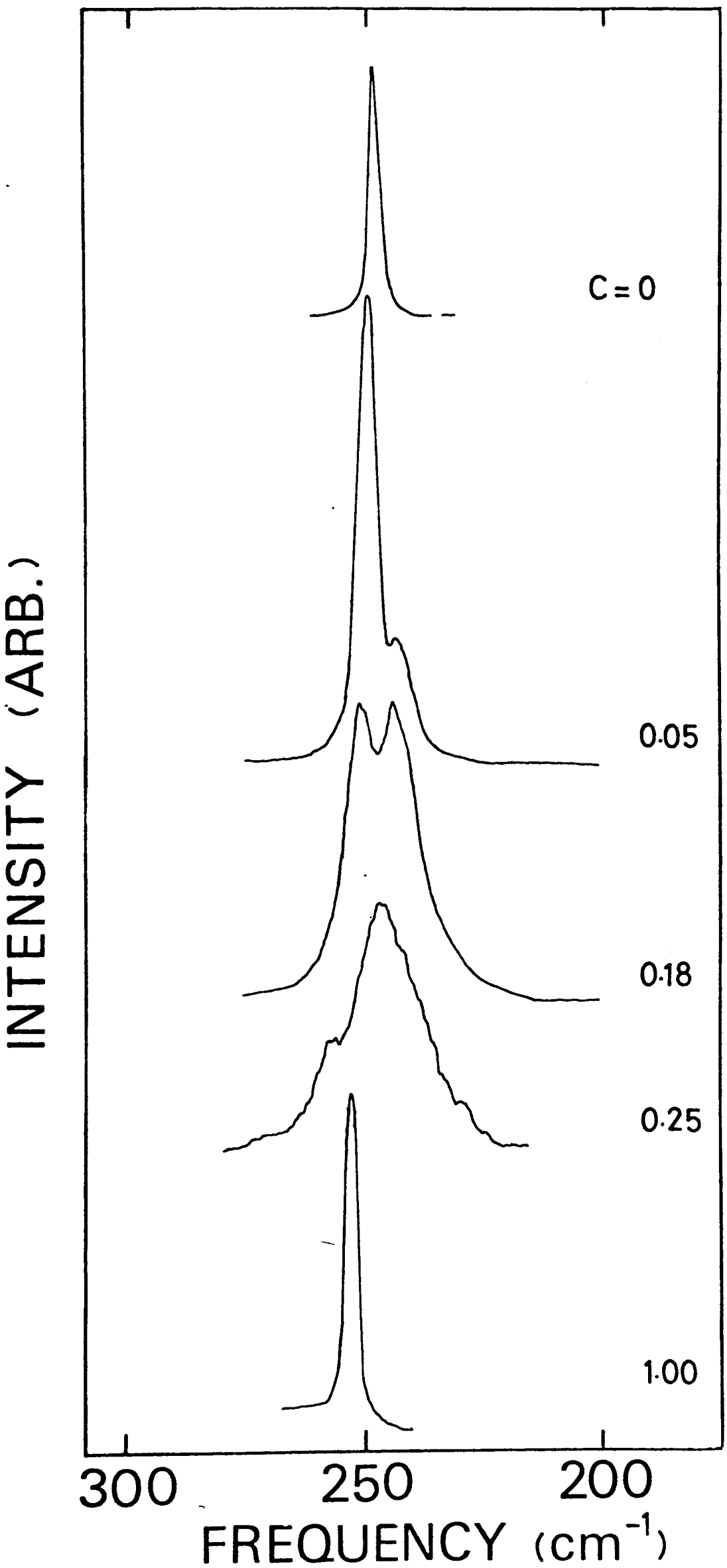
The doubly degenerate E_g mode showed a more complex behaviour in the mixed crystals. In the range $0 < c < 0.25$ two-mode behaviour was observed Fig. 6.8. An intense low frequency component was observed at low c, the intensity of which decreased relative to the higher component with increasing c. At $c = 0.18$ two equally intense phonons were observed. For $c = 0.25$ the lower frequency component is barely detectable, and with $c > 0.25$ only a single broad mode could be seen.

The polarizations of these two modes were carefully investigated to see if they were the split components of a single E_g phonon, or two separate E_g modes. The Raman tensors for an E_g mode in D_{4h} symmetry materials are (Loudon 1964)

$$\alpha(E_g) = \begin{bmatrix} 0 & 0 & 0 \\ 0 & 0 & d \\ 0 & d & 0 \end{bmatrix} \quad , \quad \begin{bmatrix} 0 & 0 & d \\ 0 & 0 & 0 \\ d & 0 & 0 \end{bmatrix}$$

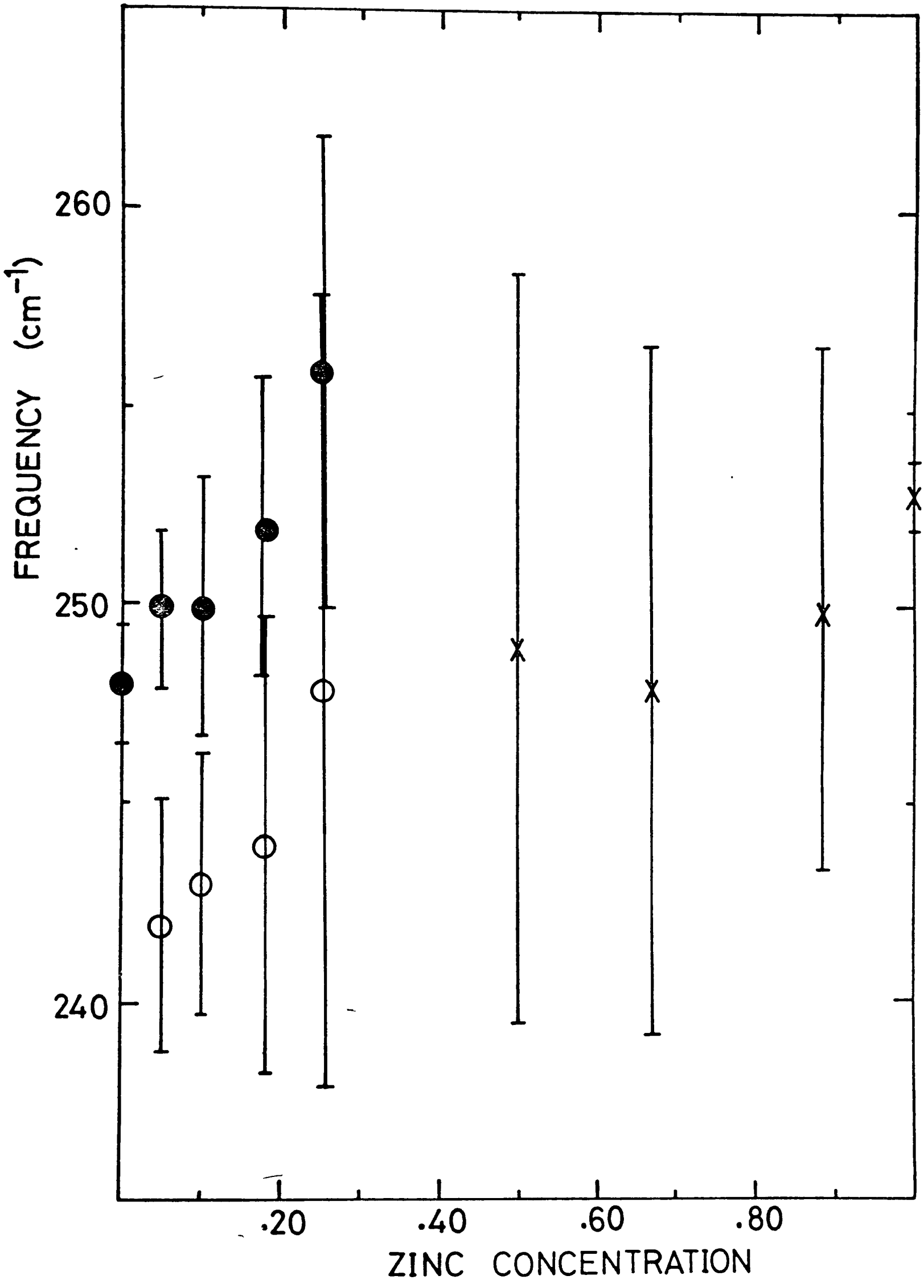
These show that the two components of a split E_g mode appear separately in (zx) and (zy) polarization, while the degenerate mode appears with equal intensity in the two polarizations. Experiments showed that the polarizations were consistent with both phonons being of E_g type, and that the symmetry of the

Fig. 6.7.



Appearance of two E_g phonon modes in $(Mn_{1-c}Zn_c)F_2$ at $80^{o}K$ for $0 < c < 0.25$.

Fig. 6.8.



Variation with c of peak position of E_g phonon modes at 80°K. Two mode behaviour is observed for $c < 0.25$ and single mode behaviour at larger c. Vertical bars indicate full width at half height.

crystal had not been reduced.

It was pointed out by Elliott (see Buchanan et al 1972) that this behaviour was consistent with a local mode which extended over several neighbours. Even though the E_g mode in pure ZnF_2 was at a higher frequency than that in MnF_2, the replacement of Mn by a small amount of Zn could produce a quasi-local E_g mode provided that the force constant at a Zn impurity was less than at a Mn site. A model for the lattice dynamics of CoF_2 (which has the same structure as MnF_2) has been developed by Martel, Cowley and Stevenson (1968), who also used neutron scattering to measure the phonon dispersion curves of CoF_2. These results suggest that the E_g mode is a member of a branch whose frequency falls by only $3cm^{-1}$ in the Σ direction, and rises from Γ in the Λ direction. If MnF_2 has similar dispersion curves, then the Zn mode might lie in a region where the density of states is determined largely by phonons of different symmetry, and would be consistent with observation of a quasi-local mode.

As far as is known the phonon dispersion curves of MnF_2 have not been measured experimentally. Until these are known a more detailed explanation of the observed phenomena will not be possible.

A P P E N D I C E S

Appendix 1. Moments

An experimental method of measuring the moments of a Raman lineshape would greatly facilitate the comparison of experimental and theoretical results. It is sometimes the case, especially with magnon spectra, that the first few moments of a lineshape can be calculated theoretically, whereas the complete shape (i.e. all the moments,) cannot. To compare all the theoretical results, rather than just the peak position of a line, with experiment therefore requires a means of measuring the moments directly. To measure the moments, the lineshape must first be determined, and this in turn requires that the background scattering, (the "wing" of the Rayleigh line), be subtracted. It should be noted that for broad lines which overlap this "wing" (e.g. magnon lines at high temperatures or in dilute alloys), an iodine cell (Devlin et al 1971) has the disadvantage that the iodine absorption lines distort the lineshape. (An iodine cell is most effective for studying sharp lines at low frequencies, when it is unlikely that the line being studied coincides with an iodine absorption line).

The background arises mainly from light scattered from the sample at the laser frequency. It consists partly of true Rayleigh scattering, but the dominant portion arises from light scattered by imperfections in the crystal. The laser linewidth is very much less than the spectrometer resolution so that the width of the background is determined by the spectrometer slit widths. If the shape is determined

by the spectrometer, then the intensity of the background at some frequency shift should be proportional to the intensity of the unshifted central peak, for all crystals. The method attempted for determining the background was based on this assumption. The basis of the technique was as follows:- the magnon spectra were measured, together with the intensity of the central (zero-frequency shift) peak with the beam attenuated by a suitable filter. The background was then measured by scattering light from a material which had no low frequency excitations, and then measuring the central peak with the same filter. The background was scaled by the ratio of the central peak intensities and subtracted. The problem was reduced to finding (1) a suitable material which produced the correct lineshape for the background, and (2) a filter which was reproducible to obtain the scaling factor. This appendix describes briefly some attempts to find materials that would satisfy these requirements.

It was necessary to find a suitable filter before any materials for background scattering could be tested. The first filter used was simply a piece of thin white paper placed over the entrance slits of the spectrometer. Although this attenuated the beam satisfactorily the scattered intensity was found to be unreproducible. This was tested by repeatedly scanning through the Rayleigh line of light scattered from a crystal. It was also found that the translucent paper broadened the image at the entrance slits, changing the effective resolution of the spectrometer and hence the shape of the

background.

To overcome the latter problem, we tried placing a filter in the incident laser beam. With a much higher intensity to be attenuated, darkened photographic plate, polaroid and glass filters all suffered heat damage. A liquid filter was constructed, consisting of coloured dye in aqueous solution sealed into a brass container with thin quartz windows at the top and bottom. The path length was about 2cm, and it was hoped that this would distribute the absorbed heat. An interesting effect was observed with this filter. The heating effect along the optical path appeared to change the lquid's refractive index, which made the beam diverge, thus changing the effective focal length of the focusing lens. The effect was demonstrated by moving this lens down to refocus the laser beam in the crystal. The distance moved was of course dependant on the laser power, but was typically 1.5cm, making the filter unusable. There was also a problem of bubbles forming in the liquid a few weeks after the filter had been constructed, even though the liquid had been boiled to remove dissolved gases.

Finally we decided that the filter must be placed in the light path after the spectrometer. The photomultiplier tube housing was modified to incorporate a neutral density filter, which could be slid in and out of the light path, immediately in front of the photocathode. This arrangement ensured that the light always passed through the same part of the filter, which was a glass photographic plate, exposed to

the light and then developed. The attenuation factor could not be measured precisely, but was $\gtrsim 10^5$, and reduced the intensity to a convenient value. It was found that this arrangement was reproducible within 3%

Having found a reliable filter, suitable background-scattering materials were searched for. The requirements for such a material are:- (a) it should have a similar shape of central peak to the material under study; (b) there should be no low-frequency excitations to distort the background; (c) the intensity of the central peak should be comparable to that of the material under study in order to minimize scaling errors.

In the first experiment, light was scattered from a polished metal surface. This drastically overestimated the background, probably due to the image broadening effect mentioned above. Next, a suspension of carbon particles in water was tried. This was also unsuccessful, partly because liquids have broad central modes which distort the shape and partly because of intensity fluctuations. The scattered intensity at any instant depended on the number of particles illuminated, producing a flickering effect.

All other experiments were done using transparent crystals, as similar as possible to the material being studied. As the primary interest was in studying two-magnon lines, we tried to obtain the background using non-magnetic crystals of the same structure. For the magnons in MnF_2 we tried ZnF_2, and for $RbMnF_3$, we used $KMgF_3$. Unfortunately, neither was

successful. The ZnF_2 fluoresced slightly which distorted the shape of the background, and the central peak in $KMgF_3$ was very much less than in $RbMnF_3$, giving large errors in the scaling of the background.

In another experiment we tried to measure the moments of the two-magnon line in $RbMnF_3$ as a function of temperature. This material was chosen as the magnon line is about two orders of magnitude more intense than in MnF_2, giving a better signal-to-noise ratio. At 4.2^oK, the two-magnon line was at $\sim 115cm^{-1}$, with a width of $\sim 10cm^{-1}$. On heating, the magnon line broadened and shifted towards zero frequency. The lineshape of the "wing" of the laser line in $RbMnF_3$, at 4.2^oK, when the magnetic scattering all occurred at a much higher frequency, was subtracted from the spectra obtained at higher temperatures. By using the same material to obtain the background, we hoped to minimize errors due to differing lineshapes. The method was unsuccessful, as below about $15cm^{-1}$ the lineshapes were obviously in error, and this had a large effect on the moments.

There are still several outstanding problems with this technique. First, we have not been able to find a demonstratably reliable method of obtaining the lineshape of the backgrcund scattering. Secondly, when measuring spectra as a function of temperature, unavoidable movements of the crystal occur due to thermal expansion in components of the cryostat. If the laser beam then strikes a small flaw in the crystal resulting in a bright spot, this changes both the <u>shape</u>

of the background (probably due to image broadening), and also the peak intensity (which alters the scaling factor). Large errors are also involved in extracting the low intensity magnetic scattering from the relatively large background.

In order to measure the moments of a line about $40cm^{-1}$ wide centred at $\sim 20cm^{-1}$, it is necessary to obtain the lineshape accurately down to $\sim 5cm^{-1}$ from the laser. Because of the frequency weighting factor in the moments, errors in the measurement below $5cm^{-1}$ have little effect, (unless the lineshape has a large intensity at zero frequency). It should be possible to achieve this using very narrow slits and good optical quality crystals. The moments of the two-magnon lines in MnF_2 and $RbMnF_3$ have very recently been measured as a function of temperature by Brya and Richards (P.L.Richards, private communication). They used very good optical quality crystals which had little background scattering. The small amount of background scattering was subtracted "by eye" to obtain the lineshape.

Appendix 2.

Electronic Raman scattering in HoF_3 and TbF_3

HoF_3 and TbF_3 both have the orthorhombic YF_3 structure, D_{2h}^{16}, with four molecules in the unit cell (Wyckoff 1964). The Rare Earth site has C_S symmetry, so that the (2J + 1) - fold degeneracy of the free-ion levels should be totally removed. These materials were chosen for study because the selection rules in such a low symmetry permitted transitions between all the electronic levels of the ground state multiplet to be Raman active.

The crystals were supplied by Dr. W.J.L.Buyers and were of good optical quality. They were oriented by X-ray analysis, and cut into cubes with (100) faces of side approximately 3mm. The Raman spectra were obtained with the crystals mounted in the variable temperature cryostat (Chapter 3), using about 200mW of 514.5n.m. radiation from the Argon-ion laser. Spectra were obtained in all polarizations at 4.2, 20, 77 and $\sim 300^{\circ}K$.

At room temperature the spectra in corresponding polarizations of HoF_3 and TbF_3 contained a similar set of lines, with frequencies differing between the two materials by a few wavenumbers. These were identified as phonons. On cooling the crystals below $77^{\circ}K$, new lines appeared in the spectra which were characteristic of either Ho^{3+} or Tb^{3+}. These lines increased in intensity and decreased in width rapidly as the temperature was lowered, and had asymmetric Raman tensors; they were therefore assumed to be due to electronic excitations

between the levels of the ground state multiplet of either Ho^{3+} or Tb^{3+}. These are discussed for the two materials separately in sections (a) and (b) below.

The four molecules in the unit cell of HoF_3 and TbF_3 give 48 zone-centre phonons. These are listed by Rast, Caspers and Miller (1968) as :-

$$7\left[A_g + B_{2g} + B_{3u} + B_{1u}\right] + 5\left[A_u + B_{2u} + B_{3g} + B_{1g}\right]$$

All the 24 even-symmetry phonons are Raman active. Of these, 22 were observed, and it was found that their frequencies increased by $\sim 3cm^{-1}$ on cooling from 300 to 4.2°K. The phonon frequencies for HoF_3 at 20°K are given in Table A2.1, and for TbF_3 in Table A2.2.

The YF_3 structure has a mirror-plane through the Rare Earth sites perpendicular to the b axis (Wyckoff 1960); the Rare Earth sites are all equivalent. Our axes x, y, z were chosen to be parallel to the axes a, b, c respectively of Wyckoff. The electronic levels of the Rare Earth ion can be classified in terms of the irreducible representations of their site symmetry, C_S. Decomposition of the even-symmetry irreducible representations of D_{2h} into those of C_S gives the following:-

$$A_g,\ B_{2g} \longrightarrow A'$$

$$B_{1g},\ B_{3g} \longrightarrow A''$$

Table A2. 1.

Phonon frequencies (cm^{-1}) of HoF_3 at $20^{o}K$.

Symmetry	A_{1g}	B_{1g}	B_{2g}	B_{3g}
Frequency (cm^{-1})	92	135	95	175
	113	190	198	261
	174	284	210	270
	249	347	352	348
	345	399	369	
	376		520	
	448			

Table A2. 2.

Phonon frequencies (cm^{-1}) of TbF_3 at $20^{o}K$.

Symmetry	A_{1g}	B_{1g}	B_{2g}	B_{3g}
Frequency (cm^{-1})	90	130	93	170
	111	188	199	253
	166	278	213	260
	247	339	343	334
	344	391	359	
	366		509	
	437			

Thus electronic Raman transitions of A' symmetry appear in polarizations (xx, yy, zz, xz, zx) while those of A'' symmetry are seen in (xy, yx, yz, and zy). Transitions between levels of the same symmetry have A' symmetry, while those between levels of different symmetry have A'' symmetry.

(a) $\underline{HoF_3}$

Ho^{3+} has a ground state multiplet $^5I_8$, which should be split by the crystal field into $(2J + 1) = 17$ non-degenerate levels. At 77°K eleven electronic transitions were seen, (Table A2.3). These could be fitted to the energy level scheme shown in Fig. A2.1. The energies in cm^{-1} of each level are given on the left hand side of the diagram. Several transitions were identified as originating from excited states by observing their decrease in intensity as the levels were thermally depopulated on cooling. The energy and symmetry of each of the transitions are shown in Fig. A2.1.

The relative symmetries of all the electronic levels was deduced from the polarizations of the transitions; the symmetries are shown on the right hand side of Fig. A2.1, where it was arbitrarily assumed that the ground state has A' symmetry. If the ground state has A'' symmetry, then the symmetries of all the other levels are interchanged.

(b) $\underline{TbF_3}$

Tb^{3+} has a ground state multiplet $^7F_6$, which in TbF_3

Table A2. 3.

Electronic Raman transitions in HoF_3 at $77^{o}K$, frequencies (cm^{-1}) and polarizations.

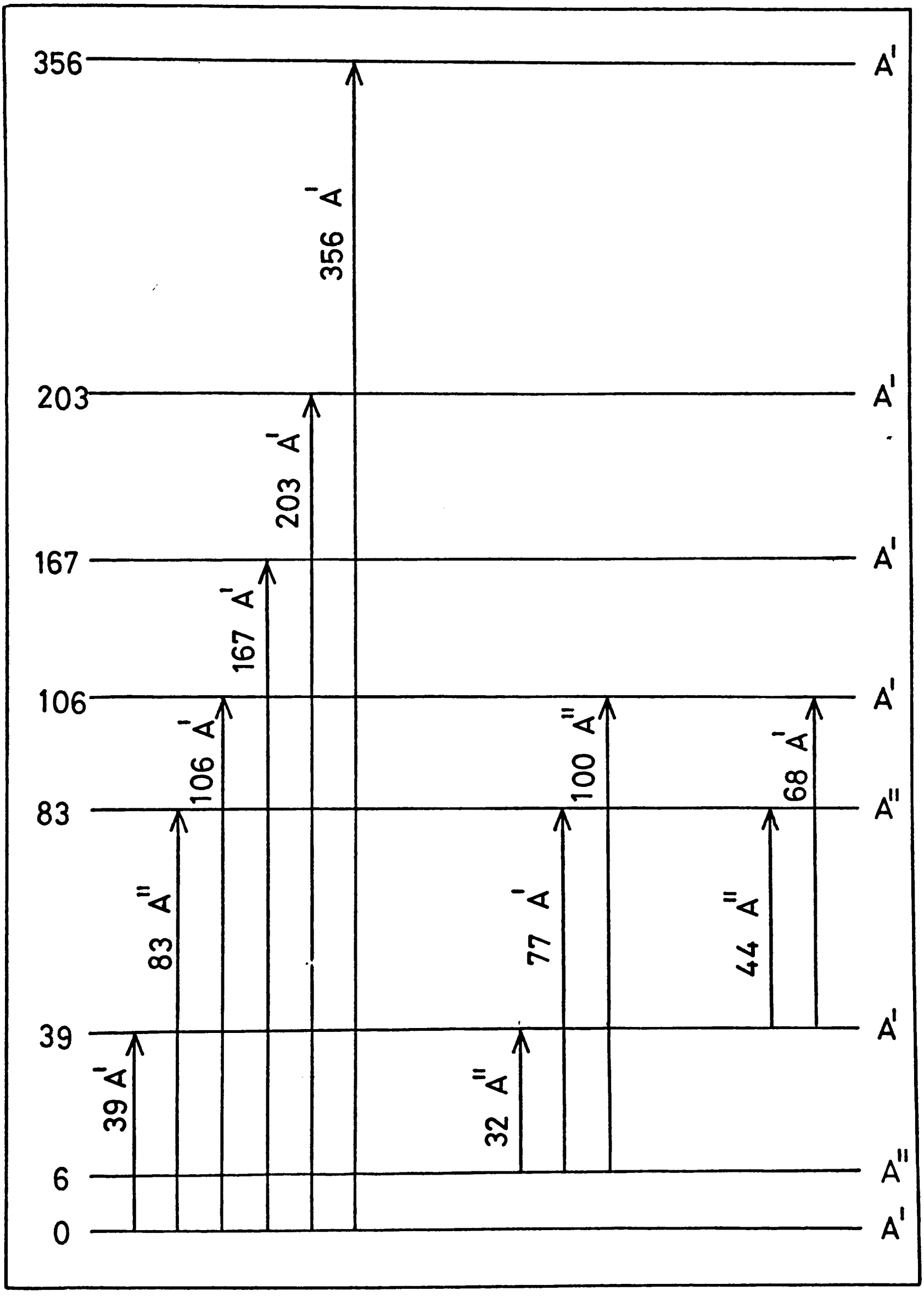
Polarization								
xx	yy	zz	xy	yx	xz	zx	yz	zy
39w	167	39	32^{+}	-	39	-	32^{+}	32^{+}_{w}
68^{+}		-	82	-	68^{+}	-	44^{+}	44^{+}
77^{+}_{w}		77+			77+	-	83	83
		106					100+	100+

\+ denotes transition out of excited state

w denotes weak line

Fig. A2.1.

Partial level scheme for $^5I_8$ ground multiplet in HoF_3. Raman transitions observed at 77°K are shown with their symmetries and energies (in cm^{-1}).



should be split into 13 non-degenerate levels. TbF_3 has been observed to order ferromagnetically below T_c = (3.95 ± 0.05)°K, (Holmes et al 1970). From this Holmes concluded that the ground state of the Tb^{3+} ion was an "accidental" doublet. Holmes et al found that their magnetisation data was consistent with a canted, two-sublattice model in which the magnetic moment of each sublattice was in the xz plane, at about 25° on either side of the x axis. If a magnetic field of greater than about 13 KOe. was applied along the z axis, a spin-flip transition was seen in which the magnetisation direction of one sublattice reversed, changing the direction of net magnetisation from the x to the z axis. In the ferromagnetic phase, the Tb^{3+} ions occupy two magnetically inequivalent sites of point symmetry C_{1h}, with principal magnetic axes related by a mirror reflection in the xz plane (Holmes and Guggenheim 1971).

At 5°K we observed seven electronic Raman transitions out of the ground state. Their frequencies, polarizations and symmetries are given in Table A2.4a. On cooling to 2°K, (below T_c), the electronic spectra changed, giving the lines listed in Table A2.4b. The spectra in yx and zx polarizations at 2°K appeared to be identical. No transition between the components of the ground state, which should have been split in the ferromagnetic phase could be detected. (This splitting has very recently been measured as 7.2 ± 0.4cm^{-1} at 2.1°K by optical fluorescence (J. Brinkmann, private communication). Since Rayleigh scattering limited our Raman observations to

Table A2. 4.

Electronic Raman transition in TbF_3

(a) $5^{o}K.$

Frequency (cm^{-1})	Polarization	Symmetry
114	yx	A''
120	yz and zx	A' and A''
124	zx	A'
131	yz	A''
183 } 193 } 317 }	xz and zx	A'

(b) $2^{o}K.$

Frequency (cm^{-1})	Polarization	Symmetry
113	yz	
116 } 120 }	yx and zx	A' and A''
131	yz	A''

$> 10cm^{-1}$ we would have been unable to detect a splitting of $7.2cm^{-1}$).

In other experiments a magnetic field was applied, using the superconducting magnet (Chapter 3). At $5^{o}K$, with the field along the y axis, no change ($< 1cm^{-1}$) was observed in the position of the 120, $131cm^{-1}$ lines in yz polarization in fields up to 25KG.

The magnetic field was applied along the x axis at $2^{o}K$. In yz polarization the lines at 113, 120, $131cm^{-1}$ did not change in fields of up to 37KG. The line at $\sim 116cm^{-1}$ in yx polarization increased slightly in frequency, from $115.5cm^{-1}$ in zero field to $118.3cm^{-1}$ in 37KG.

Finally, the field was directed along the z axis at $2^{o}K$. As the field was increased sudden changes occurred in the line positions at a field < 20KG. No further changes were seen as the field increased to 37KG. This was consistent with the occurrence of the spin-flip transition reported by Holmes et al (1970). We have not yet studied the effect of a magnetic field on the higher frequency electronic lines.

So far, we have been unable to devise an electronic energy level scheme which is consistent with the observed transitions. The observed transition frequencies do not fit the level scheme for the $^{7}F_{6}$ multiplet of Tb^{3+} in TbF_{3} obtained by Krupka and Gu genheim (1969) from fluorescence. Unfortunately, we cannot explain the effect of a magnetic field on the transition frequencies.

While the electronic spectra of HoF_{3} could be readily

interpreted, those of TbF_3 still remain unexplained. The situation will perhaps become clearer in the future if neutron scattering data become available.

REFERENCES

Allen,S.J., Loudon,R., Richards,P.L., (1966) Phys.Rev.Lett 16, 463.

Baker,J.M.,Lourens,J.A.J.,Stevenson,R.W.H. (1961) Proc.Phys. Soc. 77, 1038.

Bass,F.G., & Kaganov,M.I. (1959) Zh. Eksperim. i. Teor. Fiz. 37, 1390.
(English translation (1960) Soviet Phys - J.E.T.P. 10, 986.)

Becker,P.J., Laugsh,J (1971) Phys. Stat. Solid (6) 44, K109.

Becker,P.J., Leask,M.J.M., Tyte,R.N. (1972) J.Phys.C. 5, 2027.

Bhagavantam,S., Venkatarayudu,T. (1939) Proc. Indian Acad, Sci. A 9, 224.

Birman,J.L., (1962) Phys. Rev. 127, 1093.

Boal,D., Grunberg,P., Koningstein,J.A. (1973) Phys.Rev. B. 7, 4757.

Born,M., Bradburn,M. (1947) Proc. Roy. Soc. A. 188, 161.

Born,M., Huang,K. (1954) Dynamical Theory of Crystal Lattices Oxford, Clarendon Press).

Brya,N.J., Richards,P.M., Barckowski, R.R. (1972) Phys. Rev. Lett. 826.

Buchanan,M., Buyers,W.J.L., Elliott,R.J., Harley,R.T., Hayes, W., Perry,A.M., Saville,I.D. J. Phys. C. 5, 2011. (1972).

Burbank,R.D., (1970) J.Appl. Cryst. 3, 112.

Buyers, W.J.L., Pepper, M.D.E., Elliott,R.J., (1973) J.Phys.C. 6, 1933.

Cashion,J.D., Cooke,A.H., Hoel,L.A., Martin,D.M., Wells,M.R.(1970) Colloques du C.N.R.S. No. 180 II, 417.

Chang,I.F., Mitra,S.S. (1971) Adv. Phys. 20, 359.

Chaves, A., Porto,S.P.S., (1972) Sol. State Comm. 10, 1075.

Cochran, W. (1963) Rep. Prog. Phys. 26, 1.
Cochran, W., Zia,A. (1968) Phys.Stat. Solidi. 25, 273

Cohen,E., Riseberg,L.A., Nordland,W.A., Burbank,R.D., Sherwood,R.C., van Uitert,L.G.,(1969) Phys. Rev. 186, 476.

Cooke, A.H., Martin,D.M., Wells,M.R., (1971) J. de Physique, Paris. 32, C1, 488.

Cowley, R.A., (1963) Adv. Phys. 12, 421.

Cowley R.A., Buyers,W.J.L. (1972) Rev. Mod. Phys. 44, 406.

Dawber,P.G., Elliott,R.J., (1963) Proc. Roy. Soc. 273, 222.

Devlin,G.E., Davis,J.L., Chase,L., Geschwind,S. (1971). Appl. Phys. Lett. 19, 138.

Elliott,R.J., Heap,B.R., (1962) Proc. Roy. Soc. A265, 264.

Elliott, R.J., Loudon,R. (1963) Phys. Lett. 3, 189.

Elliott, R.J., Hayes,W., Jones,G.D., MacDonald,H.F.,Sennett,C.T. (1966) Proc. Roy. Soc. A 289, 1.

Elliott, R.J., Thorpe,M. (1969) J.Phys. C. 2, 1630.

Elliott, R.J., Harley, R.T., Hayes,W., Smith,S.R.P. (1972). Proc. Roy. Soc. Lond. A 328, 217.

Finkman,E., Cohen,E., van Uitert,L.G., (1971) Proc.Int.Conf. on Light Scattering in Solids, Paris, 1971 (Ed. M.Balkanski). p. 369 Paris, Flammarion.

Fleury,P.A., (1971) Light Scattering in Solids (Flammarion Sciences: Ed. M. Balkanski) 151.

Fleury,P.A., Loudon,R. (1968) Phys. Rev. 166, 514.

Gabanov,A.I., Shur,M.S., (1966) Sov.Phys. Sol.St. 7, 2124.

Gehring,K.A., Malozemoff,A.P., Staude,W.S., Tyte,R.N. (1971) Sol.St. Comm. 9, 511.

Greene,R.L., Sell,D.D., Feigelson,R.S., Imbusch,G.F., Guggenheim,H.J. (1968) Phys. Rev. 171, 600.

Gross, E., Permogorov,S., Travnikov,V., Selkin,A. (1971) Light Scattering in Solids (Paris) p. 238.

Harley,R.T., Page,J.B., Walker,C.T., (1971) Phys.Rev.B. 3, 1365.

Harley,R.T., Hayes,W., Perry,A.M., Smith,S.R.P.(1973a). J. Phys. C. 6, 2382.

Harley, R.T., Hayes,W., Perry,A.M., Smith,S.R.P. (1973b). (Submitted to Sol. St. Comm). Clarendon preprint no. 49/73

Harrison,W.A. (1970) Solid State Theory (McGraw Hill)

Heine,V. (1960) Group Theory in Quantum Mechanics (Pergamon).

Holmes,L., Guggenheim,H.J., Hull,G.W. (1970) Sol. St. Comm. 8, 2005.

Holmes,L., Guggenheim,H.J. (1971) Journal de Physique C1, 501.

Hougen,J.T., Singh,S. (1963) Phys. Rev. Lett. 10, 406.

Jona,F., Shirane,G. (1962) "Ferroelectric Crystals" (Pergamon Press).

Kiel,A. (1969) Light Scattering Spectra of Solids (ed.G.B.Wright) (Springer - Verlag, New York) p. 245.

Kiel, A., Porto,S.P.S. (1969) J.Mol.Spectroscopy 32, 458.

Kiro,D., Low,W., Zusman,A. (1963) "Paramagnetic Resonance" (ed.W.Low) Vol. I, p.44. New York: Academic Press.

Kittel,C. (1966) Quantum Theory of Solids (Wiley)

Kramers,H.R. (1930) Proc. Acad. Sci. Amsterdam. 33, 959.

Krupka,D.C., Gu genheim,H.J. (1969) J.Chem.Phys. 51, 4006.

Lea, K.R., Leask,M.J.M., Wolf,W.P. (1962) J.Phys. Chem Solids. 23, 1381.

Loudon,R. (1964) Adv. Phys. 13, 423.

Loudon,R., Johnson,F.A. (1964) Proc. Roy. Soc. A.281 274.

Maradudin,A.A., Fein,A.E., Vineyard,G.H. (1962). Phys. Stat. Sol 2, 1479.

Martel, P., Cowley,R.A., Stevenson,R.W.H., (1968) Can.J.Phys. 46, 1355.

Martin-Brunetière,F. (1969) J. de Physique 30, 839.

Misetch,A., Dietz,R.E., Guggenheim,H.J. (1968) Localized Excitations in Solids (Plenum Press: ed. R.F.Wallis) 379.

Mitlehner,H., Geick,R., Lehmann,W., Weber,R., Dietrich, G., Schoenherr,H. (1971) Sol. St. Comm. 9, 2059.

Moch,P., Gosso,J.P., Dugautier,C. (1971). Light Scattering in Solids. (Flammarion Sci. Ed. M. Balkanski) p.138.

Natoli, C.R., Ranninger,J. (1973) J.Phys.C. 6, 345.

Nicotin,O., Linogard,P.A., Dietrich,C.W. (1969) J. Phys. C. 2, 1168.

Ohlmann, R.C., Tinkham, M. (1961) Phys.Rev. 123, 425.

Okazaki,A., Turberfeld,K.C., Stevenson,R.W. (1964) Phys.Lett. 8, 9.

Porto,S.P.S., Tell,B., Damen,T.C. (1966) Phys. Rev. Lett. 16, 450.

Porto,S.P.S., Fleury,P.A., Damen,T.C. (1967) Phys.Rev. 154, 522.

Pytte, E., Stevens,K.W.H. (1971) Phys.Rev.Lett 27, 862.

Raman, C.V. (1928) Indian J. Phys. 2, 387.

Riseberg, L.A., Cohen,E., Nordland,W.A., van Uitert,L.G. (1969). Phys. Lett. 30A, 4.

Sandercock,J.R., Palmer,S.B., Elliott,R.J., Hayes,W., Smith,S.R.P. Young,A.P. (1972) J.Phys. C. 5, 3126.

Scott, J.F. (1969) Phys. Rev. 183, 823.

Scott, J.F., Cheesman,L.E., Porto, S.I.S., (1967) Phys.Rev. 162, 834.

Steigmeier,E.F., Auderset,H., Harbecke,G. (1973) Sol.St.Comm. 12, 1077.

Svensson,E.C., Holden,T.M., Buyers,W.J.L., Cowley, .A., Stevenson,R.W.H. (1969) Sol. St. Comm. 7, 1693.

Sykes, M.F., Essam,J.W., (1964) Phys. Rev. 133, A310.

Tanabe, Y., Moriya,T., Sugano,S. (1965) Phys.Rev.Lett 15, 1023.

Thomas, H., Müller,K.A (1968) Phys. Rev. Lett. 21, 1256.

Tinkham, M. (1964) Group Theory and Quantum Mechanics. (McGraw Hill).

Van Hove, L., (1953) Phys.Rev. 89, 1189.

Wells, M.R., Worswick R.D. (1972) Phys. Letters. 42A, 269.

Woods-Halley, J. (1969) "Light Scattering Spectra of Solids" (Ed. G.B.Wright,) (Springer - Verlag, New York) p. 207.

Worlock,J.M., Scott,J.F., Fleury,P.A. (1969) Proc. Int. Conf. on Light Scattering in Solids, New York, 1969 (ed.G.B.Wright) p.689, New York,Springer.

Wyckoff,R.W.G. (1960) Crystal Structures (Interscience Publishers Inc., New York) Vol.1, p. 251.

Wyckoff, R.W.G. (1964) "Crystal Structures" 2nd. Ed. Vol.2.
(Wiley - Interscience Inc., New York).

Ziman, J.M., (1969) Principles of the Theory of Solids (C.U.P.)